REFINEMENT OF SYNAPSE POSITION IN AUDITORY BRAINSTEM

REDISTRIBUTION OF SYNAPTIC INPUTS IN THE NEONATAL RODENT AUDITORY BRAINSTEM OCCURS IN THE ABSENCE OF ACOUSTICALLY DRIVEN ACTIVITY

By ZIQI (HUGO) WANG, B. ENG.

A Thesis
to the School of Graduate Studies
in Partial Fulfilment of the Requirements
for the Degree of Doctor of Philosophy

McMaster University

Doctor of Philosophy (2022) McMaster University
(School of Biomedical Engineering) Hamilton, Ontario, Canada

TITLE: Redistribution of Synaptic Inputs in the Neonatal Rodent Auditory Brainstem Occurs in the Absence of Acoustically Driven Activity.

AUTHOR: Ziqi (Hugo) Wang, B. Eng. (McMaster University)

SUPERVISOR: Dr. Deda Gillespie

NUMBER OF PAGES: xv. 134

Lay Abstract

How immature neurons coordinately refine their excitatory and inhibitory inputs is a fundamental question in developmental neuroscience. Lateral superior olive (LSO) is a model system for this question. Principal neurons in mature LSO receive excitatory and inhibitory inputs that are precisely matched for stimulus frequency. This sharp frequency alignment of the two phenotypically different inputs is achieved during postnatal refinement, including synapse elimination and strengthening and changes in neuronal morphology. Synapse redistribution may also contribute to the refinement. Here, I investigated the developmental distribution of excitatory and inhibitory synapses in prehearing rats. Before hearing onset, the distribution of excitatory and inhibitory synapses shifted in complementary directions in the absence of acoustic activity.

Abstract

Principal neurons in the lateral superior olive (LSO) receive excitatory input from the anteroventral cochlear nucleus (AVCN) and inhibitory inputs from the medial nucleus of the trapezoid body (MNTB). These two phenotypically different inputs arriving at individual neurons in mature LSO are precisely matched for stimulus frequency. However, in the immature LSO, excitatory and inhibitory inputs arriving at individual neurons are crudely matched for stimulus frequency. During postnatal development, both excitatory and inhibitory pathways undergo substantially physiological measurable refinement before hearing onset, presumably under the guidance of spontaneous activity generated in the immature cochlea. In the neighbouring nucleus, MSO, inhibitory synapses are redistributed toward the soma, arguably through an experience-dependent manner. Here, in LSO, I investigate how excitatory and inhibitory synapses are redistributed before hearing onset.

In order to do so, I implemented hardware to label single cells in acute living slices, Matlab scripts to segment synapses in 3D, and Matlab scripts for spike sorting and firing state reconstruction (not reported here). Using the tools that I developed, I investigated the developmental distribution of excitatory and inhibitory synapses in prehearing LSO.

At birth, excitatory synapses surprisingly outnumbered inhibitory synapses at the soma and the proximal dendrite. In the ensuing week, before hearing onset, while excitatory synapses are redistributed away from the soma, inhibitory synapses are redistributed toward the soma, such that by hearing onset inhibitory synapses outnumber excitatory synapses at the soma and the proximal dendrite.

Acknowledgements

First and foremost, I would like to thank my supervisor, Dr. Deda Gillespie. I still remember vividly when Deda interviewed me through skype when I was on my graduation trip to Europe. Her enthusiasm for science attracted me to her lab, and she opened the door to neurobiology for me. I was a naïve engineering student. Deda guided me through all the hard times, especially during the pandemic, during which I encountered a series of challenging family issues. Thank you, Deda. Without your guidance, I might diminish in the scientific field, as those synapses that got eliminated during development.

I would also like to thank Dr. Ian Bruce and Dr. Shahram Shirani for taking the time to serve on my supervisory committee. I met Ian when I was in my undergraduate study. He was the one who introduced the Hodgkin and Huxley model to me and offered me an opportunity to work on a research project which opened the field of auditory systems for me. Shahram is an expert in image processing and computer vision. My very first segmentation algorithm took me a week to process a neuron. I had several chats with Shahram, and his advice inspired me to improve my algorithm and cut the processing time to half an hour.

A lot of people helped me during my time in graduate school. I want to thank all the members of the Gillespie lab. I appreciate James Jonkman from advanced optical microscopy facility (AOMF) in Toronto. James generously allowed me to use his facility to analyze my image data. I also want to thank all my friends in Canada and China. I really appreciate my parents for their financial support. I want to shout a special thank you to Tiankai Zhang and Marvella Wang.

Last but not least, I appreciate all the front-line workers and every individual that followed the mask policy during the pandemic.

Contents

List of figures and tables

Abbreviations

AMPA(R)	2-amino-3-(3-hydroxy-5-methyl-isoxazol-4-yl) propanoic acid receptor
AVCN	Anteroventral cochlear nucleus
BSA	Bovine serum albumin
CaMKII	Ca/calmodulin-dependent protein kinase II
CNS	Central nervous system
DIADEM	DIgital reconstruction of Axonal and DEndritic Morphology
DMV	Dorsal motor nucleus of the vagus
EM	Electron microscopy
EPSC	Excitatory postsynaptic current
EPSP	Excitatory postsynaptic potential
GABA(R)	Gamma amino butyric acid receptor
GBC	Globular bushy cells
GlyR	Glycine receptor
HMM	Hidden Markov Model
IHC	Inner hair cell
ILD	Interaural level difference
IPSC	Inhibitory postsynaptic current
IPSP	Inhibitory postsynaptic potential
ITD	Interaural time difference
KCC2	Potassium chloride cotransporter 2
LGN	Lateral geniculate nucleus
LNTB	Lateral nucleus of the trapezoid body
LSO	Lateral superior olive
LTD	Long-term depression
LTP	Long-term potentiation
MNTB	Medial nucleus of the trapezoid body
MSO	Medial superior olive

NA	Numerical aperture
nACh(R)	Nicotinic acetylcholine receptor
NKCC1	Sodium potassium cotransporter 1
NMDA(R)	N-methyl D-aspartate receptor
NTS	Nucleus tractus solitarius
PBS	Phosphate-buffered Saline
PSD-95	Postsynaptic density protein 95kDA
PSTH	Peristimulus time histogram
RGC	Retinal ganglion cells
RI	Refractive index
SBC	Spherical bushy cells
SBEM	Serial block-face scanning electron microsocpy
SCE	Single cell electroporation
SEM	Standard error of the mean
SNR	Signal to noise ratio
SNT	Simple neurite tracer
VGLUT1	Vesicular glutamate transporter 1
VIAAT	Vesicular inhibitory amino acid transporter

Glossary

Critical period

a time window during which if the sensory system is not exposed to normal sensory experience the organism fails to gain proper sensory function.

Electroporation

a method to deliver dyes and/or genetic materials into cells with the application of electrical field.

Immunostaining

a method that uses antibodies to detect specific antigens (usually proteins). In the context of this thesis, I used fluorescent antibodies to label synaptic proteins so that I could image the fluorophores with confocal microscope.

Neural circuit

the connection(s) between neurons that when activated can perform a specific task.

Neuronal reconstruction

the process of creating a model (often in 3D) to allow neuroscientists to evaluate biophysical properties of the neuron, including dendritic length, dendritic branches, dendritic diameter, etc.

Patch clamp

a technique developed by Neher and Sakmann to study the subthreshold electrophysiological response of a cell or a patch of cell membrane. Can be used to measure current flowing through ion channels or changes in membrane potential of the cell or patch of membrane.

Plasticity

the phenomenon in which a neuron, neural circuit, or neural system changes its behavior as a result of experience (i.e., neural activity). Synaptic plasticity for a neural circuit involves a change in strength of synaptic connections in the circuit, as a result of previous neural activity.

Receptor subunit

the building block of a receptor (protein complex). Different receptor subunits may have different functions (e.g., ligand-binding, voltage-sensing, ion selectivity…).

Spine

a small protrusion from the dendritic shaft. For many neurons, spines are associated with excitatory synapses (though not for aspiny neurons such as LSO principal cells)

Tonotopy

a topographic arrangement found in most stages of the auditory system. This arranges maps the frequencies of auditory stimuli onto neural tissue, preserving nearest-neighbour relationships, in an orderly fashion. The result is that a ‘tonotopic axis’ can be determined, along which stimulus representation increases from lowest to highest frequency. Thus, as we move along this axis, we continue to encounter neurons that respond preferentially to tones of higher and higher frequency.

Declaration of contribution of research

For Chapter 2, I designed and implemented the electroporator, I performed the experiment, I analyzed the data, and I wrote the manuscript. The manuscript is prepared for submission to HardwareX.

For Chapter 3, I evaluated software programs, I designed and implemented the segmentation algorithms, and I analyzed the data.

For Chapter 4, I designed the experiment with Dr. Deda Gillespie, I performed the experiments, and I analyzed the data.

1 Chapter 1: Introduction

1.1 Circuit refinement at excitatory synapses

Neural circuits critically depend on the connections between neurons, which determine the tasks the circuits can perform. These connections between neurons are not hardwired, however, and can be substantially altered by neural activity, especially during early life. As postulated by Hebb, the repetition of activity in neuron A that continually causes the firing of neuron B can increase the ability of neuron A to cause neuron B to fire (Hebb, 1949). Hebbian activity-dependent plasticity has been implicated in the refinement of many neural circuits.

Within the central nervous system (CNS), glutamatergic synapses constitute the primary type of excitatory synapse. Glutamate activates cation-permeable ionotropic glutamate receptors, including α-amino-3-hydroxy-5-methyl-4-isoxazolepropionic acid receptors (AMPARs), N-methyl-D-aspartic acid receptors (NMDARs), and kainate receptors (For review, See Traynelis et al., 2010). Binding of two molecules of glutamate causes direct activation of AMPARs. Activation of NMDARs, in contrast, requires the binding of both glutamate and its co-agonist glycine, and it additionally requires the removal of Mg^{2+} that normally blocks the channel pore in the resting state. Thus, glutamate binding, glycine binding, and membrane depolarization are all required for Ca^{2+} influx through NMDARs (Mayer et al., 1984, 1987). Activation of both AMPA and NMDA receptors is required for canonical long-term potentiation (LTP), a form of Hebbian plasticity extensively studied at Schaffer collateral synapses in the hippocampus.

Developmental activity-dependent refinement in sensory systems has been best studied in the visual and somatosensory systems. Rodents that use whisking behavior to explore their environment exhibit a specialized cytoarchitecture in corresponding areas of somatosensory cortex, where layer IV is organized in barrel-like structures (Woolsey and Van der Loos, 1970; Welker and Woolsey, 1974; Rice et al., 1985). Each barrel, a ring of cell bodies surrounding a ‘hollow,’ receives glutamatergic inputs from thalamocortical axons, each of which relays information from single whiskers. Neighbouring barrels, which receive information from neighbouring whiskers, are separated by a septum. Early studies showed that removal of whiskers at birth causes a loss of the corresponding barrels, suggesting that sensory activity is required for barrel formation (Van der Loos and Woolsey, 1973). Subsequent studies revealing that whisker manipulation is maximally effective when it occurs at birth (postnatal day 0 (P0)) and is less effective by P6, established a critical period for barrel formation between P0 and P6 (Fox, 1992; Schlaggar et al., 1993). Several lines of evidence support a mechanistic role for activity-dependent glutamatergic transmission acting through canonical forms of LTP and LTD in critical-period plasticity in barrel cortex. First, genetic deletion of vesicular glutamate transporter 1 (VGLUT1) and VGLUT2 disrupts barrel formation, suggesting that thalamocortical axons require glutamatergic transmission in order to cluster (Li et al., 2013). Normal glutamatergic transmission shifts from mostly NMDAR- to mostly AMPAR-mediated transmission (Agmon and O’Dowd, 1992; Isaac et al., 1997). Furthermore, NMDAR-dependent LTP and LTD can be induced only during the critical period for barrel formation (Crair and Malenka, 1995; Feldman et al., 1998), and NMDARs undergo a subunit switch from GluN2B- to GluN2A-containing receptors (Barth and Malenka, 2001; Lu et al., 2001). Finally, genetic knockout of NMDAR subunits GluN1 and GluN2B results in reduced spine density of layer IV neurons (Espinosa et al., 2009; Mizuno et al., 2014). Together, these results support a critical role for NMDAR-dependent plasticity in developmental refinement of barrel cortex.

1.2 Circuit refinement at inhibitory synapses

The two primary mediators of inhibitory synaptic transmission in the CNS are glycine and γ- aminobutyric acid (GABA). Glycine can activate chloride permeable glycine receptors (glyRs) (Young and Snyder, 1973), pentameric proteins with α and β subunits (For review, see Betz, 1992). Whereas α subunits can form homo-oligomeric glyRs, β subunits require co-expression of α subunits for hetero-oligomeric glyRs. GABA can activate chloride-permeable ionotropic $GABA_A$ receptors and metabotropic $GABA_B$ receptors. The $GABA_A$ receptors are pentameric with 19 genes for $GABA_AR$ subunit proteins (For review, see Olsen and Sieghart, 2009). The heterodimeric $GABA_B$ receptors are G protein-coupled receptors, with $GABA_{B1}$ binding to ligand and $GABA_{B2}$ coupling to the G protein (For review, see Frangaj and Fan, 2018). Whereas inhibition in cortex and hypothalamus is accomplished through GABAergic transmission, brain regions in the retina, spinal cord brainstem, cerebellum, and thalamus can exhibit GABAergic or glycinergic – or mixed – transmission (Wassle et al., 1998; Sanes et al., 1987; Van Den Pol and Gorcs, 1988; Decavel and Van Den Pol, 1990; Dumoulin et al., 2001; Giber et al., 2015; Kubota et al., 2016).

Some immature inhibitory synapses undergo a shift in the neurotransmitter used during development. Though the dorsal motor nucleus of the vagus (DMV) receives input from the Nucleus tractus solitarius (NTS) that is mostly GABAergic in adult (Travagli et al., 1991), DMV neurons receive mixed GABAergic and glycinergic inputs during early development, with glycinergic transmission decreasing across development (McMenamin et al., 2016). A shift from GABA to glycine is common in various areas of the brainstem. For example, neurons in the lateral portion of the NTS initially receive purely GABAergic inputs, and gradually shift to receiving a mix of GABAergic and glycinergic inputs (Dufour et al., 2010). In the auditory brainstem, neurons of various nuclei – including spherical bushy cells of the anteroventral cochlear nucleus, principal cells of the medial nucleus of the trapezoid body, and principal neurons of the lateral superior olive – use predominantly GABAergic transmission in early life, followed by nearly purely glycinergic transmission in the adult (Kotak et al., 1998; Nabekura et al., 2004; Awatramani et al., 2005; Nerlich et al., 2017). Although plausible schemata have been proposed for how the shift in neurotransmitter might influence developmental refinement (Gillespie and Kandler, 2009), the shift itself has not been well-studied, and its phenomenology and function remain poorly understood.

As at other synapses throughout the nervous system, receptor subunits at inhibitory synapses undergo developmental changes in expression. In adult rats, glyRs with α1 subunit are highly expressed in the spinal cord as well as inferior and superior colliculi (Malosio et al., 1991). In contrast, glyRα2 subunit expression is abundant at birth and declines during postnatal development. In neonatal rats, $GABA_A$Rs with α1 subunit exhibit low expression at birth and the expression level increases during development (Fritschy et al., 1994). In contrast, $GABA_A$Rα2 subunit expression is widespread and abundant at birth but declines soon thereafter. As glyR α1 and $GABA_A$ α1 exhibit faster kinetics than the fetal subunits, the subunit switch in the inhibitory synapses underlies the acceleration of kinetics of inhibitory postsynaptic currents (IPSCs) (Takahashi et al., 1992; Okada et al., 2000).

As with glutamatergic synapses, many inhibitory synapses undergo activity-dependent refinement. In auditory brainstem, neurons of the medial superior olive (MSO) receive inhibitory inputs from the medial nucleus of the trapezoid body (MNTB). Individual axons from the MNTB arborize widely within the MSO of very young gerbils (Werthat et al., 2008), such that inhibitory inputs landing on MSO neurons innervate both somata and dendrites at early ages (Kapfer et al., 2002). By contrast, in adult gerbils, axon arbors of the MNTB projection are narrowly confined, with inhibitory synapses found only on the somata of MSO neurons (Kapfer et al., 2002; Werthat et al., 2008). Unilateral cochlea ablation and omnidirectional noise rearing prevent this reorganization of inhibitory synapses in MSO, suggesting that activity is required for this refinement. Activity-dependent developmental refinement of inhibitory synapses has also been shown in the visual cortex, where GABAergic basket cells innervate the somata and proximal dendrites of pyramidal neurons (Tamás et al., 1997). Although the GABAergic basket cells initially form multiple small synapses onto pyramidal neurons, only a subset of these synapses remain after many are eliminated during development (Wu et al., 2012). Genetic deletion of vesicular inhibitory amino acid transporter (VIAAT) prevents elimination of these early synapses, pointing to a requirement for GABAergic activity in synapse elimination (Wu et al., 2012).

Although the phenomenon of long-term plasticity has been described for inhibitory synapses, the mechanisms of long-term plasticity are less well-understood for inhibitory synapses than for glutamatergic synapses, though a role for Ca^{2+} has been shown in at least some cases. Early results from sensory neurons of the dorsal root ganglion of bullfrog showed that Ca^{2+} influx could suppress the $GABA_A$R-mediated Cl^- conductance (Inoue et al., 1986) whereas a later study in mammalian tissue showed Ca^{2+} influx could transiently increase the amplitude of $GABA_A$R-mediated current in Purkinje cells (Llano et al., 1991). These results established that inhibitory synapses could undergo long-term plasticity that was either depressing or potentiating. In guinea pig hippocampus, tetanic stimulation in the striatum induces inhibitory LTP in CA1 neurons (Xie and Sastry, 1991). In the deep cerebellar nuclei, 10 Hz stimulation induces LTD of $GABA_A$R-mediated transmission that is abolished by application of a Ca^{2+} chelator (Morishita and Sastry, 1996). Stellate cells in the cerebellar cortex receive glutamatergic inputs from parallel fibres and can form autaptic inhibitory synapses (Pouzat and Marty, 1998). Parallel fibre stimulation induces at these autaptic inhibitory synapses an LTP that likely depends on NMDARs (Liu and Lachamp, 2006).

Among the many developmental changes affecting inhibitory synapses, cellular changes in intracellular Cl^- concentration are especially significant. Many biological cells dynamically regulate intracellular Cl^- concentration through an array of channels and transporters (Duran et al., 2010). For immature neurons in particular the balance of Cl^- influx and efflux through Na^+-K^+-Cl^- (NKCC) and K^+-Cl^- (KCC) cotransporters sets the Cl^- reversal potential and hence the driving force for synaptic inhibition. In general, immature neurons, with low functional expression of KCC2, exhibit high intracellular Cl- concentrations, and the maturation of KCC2 expression shifts GABA- and/or glycinergic inputs from their immature depolarizing phenotype to their normal hyperpolarizing phenotype (Rivera et al., 1999). The same is true in the immature LSO, where activation of GABARs and glyRs leads to Cl^- efflux and postsynaptic depolarization (Ehrlich et al., 1999). The developmental change of KCC2 expression switches glyR and GABAR activation from depolarizing to hyperpolarizing. Interestingly, KCC2 expression is itself influenced by glyR and GABAR activation (Ganguly et al., 2001; Allain et al., 2016), and KCC2 expression can also affect glyR expression (Schwale et al., 2016).

1.3 Coordinate refinement of excitatory and inhibitory synapses

Throughout the CNS, the coordination of excitation and inhibition enables the neural circuit to function normally. Mature neurons are robust to perturbation of inputs, and tend to actively restore excitatory/inhibitory balance (Salinas and Sejnowski, 2000); however, how the excitatory/inhibitory balance is achieved initially during development is not well understood. As discussed previously, excitatory circuit refinement has been extensively studied, and although less is known about inhibitory circuit refinement, some progress has been made. As to how a neural circuit coordinately refines its excitatory and inhibitory inputs, nearly nothing is known, and yet, coordinate refinement of excitatory and inhibitory inputs is a fundamental question for understanding developmental refinement. In this section, I will highlight some studies in the visual system and auditory system that have begun to explore this question.

Coordinated refinement of excitatory and inhibitory inputs has been observed in the retina and downstream visual areas. Retinal ganglion cells (RGCs), the major output neuron of the retina, receive excitatory inputs from bipolar cells and inhibitory inputs from amacrine cells and send their output to neurons in lateral geniculate nucleus (LGN) (Levick et al., 1972; Wassle et al., 1998). Soto and colleagues genetically labelled excitatory and inhibitory synapses onto immature RGCs, estimated the ratio of excitatory to inhibitory synapses, and showed that RGCs maintain a stable excitatory to inhibitory synapse ratio throughout postnatal development, suggesting that RGCs coordinately refine their excitatory and inhibitory inputs (Soto et al., 2011). Neurons in the downstream LGN receive – in addition to excitatory inputs from RGCs – inhibitory inputs from local interneurons (Bickford et al., 2010). During postnatal development, the excitatory input convergence to neurons in LGN decreases while the inhibitory convergence increases (Tschetter et al., 2018). This complementary refinement of excitatory and inhibitory inputs may underlie the decrease in receptive field size for LGN neurons.

Froemke and colleagues have characterized refinement of excitatory and inhibitory inputs in auditory cortex, showing that sensory experience drives the coordinated refinement of excitatory and inhibitory synaptic input (Dorrn et al., 2010). Whereas in adult rat auditory cortex, inhibition is sharply tuned and is correlated with the excitation, in young rats, inhibition is largely untuned for frequency, and excitation and inhibition are uncorrelated. Exposing young rats to patterned auditory stimulation increases the correlation between excitation and inhibition, suggesting that the precisely coordinated refinement of cortical excitation and inhibition requires acoustic activity. The lab moved to slice studies to address mechanisms of coordinated refinement (Field et al., 2020). Using an array of stimulation electrodes to elicit individual EPSCs and IPSCs in pyramidal neurons, they investigated spike-timing dependent pairing of excitation and inhibition, showing that forward pairing could induce synaptic modification at multiple synapses, augmenting the correlation of excitation and inhibition. This heterosynaptic plasticity was mediated by Ca^{2+} transients in dendrites and was blocked by the application of APV, suggesting that the NMDAR-mediated Ca^{2+} transients are required for this heterosynaptic plasticity.

1.4 Auditory brainstem circuitry

For many animals, positional auditory information critically underlies survival and communication. For example, the ability to segment auditory objects from a noisy background, which many organisms rely upon for navigation and/or prey capture, crucially depends on the ability to localize sound sources. A diverse group of mammals, including bats, cetaceans, and shrews, among others, and some birds, produce and analyze echolocation signals for navigation. Whereas some acoustic hunters analyze self-generated sounds, others localize prey-generated sounds to successfully capture food. Barn owls are capable acoustic hunters, responding to relevant sounds within 100 msec with head saccades and exhibiting localization errors under 2° (Knudsen et al., 1979). Finally, in the communication realm, sound localization is critically required to attend to and track conspecifics' voices. A classic example for humans is the so-called 'cocktail party problem,' where in a closed environment with many voices, sound localization allows individuals to filter less relevant auditory information and attend to the relevant conversation. In order to perform sound localization in the real world, the nervous system must be able to detect signals on the order of a few microseconds and must process the complex auditory signal on a timecourse of tens of milliseconds.

Acoustic waves travel through the outer ear and are transformed to a mechanical signal in the middle ear and to an electrical signal in the inner ear. The outer ear collects sound waves and directs them through the ear canal to the tympanic membrane. The tympanic membrane is attached to the ossicles, three tiny bones (malleus, incus, and stapes) that form a mechanical advantage system for translating and amplifying vibrations at the tympanum to the oval window of the cochlea. The cochlea is a coiled structure with three adjacent tubes: scala vestibuli, scala media, and scala tympani. The scala media contains endolymph, fluid with high potassium concentration. The scala vestibuli, superior to the scala media, terminates at the oval window. The scala tympani, inferior to the scala media, terminates at the round window. The scala vestibuli and the scala tympani contain perilymph, fluid with ionic concentration similar to that of cerebrospinal fluid, and merge at the helicotrema, the apex of the cochlea. The basilar membrane separates the scala media and the scala tympani. The stapes strikes the oval window, which in turn compresses the perilymph in the scala vestibuli. Because the scala vestibuli and the scala tympani are merged through helicotrema, the compression of the perilymph in scala vestibuli also vibrates the perilymph in the scala tympani and eventually vibrates the round window. The pressure difference between the scala vestibuli and the scala tympani vibrates the basilar membrane transversely. As first appreciated by German physiologist Hermann Von Helmholtz, what the cochlea does is essentially the reverse of what the piano does. Whereas the piano convolves simple tones into musical pieces through the vibration of strings, the cochlea deconvolves a complex acoustic signal by segregating each of its component tones within different segments of the basilar membrane. The main mechanical element of the cochlea, the basilar membrane is stiffest at the base of the cochlea, where it responds to high-frequency sound, and is least stiff at the apex of the cochlea, which responds to low frequency sound (Wever et al., 1954; Bekesy, 1956, 1970). Just as sound frequencies map along the piano keyboard, sound frequencies map along the basilar membrane, constructing a frequency gradient, or tonotopic map, that is preserved throughout most of the auditory system. Hair cells in the cochlea convert the vibration of the basilar membrane to an electrical signal and transmit it to spiral ganglion neurons, whose axons make up the auditory (VIIIth) nerve. The target of the auditory nerve, the cochlear nucleus, consists of three subdivisions with differing function and anatomy: 1) the dorsal cochlear nucleus, a cerebellum-like organization that integrates multimodal sensory information (Oertel and Young, 2004); 2) the posteroventral cochlear nucleus, containing primarily stellate cells and broadband-tuned, onset-sensitive octopus cells and stellate cells (Brawer et al., 1974; Godfrey et al., 1975; Oertel et al., 1990; Oertel et al., 2000); and 3) the anteroventral cochlear nucleus (AVCN), with which we will be concerned here for sound localization in azimuthal plane.

The proximate input to the azimuthal sound localization circuit of the auditory brainstem arises in the AVCN. Bushy cells of the AVCN receive excitatory, glutamatergic inputs from spiral ganglion neurons and relay auditory information to the superior olivary complex (SOC), a binaural structure in the auditory brainstem that is essential for sound localization (Cant and Morest, 1979; Spirou et al., 2005; Lauer et al., 2013). The glutamatergic bushy cells are of two main types: spherical bushy cells (SBCs) project bilaterally to the medial superior olive (MSO) on both sides as well as to the ipsilateral lateral superior olive (LSO) (Cant and Casseday, 1986), and globular bushy cells (GBCs) project to the contralateral medial nucleus of the trapezoid body (MNTB) (Tolbert et al., 1982). In addition to their distinct morphology and circuitry, the two types of bushy cells exhibit different physiological behaviours in response to short tone bursts at the neuron’s characteristic frequency (Kiang et al., 1965). In particular, the peristimulus time histogram (PSTH) of SBCs reveals a “primary-like response” that resembles the responses of primary auditory nerve fibres to pure tones (Smith et al., 1993), whereas most GBCs have a “primary-with-notch” response, wherein the cell shows a high frequency onset response that drops to near zero for about one millisecond and then rebounds to a low-level sustained response (Smith et al., 1993). In general, bushy cells – like auditory nerve fibres – fire in phase with the sound stimulus at lower stimulus frequencies (Joris et al., 1994), and hence are said to “phase-lock” to the stimulus.

Information for azimuthal sound localization is extracted in the SOC, using binaural cues that result from the physical separation of the two acoustic sensors (tympanic membranes). The interaural time difference (ITD) cue arises from differences in path-length from the sound source to the two ears, and the range of relevant ITDs is determined by head size (Masterton and Diamond, 1967). The interaural level difference (ILD) cue arises from differences in sound intensity at the two ears. Attenuation as $1/r^2$ can provide measurable cues only for sound sources that are quite near the sensors, and hence most effective ILDs arise from the sound shadow cast by the head. For acoustic stimuli of wavelength head size or smaller, the acoustic wave at the ipsilateral ear is reflected by the head, resulting in an attenuated (lower intensity) sound pressure wave at the contralateral ear. This head-shadow effect makes ILD cues useful for high-frequency sound sources, regardless of distance.

The mammalian SOC contains several major nuclei, of which the most prominent in rodent are the LSO, MSO, MNTB, and superior paraolivary nucleus (SPN) (fig 1). The primary role of the MSO is understood to be computation of interaural time differences (ITD) for low frequency stimuli, whereas that of the LSO is understood to be computation of interaural level difference (ILD) for high-frequency stimuli as well as ITD of the envelope for amplitude-modulated tones (Boudreau and Tsuchitani, 1968; Goldberg and Brown, 1969; Caird and Klinke, 1983; Joris and Yin, 1995).

Principal neurons in the MSO are sensitive to ITDs. These neurons receive bilateral excitatory inputs from spherical bushy cells in AVCN and bilateral inhibitory inputs from MNTB and lateral nucleus of the trapezoid body (LNTB) (Goldberg and Brown, 1969; Yin and Chan, 1990; Kuwabara and Zook, 1992; Spirou and Berrebi, 1997). Lloyd Jeffress proposed a model for ITD detection in which an array of coincidence detector neurons receives inputs from the two ears. Inputs to different coincidence detectors arrive with different delays, such that the signal from the ear ipsilateral to the sound source, though transduced earlier at the cochlea due the shorter path traveled from the sound source, is delayed on its way to the MSO, presumably by imposing a longer physical path (Jeffress, 1948). In essence, these anatomical neural delay lines compensate for the acoustic delays that give rise to the ITD in the first place. Each individual coincidence detector neuron fires only when its two inputs arrive simultaneously. In the original Jeffress model, ITDs are mapped onto the array of coincidence detectors. As the sound source shifts from the medial to lateral, firing in the neural array shifts from medial to lateral. The internal delay line also presumes that the bilateral presynaptic neurons fire at the same delay to a given stimulus. The phase-locking property of bushy cells critically underlies the Jeffress model. In the avian brain, the excitatory inputs to Nucleus laminarus, the analogue of mammalian MSO, follow the Jeffress model: internal delay lines compensate for the acoustic delay (ITD), and neurons in Nucleus laminarus fire upon the coincident detection of bilateral excitatory inputs (Seidl et al., 2010). Interestingly, the axon length of the contralateral pathway is longer than that of the ipsilateral pathway. However, the contralateral axon exhibits a larger mean axon diameter and a longer mean internode distance than the ipsilateral axon. Together, the conduction time difference at the two pathways falls into the physiological range for ITD computation. The Jeffress model has less than perfect explanatory power in mammals, where the acoustic delays are not clearly compensated neurally (Karino et al., 2011). Mammalian MSO principal cells receive dense somatic inhibition, and pharmacological blockade of glycine receptors both broadens ITD tuning, and shifts peak responses toward ITDs of 0 µsec, showing that strong somatic inhibition contributes to ITD tuning, though in ways that are still incompletely understood (Brand et al., 2002; Kapfer et al., 2002; Roberts et al., 2013; Franken et al., 2015; Goldwyn et al., 2017).

Principal neurons in the LSO are sensitive to ILDs. These neurons receive excitatory input from spherical bushy cells in the ipsilateral AVCN (Cant and Casseday, 1986) and inhibitory input from the ipsilateral MNTB, which themselves receive excitatory input from globular bushy cells in the contralateral AVCN (Moore and Caspary, 1983; Bledsoe et al., 1990; Sommer et al., 1993; Smith et al., 1998). Extracellular single-unit electrophysiology from the LSO of various species has supported the idea that most LSO cells fire in a sustained manner in response to auditory stimuli (Tsuchitani, 1977; Greene and Davis, 2012). More recent *in vivo* patch recordings in LSO suggest that LSO principal neurons may fire only at the onset of the sound (Franken et al., 2018). This newer finding suggested that principal neurons of LSO may act primarily as differentiators rather than integrators and placed renewed emphasis on the importance of timing of LSO inputs. The relative timing of inhibitory postsynaptic potentials (IPSPs) and excitatory postsynaptic potentials (EPSPs) arriving at the individual LSO principal neurons are correlated to the sound pressure differences between two ears. When the sound pressure at the contralateral ear is greater than the sound pressure at the ipsilateral ear, IPSPs at the LSO principal neuron precede excitatory postsynaptic potentials (EPSPs). As the sound pressure at the contralateral ear decreases, the latency of IPSPs at the LSO principal neuron increases, and when the sound pressure at the contralateral ear is less than the sound pressure at the ipsilateral ear, EPSPs precede IPSPs. This delayed IPSP, when the sound pressure at the ipsilateral ear is higher that of the contralateral ear, fails to suppress the EPSP, allowing the principal neuron to fire an action potential.

Although LSO neurons are associated primarily with ILD computation, many LSO neurons also sensitive to ITDs for the carrier frequency, and most may be sensitive to ITDs in the envelope. Classic studies performed in the barbiturate-anesthetized cat suggested that neurons in LSO are sensitive to ITD of amplitude-modulated tones. Joris and Yin presented sinusoidal amplitude-modulated stimuli to anesthetized cats and recorded cells in LSO *in vivo* (Joris and Yin, 1995; Joris, 1996). Their recording revealed that the firing rate of LSO neuron in response to ITD was periodic corresponding to the modulate stimuli, suggesting neurons in LSO were ITD sensitive. With low modulation frequency, neurons in LSO fired maximally when the modulation stimuli at two ears were 180° out of phase. Increasing the modulation frequency beyond 300 Hz decreased firing rate, suggesting the envelope ITD computation in LSO has a much lower range compared to ITD computation in MSO.

In order to compute appropriate ILDs (i.e., in which the compared signals arise from the same sound source), the two phenotypically different inputs to individual LSO neurons must be precisely matched for characteristic frequency (i.e., the stimulus frequency that drives a neural response with highest probability) (Tollin, 2003). This requirement imposes an additional burden on the process of developmental circuit optimization, as the cell must ensure not only that excitation and inhibition achieve balance, but also that they achieve frequency-based (tonotopic) registration. What do we know about this process? This question can be answered only with *in vivo* electrophysiology (or optical physiology) using appropriately calibrated binaural acoustic stimuli in juvenile animals. Recording from juvenile animals presents technical difficulties that are exacerbated in this instance by the depth and size of the target nucleus. Thus, to date, only a single study has examined this question, and that study was performed in gerbil – a low-frequency, MSO, specialist – rather than in an LSO specialist (Sanes and Rubel, 1988). Nevertheless, this study provides a sense of what likely happens in higher-frequency-hearing rodents. Like rats and mice, gerbils begin to transduce and process acoustic information around postnatal day 12 (P12). Immediately after hearing onset, excitatory and inhibitory inputs to the LSO were relatively broadly tuned and the two were crudely matched for stimulus frequency. Along with their broader frequency tuning, juvenile gerbils exhibited a narrower dynamic range and poorer precision of ILD tuning than adults. Thus, although no precise window has been established, the primary period during which excitatory and inhibitory inputs are brought into registration is generally thought to be the first week after hearing onset.

As with developmental processes throughout the nervous system, we can characterize developmental circuit refinement in the LSO circuit by two major stages: an initial stage including both “axon guidance” to target neural processes to appropriate locations and “synaptogenesis” to establish synaptic connections among neurons, and a later stage of circuit refinement that occurs largely through re-weighting of synaptic strength. Axon guidance in the auditory brainstem occurs perinatally: axon collaterals of the cochlear nuclei form and begin to innervate auditory brainstem nuclei in the late embryonic period, and by postnatal day 3 (P3), neurons of the cochlear nucleus have formed appropriate afferent projections to nuclei of the superior olive (Kandler and Friauf, 1993). This process is likely regulated by signaling through the Eph receptor family of high-affinity receptor tyrosine kinases and their ephrin ligands (Cramer, 2005; for review, Pasquale, 2005). Sixteen Eph receptors (EphA1-10 and EphB1-6) and eight ephrins (ephrin-A1-5 and ephrin-B1-3) have been described in vertebrates, with various ephrin/Eph receptor combinations subserving different developmental stages and processes. In the auditory brainstem, mice lacking EphA4 exhibit a shifted frequency response in the MNTB, as revealed by staining for the immediate early gene c-fos, which indicates suprathreshold neural activity (Morgan and Curran, 1989; Miko et al., 2007). Null mutations for EphB2 or EphB3, as well as mutations in ephrin-B2, on the other hand, exhibit mis-targeted projections to the MNTB from ipsilateral AVCN (Hsieh et al., 2010). Mechanisms of synaptogenesis, presumed to be conserved throughout the central nervous system, likely involve immature glial cells, though precise cues are still debated (Christopherson et al., 2005).

To understand the ultimate (refinement) stage of postnatal circuit development, we must know how both the excitatory and inhibitory inputs are refined. Though much is still murky about developmental refinement of the excitatory AVCN-LSO projection, physiological recordings in living slice have shown that the number of excitatory inputs received by individual LSO neurons decreases, and the remaining input strength increases, before hearing onset (Case et al., 2011). At birth, glutamatergic transmission in this pathway is mediated primarily NMDARs, and mostly by GluN2B-containing NMDARs, whereas between birth and hearing onset, expression of GluR4-containing AMPARs increases, and transmission shifts primarily to AMPARs (Caicedo and Eybalin, 1999; Case et al., 2011). It should be noted that the LSO also receives noradrenergic inputs from locus coeruleus (Woods and Azeredo, 1999; Mulders and Robertson, 2001), and that lesioning noradrenergic nerve terminals and chronically inhibiting α_2-adrenoceptors disrupts developmental refinement in the AVCN-LSO pathway (Hirao et al., 2015).

Because the MNTB-LSO pathway has been used for some time as a model for studies of inhibitory circuit refinement, refinement of the major inhibitory input to LSO principal cells is – unusually – better characterized than that of their major excitatory input. Like the excitatory AVCN-LSO pathway, the inhibitory circuit undergoes substantial refinement before hearing onset: the proportional area of MNTB capable of eliciting a response in an individual LSO neuron decreases two-fold, and strength of the remaining synapses increases by an order of magnitude. Most of this refinement occurs during the first postnatal week and is complete by hearing onset in rats and mice (Kim and Kandler, 2003, 2010). During this period, transmission shifts from GABAergic to glycinergic, and expression of α1-containing glyRs increases (Friauf et al., 1997; Kotak et al., 1998). Surprisingly, the immature inhibitory pathway in LSO releases not only GABA and glycine but also glutamate, enabled by the transient expression of vesicular glutamate transporter 3 (VGLUT3) (Gillespie et al., 2005), which is likely packaged into different vesicles than GABA/glycine (Case and Gillespie, 2011). As genetic deletion of VGLUT3 disrupts normal refinement in the inhibitory pathway (Noh et al., 2010), glutamate release is thought to play a critical role in inhibitory plasticity here. Finally, the cotransporter KCC2 while present is incompletely functional in the first postnatal week. During this period, LSO neurons exhibit a high intracellular Cl^- concentration (Balakrishnan et al., 2003), and $GABA_A$Rs and glyRs depolarize LSO principal cells (Kandler and Friauf, 1995; Ehrlich et al., 1999; Löhrke et al., 2005).

What drives the physiologically measurable refinement before hearing onset? This refinement is understood to be activity-dependent, and yet the activity cannot be acoustically driven. The answer is provided by spontaneous activity, which can drive physiologically measurable refinement before hearing onset. In fact, patterned spontaneous activity originating from the Kölliker's organ, a transient structure in the developing cochlea, is required for the normal tonotopic refinement in MNTB-LSO pathway (Tritsch and Bergles, 2010; Clause et al., 2014; Fischer et al., 2019).

Circuit refinement that is physiologically measurable before hearing onset is translated into anatomically measurable refinement largely after hearing onset. After hearing onset, MNTB axon terminal boutons are found to be more confined within narrow isofrequency bands in the LSO, suggesting a further tonotopic sharpening or a crystallization of previous tonotopic sharpening (Sanes and Siverls, 1991). In gerbils, unilateral cochlea ablation decreases the degree of refinement of terminal bouton spread, supporting a model in which anatomically measurable refinement is activity-dependent (Sanes and Takács, 1993). Finally, during the first 1-2 weeks after hearing onset, the size of the dendritic field, the number of primary dendrites, and the number of dendritic endpoints decrease in LSO (Rietzel and Friauf, 1998).

In the LSO, circuit refinement of the major input pathways during the first few postnatal weeks is known to involve synapse elimination and strengthening, as well as changes in protein expression and cell morphology. The physical redistribution of synapses could further contribute to this refinement. In this thesis, I examined the distribution, and redistribution, of inhibitory and excitatory synapses onto LSO cells of the rat in the period before hearing onset. In Chapter 2, I describe the design and implementation of a low-cost, Arduino-based single-cell electroporator that allowed me to label individual LSO neurons in acute living slices. In Chapter 3, I describe testing of various 3D neuronal reconstruction software packages to reconstruct labeled LSO neurons, and implementation of an improved iterative-thresholding-based algorithm to segment synapses in 3D. In Chapter 4, using the hardware and software solutions described in Chapters 2 and 3, I describe my investigation into the redistribution of excitatory and inhibitory synapses in LSO before hearing onset.

1.5 Figure

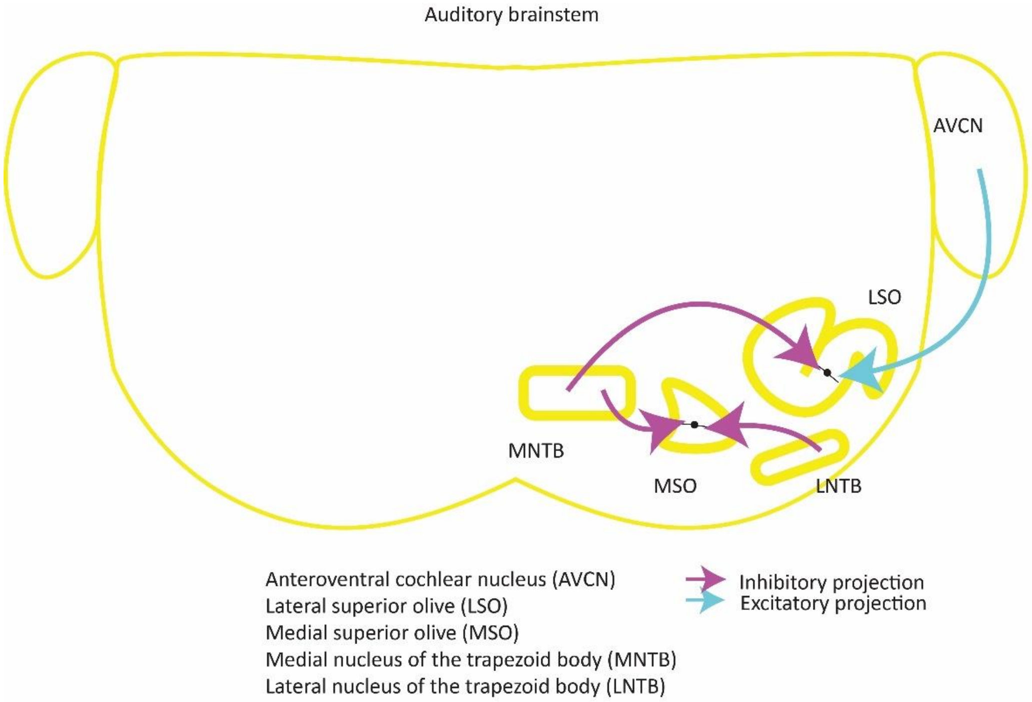

Figure 1. Schematic of auditory brainstem in coronal section. Principal neurons in LSO receive excitatory inputs from AVCN and inhibitory inputs from MNTB. Principal neurons in MSO receive bilateral inhibitory inputs from MNTB and LNTB.

1.6 References:

Agmon A, O'Dowd DK (1992) NMDA receptor-mediated currents are prominent in the thalamocortical synaptic response before maturation of inhibition. J Neurophysiol 68:345–349.

Allain AE, Cazenave W, Delpy A, Exertier P, Barthe C, Meyrand P, Cattaert D, Branchereau P (2016) Nonsynaptic glycine release is involved in the early KCC2 expression. Dev Neurobiol 76:764–779.

Awatramani GB, Turecek R, Trussell LO (2005) Staggered development of GABAergic and glycinergic transmission in the MNTB. J Neurophysiol 93:819–828.

Balakrishnan V, Becker M, Löhrke S, Nothwang HG, Güresir E, Friauf E (2003) Expression and function of chloride transporters during development of inhibitory neurotransmission in the auditory brainstem. J Neurosci 23:4134–4145.

Barth AL, Malenka RC (2001) NMDAR EPSC kinetics do not regulate the critical period for LTP at thalamocortical synapses. Nat Neurosci 4:235–236.

Bekesy G V (1970) Traveling Waves as Frequency Analysers in the Cochlea. Nature 225:1207–1209.

Bekesy G Von (1956) Current status of theories of Hearing. Science (80-) 123:779–783.

Betz H (1992) Structure and function of inhibitory glycine receptors. Q Rev Biophys 25:381–394.

Bickford ME, Slusarczyk A, Dilger EK, Krahe TE, Kucuk C, Guido W (2010) Synaptic development of the mouse dorsal lateral geniculate nucleus. J Comp Neurol 518:622–635.

Bledsoe SC, Snead CR, Helfert RH, Prasad V, Wenthold RJ, Altschuler RA (1990) Immunocytochemical and lesion studies support the hypothesis that the projection from the medial nucleus of the trapezoid body to the lateral superior olive is glycinergic. Brain Res 517:189–194.

Boudreau JC, Tsuchitani C (1968) Binaural interaction in the cat superior olive S segment. J Neurophysiol 31:442–454.

Brand A, Behrend O, Marquardt T, McAlpine D, Grothe B (2002) Precise inhibition is essential for microsecond interaural time difference coding. Nature 417:543–547.

Brawer JR, Morest DK, Kane EC (1974) The neuronal architecture of the cochlear nucleus of the cat. J Comp Neurol 155:251–299.

Caicedo A, Eybalin M (1999) Glutamate receptor phenotypes in the auditory brainstem and mid-brain of the developing rat. Eur J Neurosci 11:51–74.

Caird D, Klinke R (1983) Processing of binaural stimuli by cat superior olivary complex neurons. Exp Brain Res 52:385–399.

Cant NB, Casseday JH (1986) Projections from the anteroventral cochlear nucleus to the lateral and medial superior olivary nuclei. J Comp Neurol 247:457–476.

Cant NB, Morest DK (1979) The bushy cells in the anteroventral cochlear nucleus of the cat. A study with the electron microscope. Neuroscience 4:1925–1945.

Case DT, Gillespie DC (2011) Pre- and postsynaptic properties of glutamatergic transmission in the immature inhibitory MNTB-LSO pathway. J Neurophysiol 106:2570–2579.

Case DT, Zhao X, Gillespie DC (2011) Functional refinement in the projection from ventral cochlear nucleus to lateral superior olive precedes hearing onset in rat. PLoS One 6.

Christopherson KS, Ullian EM, Stokes CCA, Mullowney CE, Hell JW, Agah A, Lawler J, Mosher DF, Bornstein P, Barres BA (2005) Thrombospondins are astrocyte-secreted proteins that promote CNS synaptogenesis. Cell 120:421–433.

Clause A, Kim G, Sonntag M, Weisz CJC, Vetter DE, Rubsamen R, Kandler K (2014) The Precise Temporal Pattern of Prehearing Spontaneous Activity Is Necessary for Tonotopic Map Refinement. Neuron 82:822–835.

Crair MC, Malenka RC (1995) A critical period for long-term potentiation at thalamocortical synapses. Nature 375:325–328.

Cramer KS (2005) Eph proteins and the assembly of auditory circuits. Hear Res 206:42–51.

Decavel C, Van Den Pol a N (1990) GAB & ADominant Neurotransmitter i n the Hypothalamus. J Comp Neurol 302:1019–1037.

Dorrn AL, Yuan K, Barker AJ, Schreiner CE, Froemke RC (2010) Developmental sensory experience balances cortical excitation and inhibition. Nature 465:932–936.

Dufour A, Tell F, Baude A (2010) Perinatal development of inhibitory synapses in the nucleus tractus solitarii of the rat. Eur J Neurosci 32:538–549.

Dumoulin A, Triller A, Dieudonné S (2001) IPSC kinetics at identified GABAergic and mixed GABAergic and glycinergic synapses onto cerebellar Golgi cells. J Neurosci 21:6045–6057.

Duran C, Thompson CH, Xiao Q, Hartzell HC (2010) Chloride channels: Often enigmatic, rarely predictable. Annu Rev Physiol 72:95–121.

Ehrlich I, Löhrke S, Friauf E (1999) Shift from depolarizing to hyperpolarizing glycine action in rat auditory neurones is due to age-dependent Cl- regulation. J Physiol 520:121–137.

Espinosa JS, Wheeler DG, Tsien RW, Luo L (2009) Uncoupling Dendrite Growth and Patterning: Single-Cell Knockout Analysis of NMDA Receptor 2B. Neuron 62:205–217.

Feldman DE, Nicoll RA, Malenka RC, Isaac JTR (1998) Long-term depression at thalamocortical synapses in developing rat somatosensory cortex. Neuron 21:347–357.

Field RE, D’amour JA, Tremblay R, Miehl C, Rudy B, Gjorgjieva J, Froemke RC (2020) Heterosynaptic Plasticity Determines the Set Point for Cortical Excitatory-Inhibitory Balance. Neuron 106:842–854.

Fischer AU, Müller NIC, Deller T, Del Turco D, Fisch JO, Griesemer D, Kattler K, Maraslioglu A, Roemer V, Xu-Friedman MA, Walter J, Friauf E (2019) GABA is a modulator, rather than a classical transmitter, in the medial nucleus of the trapezoid body–lateral superior olive sound localization circuit. J Physiol 597:2269–2295.

Fox K (1992) A critical period for experience-dependent synaptic plasticity in rat barrel cortex. J Neurosci 12:1826–1838.

Frangaj A, Fan QR (2018) Structural biology of GABAB receptor. Neuropharmacology 136:68–79.

Franken TP, Joris PX, Smith PH (2018) Principal cells of the brainstem’s interaural sound level detector are temporal differentiators rather than integrators. Elife 7:1–25.

Franken TP, Roberts MT, Wei L, Golding NL, Joris PX (2015) In vivo coincidence detection in mammalian sound localization generates phase delays. Nat Neurosci 18:444–454.

Friauf E, Hammerschmidt B, Kirsch J (1997) Development of adult-type inhibitory glycine receptors in the central auditory system of rats. J Comp Neurol 385:117–134.

Fritschy JM, Paysan J, Enna A, Mohler H (1994) Switch in the expression of rat GABA(A)-receptor subtypes during postnatal development: An immunohistochemical study. J Neurosci 14:5302–5324.

Ganguly K, Schinder AF, Wong ST, Poo M ming (2001) GABA itself promotes the developmental switch of neuronal GABAergic responses from excitation to inhibition. Cell 105:521–532.

Giber K, Diana MA, M Plattner V, Dugué GP, Bokor H, Rousseau C V., Maglóczky Z, Havas L, Hangya B, Wildner H, Zeilhofer HU, Dieudonné S, Acsády L (2015) A subcortical inhibitory signal for behavioral arrest in the thalamus. Nat Neurosci 18:562–568.

Gillespie DC, Kandler K (2009) GABA, Glycine, and Glutamate Co-Release at Developing Inhibitory Synapses. In: Co-Existence and Co-Release of Classical Neurotransmitters (Gutierrez R, ed), pp 1–26. Boston, MA: Springer US.

Gillespie DC, Kim G, Kandler K (2005) Inhibitory sypnapses in the developing auditory system are glutamatergic. Nat Neurosci 8:332–338.

Godfrey DA, Kiang NYS, Norris BE (1975) Single unit activity in the posteroventral cochlear nucleus of the cat. J Comp Neurol 162:247–268.

Goldberg YM, Brown B (1969) Response of Binaural Neurons of Dog Superior Olivary Complex to Dichotic TOnal Stimuli: Some Physiological Mechanisms of Sound Localization. J Physiol.

Goldwyn JH, McLaughlin M, Verschooten E, Joris PX, Rinzel J (2017) Signatures of somatic inhibition and dendritic excitation in auditory brainstem field potentials. J Neurosci 37:10451–10467.

Greene NT, Davis KA (2012) Discharge patterns in the lateral superior olive of decerebrate cats. J Neurophysiol 108:1942–1953.

Hebb D (1949) The Organization of Behavior. New York: John Wiley & Sons, Inc.

Hirao K, Eto K, Nakahata Y, Ishibashi H, Nagai T, Nabekura J (2015) Noradrenergic refinement of glutamatergic neuronal circuits in the lateral superior olivary nucleus before hearing onset. J Neurophysiol 114:1974–1986.

Hsieh CY, Nakamura PA, Luk SO, Miko IJ, Henkemeyer M, Cramer KS (2010) Ephrin-B reverse signaling is required for formation of strictly contralateral auditory brainstem pathways. J Neurosci 30:9840–9849.

Inoue M, Oomura Y, Yakushiji T, Akaike N (1986) Intracellular calcium ions decrease the affinity of the GABA receptor. Nature 324:156–158.

Isaac JTR, Crair MC, Nicoll RA, Malenka RC (1997) Silent synapses during development of thalamocortical inputs. Neuron 18:269–280.

Jeffress LA (1948) A place theory of sound localization. J Comp Physiol Psychol 41:35–39.

Joris PX (1996) Envelope coding in the lateral superior olive. II. Characteristic delays and comparison with responses in the medial superior olive. J Neurophysiol 76:2137–2156.

Joris PX, Carney LH, Smith PH, Yin TCT (1994) Enhancement of neural synchronization in the anteroventral cochlear nucleus. I. Responses to tones at the characteristic frequency. J Neurophysiol 71:1022–1036.

Joris PX, Yin TCT (1995) Envelope Coding in the Lateral Superior Olive. I. Sensitivity to Interaural Time Differences. J Neurophysiol 73.

Kandler K, Friauf E (1993) Pre- and postnatal development of efferent connections of the cochlear nucleus in the rat. J Comp Neurol 328:161–184.

Kandler K, Friauf E (1995) Development Transmission of Glycinergic and Glutamatergic Synaptic in the Auditory Brainstem of Perinatal Rats. J Neurosci 15:6890–6904.

Kapfer C, Seidl AH, Schweizer H, Grothe B (2002) Experience-dependent refinement of inhibitory inputs to auditory coincidence-detector neurons. Nat Neurosci 5:247–253.

Karino S, Smith PH, Yin TCT, Joris PX (2011) Axonal branching patterns as sources of delay in the mammalian auditory brainstem: A re-examination. J Neurosci 31:3016–3031.

Kiang NKS, Pfeiffer RR, Warr WB, Backus ASN (1965) Stimulus Coding in the Cochlear Nucleus. Ann Otol Rhinol Laryngol 74:463–485.

Kim G, Kandler K (2003) Elimination and strengthening of glycinergic/GABAergic connections during tonotopic map formation. Nat Neurosci 6:282–290.

Kim G, Kandler K (2010) Synaptic changes underlying the strengthening of GABA/ glycinergic connections in the developing lateral superior olive. Neuroscience 171:924–933.

Knudsen EI, Blasdel GG, Konishi M (1979) Sound localization by the barn owl (Tyto alba) measured with the search coil technique. J Comp Physiol 133:1–11.

Kotak VC, Korada S, Schwartz IR, Sanes DH (1998) A developmental shift from GABAergic to glycinergic transmission in the central auditory system. J Neurosci 18:4646–4655.

Kubota Y, Karube F, Nomura M, Kawaguchi Y (2016) The diversity of cortical inhibitory synapses. Front Neural Circuits 10:1–15.

Kuwabara N, Zook JM (1992) Projections to the medial superior olive from the medial and lateral nuclei of the trapezoid body in rodents and bats. J Comp Neurol 324:522–538.

Lauer AM, Connelly CJ, Graham H, Ryugo DK (2013) Morphological Characterization of Bushy Cells and Their Inputs in the Laboratory Mouse (Mus musculus) Anteroventral Cochlear Nucleus. PLoS One 8:1–16.

Levick WR, Cleland BG, Dubin MW (1972) Lateral geniculate neurons of cat: retinal inputs and physiology. Invest Ophthalmol 11:302–311.

Li H, Fertuzinhos S, Mohns E, Hnasko TS, Verhage M, Edwards R, Sestan N, Crair MC (2013) Laminar and Columnar Development of Barrel Cortex Relies on Thalamocortical Neurotransmission. Neuron 79:970–986.

Liu SJ, Lachamp P (2006) The activation of excitatory glutamate receptors evokes a long-lasting increase in the release of GABA from cerebellar stellate cells. J Neurosci 26:9332–9339.

Llano I, Leresche N, Marty A (1991) Calcium entry increases the sensitivity of cerebellar Purkinje cells to applied GABA and decreases inhibitory synaptic currents. Neuron 6:565–574.

Löhrke S, Srinivasan G, Oberhofer M, Doncheva E, Friauf E (2005) Shift from depolarizing to hyperpolarizing glycine action occurs at different perinatal ages in superior olivary complex nuclei. Eur J Neurosci 22:2708–2722.

Lu HC, Gonzalez E, Crair MC (2001) Barrel cortex critical period plasticity is independent of changes in NMDA receptor subunit composition. Neuron 32:619–634.

Malosio ML, Marquèze-Pouey B, Kuhse J, Betz H (1991) Widespread expression of glycine receptor subunit mRNAs in the adult and developing rat brain. EMBO J 10:2401–2409.

Masterton B, Diamond IT (1967) Medial Superior Olive and Sound Localization Author. Science (80-) 155:1696–1697.

Mayer ML, MacDermott AB, Westbrook GL, Smith SJ, Barker JL (1987) Agonist- and voltage-gated calcium entry in cultured mouse spinal cord neurons under voltage clamp measured using arsenazo III. J Neurosci 7:3230–3244.

Mayer ML, Westbrookt GL, Guthriet PB (1984) Responses in Spinal Cord Neurones. Nature 309:261–263.

McMenamin CA, Anselmi L, Travagli RA, Browning KN (2016) Developmental regulation of inhibitory synaptic currents in the dorsal motor nucleus of the vagus in the rat. J Neurophysiol 116:1705–1714.

Miko IJ, Nakamura PA, Henkemeyer M, Cramer KS (2007) Auditory Brainstem Neural Activation Patterns Are Altered in EphA4- and Ephrin-B2-Deficient Mice. J Comp Neurol 505:669–681.

Mizuno H, Luo W, Tarusawa E, Saito YM, Sato T, Yoshimura Y, Itohara S, Iwasato T (2014) NMDAR-regulated dynamics of layer 4 neuronal dendrites during thalamocortical reorganization in neonates. Neuron 82:365–379.

Moore MJ, Caspary DM (1983) Strychnine blocks binaural inhibition in lateral superior olivary neurons. J Neurosci 3:237–242.

Morgan JI, Curran T (1989) Stimulus-transcription coupling in neurons: role of cellular immediate-early genes. Trends Neurosci 12:459–462.

Morishita W, Sastry BR (1996) Postsynaptic mechanisms underlying long-term depression of GABAergic transmission in neurons of the deep cerebellar nuclei. J Neurophysiol 76:59–68.

Mulders WHAM, Robertson D (2001) Origin of the noradrenergic innervation of the superior olivary complex in the rat. J Chem Neuroanat 21:313–322.

Nabekura J, Katsurabayashi S, Kakazu Y, Shibata S, Matsubara A, Jinno S, Mizoguchi Y, Sasaki A, Ishibashi H (2004) Developmental switch from GABA to glycine release in single central synaptic terminals. Nat Neurosci 7:17–23.

Nerlich J, Rübsamen R, Milenkovic I (2017) Developmental shift of inhibitory transmitter content at a central auditory synapse. Front Cell Neurosci 11:1–19.

Noh J, Seal RP, Garver JA, Edwards RH, Kandler K (2010) Glutamate co-release at GABA/glycinergic synapses is crucial for the refinement of an inhibitory map. Nat Neurosci 13:232–238.

Oertel D, Bal R, Gardner SM, Smith PH, Joris PX (2000) Detection of synchrony in the activity of auditory nerve fibers by octopus cells of the mammalian cochlear nucleus. Proc Natl Acad Sci U S A 97:11773–11779.

Oertel D, Wu SH, Garb MW, Dizack C (1990) Morphology and physiology of cells in slice preparations of the posteroventral cochlear nucleus of mice. J Comp Neurol 295:136–154.

Oertel D, Young ED (2004) What’s a cerebellar circuit doing in the auditory system? Trends Neurosci 27:104–110.

Okada M, Onodera K, Van Renterghem C, Sieghart W, Takahashi T (2000) Functional correlation of GABA(A) receptor α subunits expression with the properties of IPSCs in the developing thalamus. J Neurosci 20:2202–2208.

Olsen RW, Sieghart W (2009) GABAA receptors: Subtypes provide diversity of function and pharmacology. Neuropharmacology 56:141–148.

Pasquale EB (2005) Eph receptor signalling casts a wide net on cell behaviour. Nat Rev Mol Cell Biol 6:462–475.

Pouzat C, Marty A (1998) Autaptic inhibitory currents recorded from interneurones in rat cerebellar slices. J Physiol 509:777–783.

Rice FL, Gomez C, Barstow C, Burnet A, Sands P (1985) AComparative analysis of the development of the primary somatosensory cortex: Interspecies similarities during barrel and laminar development. J Comp Neurol 236:477–495.

Rietzel HJ, Friauf E (1998) Neuron types in the rat lateral superior olive and developmental changes in the complexity of their dendritic arbors. J Comp Neurol 390:20–40.

Rivera C, Voipio J, Payne JA, Ruusuvuori E, Lahtinen H, Lamsa K, Pirvola U, Saarma M, Kaila K (1999) The K+/Cl- co-transporter KCC2 renders GABA hyperpolarizing during neuronal maturation. Nature 397:251–255.

Roberts MT, Seeman SC, Golding NL (2013) A mechanistic understanding of the role of feedforward inhibition in the mammalian sound localization circuitry. Neuron 78:923–935.

Salinas E, Sejnowski TJ (2000) Impact of correlated synaptic input on output firing rate and variability in simple neuronal models. J Neurosci 20:6193–6209.

Sanes DH, Geary WA, Wooten GF, Rubel EW (1987) Quantitative distribution of the glycine receptor in the auditory brain stem of the gerbil. J Neurosci 7:3793–3802.

Sanes DH, Rubel EW (1988) The ontogeny of inhibition and excitation in the gerbil lateral superior olive. J Neurosci 8:682–700.

Sanes DH, Siverls V (1991) Development and specificity of inhibitory terminal arborizations in the central nervous system. J Neurobiol 22:837–854.

Sanes DH, Takács C (1993) Activity-dependent Refinement of Inhibitory Connections. Eur J Neurosci 5:570–574.

Schlaggar BL, Fox K, O’Leary DDM (1993) Postsynaptic control of plasticity in developing somatosensory cortex. Nature 364:623–626.

Schwale C, Schumacher S, Bruehl C, Titz S, Schlicksupp A, Kokocinska M, Kirsch J, Draguhn A, Kuhse J (2016) KCC2 knockdown impairs glycinergic synapse maturation in cultured spinal cord neurons. Histochem Cell Biol 145:637–646.

Seidl AH, Rubel EW, Harris DM (2010) Mechanisms for adjusting interaural time differences to achieve binaural coincidence detection. J Neurosci 30:70–80.

Smith PH, Joris PX, Yin TCT (1993) Projections of physiologically characterized spherical bushy cell axons from the cochlear nucleus of the cat: Evidence for delay lines to the medial superior olive. J Comp Neurol 331:245–260.

Smith PH, Joris PX, Yin TCT (1998) Anatomy and physiology of principal cells of the medial nucleus of the trapezoid body (MNTB) of the cat. J Neurophysiol 79:3127–3142.

Sommer I, Lingenhöhl K, Friauf E (1993) Principal cells of the rat medial nucleus of the trapezoid body: an intracellular in vivo study of their physiology and morphology. Exp Brain Res 95:223–239.

Soto F, Bleckert A, Lewis R, Kang Y, Kerschensteiner D, Craig AM, Wong ROL (2011) Coordinated increase in inhibitory and excitatory synapses onto retinal ganglion cells during development. Neural Dev 6:31.

Spirou G, Berrebi AS (1997) Glycine Immunoreactivity in the Lateral Nucleus of the Trapezoid Body of the Cat. J Comp Neurol 488:473–488.

Spirou GA, Rager J, Manis PB (2005) Convergence of auditory-nerve fiber projections onto globular bushy cells. Neuroscience 136:843–863.

Takahashi T, Momiyama A, Hirai K, Hishinuma F, Akagi H (1992) Functional correlation of fetal and adult forms of glycine receptors with developmental changes in inhibitory synaptic receptor channels. Neuron 9:1155–1161.

Tamás G, Buhl EH, Somogyi P (1997) Massive autaptic self-innervation of GABAergic neurons in cat visual cortex. J Neurosci 17:6352–6364.

Tolbert LP, Morest DK, Yurgelun-Todd DA (1982) The neuronal architecture of the anteroventral cochlear nucleus of the cat in the region of the cochlear nerve root: Horseradish peroxidase labelling of identified cell types. Neuroscience 7:3031–3052.

Tollin DJ (2003) The lateral superior olive: A functional role in sound source localization.

Neuroscientist 9:127–143.

Travagli RA, Gillis RA, Rossiter CD, Vicini S (1991) Glutamate and GABA-mediated synaptic currents in neurons of the rat dorsal motor nucleus of the vagus. Am J Physiol 260.

Traynelis SF, Wollmuth LP, McBain CJ, Menniti FS, Vance KM, Ogden KK, Hansen KB, Yuan H, Myers SJ, Dingledine R (2010) Glutamate Receptor Ion Channels: Structure, Regulation, and Function. Pharmacol Rev 62:406–496.

Tritsch NX, Bergles DE (2010) Developmental regulation of spontaneous activity in the mammalian cochlea. J Neurosci 30:1539–1550.

Tschetter WW, Govindaiah G, Etherington IM, Guido W, Niell CM (2018) Refinement of spatial receptive fields in the developing mouse lateral geniculate nucleus is coordinated with excitatory and inhibitory remodeling. J Neurosci 38:4531–4542.

Tsuchitani C (1977) Functional organization of lateral cell groups of cat superior olivary complex. J Neurophysiol 40:296–318.

Van Den Pol AN, Gorcs T (1988) Glycine and glycine receptor immunoreactivity in brain and spinal cord. J Neurosci 8:472–492.

Van der Loos H, Woolsey TA (1973) Somatosensory Cortex : Structural Alterations following Early Injury to Sense Organs. Science (80-) 179:395–398.

Wassle H, Koulen P, Brandstatter JH, Fletcher EL, Becker C-M (1998) Glycine and GABA receptors in the mammalian retina. Vis Res 38:1411–1430.

Welker C, Woolsey TA (1974) Structure of layer IV in the somatosensory neocortex of the rat: Description and comparison with the mouse. J Comp Neurol 158:437–453.

Werthat F, Alexandrova O, Grothe B, Koch U (2008) Experience-dependent refinement of the inhibitory axons projecting to the medial superior olive. Dev Neurobiol 68:1454–1462.

Wever EG, Lawrence M, Bekesy G Von (1954) A Note on Recent Developments in Auditory Theory. PNAS 40:508–512.

Woods CI, Azeredo WJ (1999) Noradrenergic and serotonergic projections to the superior olive: Potential for modulation of olivocochlear neurons. Brain Res 836:9–18.

Woolsey TA, Van der Loos H (1970) The structural organization of layer IV in the somatosensory region (S I) of mouse cerebral cortex. The description of a cortical field composed of discrete cytoarchitectonic units. Brain Res 17:205–242.

Wu X, Fu Y, Knott G, Lu J, Cristo G Di, Josh Huang Z (2012) GABA signaling promotes synapse elimination and axon pruning in developing cortical inhibitory interneurons. J Neurosci 32:331–343.

Xie Z, Sastry BR (1991) Inhibition of protein kinase activity enhances long-term potentiation of hippocampal IPSPs. Neuroreport 2:389–392.

Yin TCT, Chan JCK (1990) Interaural time sensitivity in medial superior olive of cat. J Neurophysiol 64:465–488.

Young AB, Snyder SH (1973) Strychnine binding associated with glycine receptors of the central nervous system. Proc Natl Acad Sci U S A 70:2832–2836.

2 Chapter 2: Low-cost, Arduino-based blind single-cell electroporation in tissue

Title: Low-cost, Arduino-based blind single-cell electroporation in tissue

Authors: Ziqi (Hugo) Wang
Affiliations: School of Biomedical Engineering, McMaster University
Contact email: wangz74@mcmaster.ca

Abstract: Electroporation is commonly used to deliver exogenous substances to living cells, with Single Cell Electroporation (SCE) especially useful for targeting individual biological cells. While this method has broad usefulness, not all labs have access to the kind of equipment that can ensure success especially in tissues. Here, we describe a low-cost, open-source, Arduino-based SCE device that enables SCE in tissue and does not require access to sophisticated optics. The device operates in two modes: a search mode for positioning the electrode and an electroporation mode for delivering exogenous substances, and electroporation parameters can be easily modified by Arduino programming. We demonstrate how stimulus parameters can be modified to electroporate individual neurons in rodent tissue using dyes of different polarity. This adaptable, highly portable, device makes SCE accessible to teaching labs and other labs with small budgets.

Keywords: Single-cell electroporation, Arduino, Teaching

Specifications table

Hardware name	Arduino-based blind single-cell electroporator
Subject area	• Neuroscience • Biological Sciences (e.g. Microbiology and Biochemistry) • Educational Tools and Open Source Alternatives to Existing Infrastructure
Closest commercial analog	Axoporator 800A (Molecular Devices)
Hardware type	• Biological sample handling and preparation
Open Source License	CC-BT-SA 4.0
Cost of Hardware	104.285
Source File Repository	*https://doi.org/10.17605/OSF.IO/BWJNY*

2.1 Hardware in context

Electroporation has been widely used to deliver a variety of exogenous substances – such as dyes, nucleic acids, proteins, peptides, and pharmacological agents (Mir et al., 1988) – into living cells. To electroporate, the researcher supplies the exogenous substance externally, and then applies a local electric field that transiently disrupts the cell membrane. When performed properly, membrane pore formation lasts long enough to allow transfer of the substance but not so long as to cause lasting damage. Although bulk electroporation is useful for delivering substances to cell populations (Kinosita and Tsong, 1977), researchers often need to target substances more precisely to individual cells. Single-cell electroporation (SCE), which provides a localized electrical field of a few Volts to individual cells (for review, see (Olofsson et al., 2003)), answers the need for higher resolution delivery. Successful SCE requires that the electrode tip be precisely positioned with respect to the cell membrane during the application of the electric field. Electrode tip position is easily monitored using appropriate microscope optics when working with cultured cells. However, monitoring electrode tip position is more complicated when working with tissue, where infrared optics and dipping objectives are of limited use, as well as for labs without access to these optics. In the last few decades, SCE devices that use electrical feedback to monitor the position of the electrode tip relative to the cell membrane have been implemented for use with cultured cells, in *ex vivo* living tissue, and *in vivo*, (Lundqvist et al., 1998; Haas et al., 2001).

More recently, a number of commercially available options (e.g., the Molecular Devices Axoporator 800A, Grass Telefactor) have become available for SCE (Bestman et al., 2006; Judkewitz et al., 2009; Pagès et al., 2015; Schohl et al., 2020). These commercial solutions, however, may not be accessible to labs with limited budgets or space, and in particular to teaching labs. Although some implementations of blind SCE (SCE without visual guidance) have been described for dissociated cells (Dong et al., 2020; Zhang et al., 2020), these devices have limited usefulness in tissue. Additionally, although bulk electroporation can be used to drive SCE through stochastic expression of Cre-recombinase, this method, too, relies on genetics tools unavailable to all labs. We were motivated to create a blind SCE device that would be highly portable, adaptable for use in tissue, and that furthermore could be easily implemented by biology students.

Here, we have altered the circuit described by Rae and Levis in their modified patch-clamp design (Rae and Levis, 2002), implementing a unit that monitors resistance to target single cells in the absence of visual guidance. We replaced external stimulators with an Arduino and transistors to create a space-saving and highly portable device. The implementation is low-cost, open-source, adaptive, portable, and applicable for multiple biological preparations.

2.2 Hardware description.

The principle is based on a method used in patch-clamp electrophysiology, a technique that crucially relies upon formation of a high-resistance (GΩ) seal between the biological membrane and the electrode glass to allow low-noise access to the cell interior [17]. Success in obtaining the GΩ seal is variable, and can be increased by bringing the electrode tip close to the cell membrane in appropriate orientation. Achieving the optimal electrode position is relatively straightforward using appropriate microscope and optics in cell culture systems. Due to light scattering by biological tissue in “living slice” or whole brain preparations, however, visual guidance is much less useful; hence, the recording electrode is often positioned using the "blind patch” method [18, 19]. In short, brief current or voltage steps are continuously applied in order to monitor resistance as the recording electrode is slowly advanced through the tissue. As the electrode tip nears a cell membrane, the ‘cleft resistance’ between electrode tip and cell membrane increases, and this change in cleft resistance is used to optimize electrode position. Figure 1A illustrates the principle of resistance monitoring for determining electrode position, where the voltage at the cell membrane (Vcm) is given by the voltage divider equation:

$V_{cm} = V_{In} \frac{R_{Cl}}{R_{Cl}+R_e}$ [1].

As cleft resistance (R_{Cl}) increases, the voltage at the cell membrane (V_{cm}) decreases. Because the voltages at the two inputs of the operational amplifier are equal, the output of the first operational amplifier A1 is:

$V_{O1} = IR_f + V_{in}$ [2],

where I is the current travelling through the electrode and R_f is the feedback resistor.

$I = \frac{V_{In}}{R_e+R_{Cl}}$ [3].

If the four resistors across the second operational amplifier are the same, the second operational amplifier A2 subtracts the stimulation (input) voltage V_{In} from the output of the first operational amplifier A1. The output at A2 is thus:

$V_{O2} = -IR_f$ [4],

Or, substituting from equation [3]:

$V_{O2} = -\frac{V_{In}}{R_e+R_{Cl}} R_f$ [5],

From equation [5], as R_{Cl} increases, V_{O2} decreases. We can monitor this decrease in V_{O2} with an oscilloscope to evaluate the distance between the tip of the electrode and the cell membrane.

Key components of this design ensure cost-effectiveness, portability, and flexibility:

- Arduino UNO
    - The UNO provides electrical stimulation
    - The programmable UNO allows users to design custom stimulation protocols
- Instrumentation amplifier AD620
    - The AD620 is used to calculate the voltage differences ($V_{input} – V_{electrode}$) that arise from changes in resistance as the electrode approaches a cell membrane
    - This instrumentation amplifier gives a high signal-to-noise ratio using only a single resistor for gain control
- Mini oscilloscope (JYE) mini oscilloscope
    - This device is used to monitor changes in resistance
    - It is small and inexpensive
- Batteries and transistors
    - These eliminate potential AC noise and provide greater portability

2.3 Design files

Design Files Summary

Design file name	File type	Open source license	Location of the file
SCE_update_bread.fzz	*Fritzing Design File*	CC-BT-SA 4.0	Available in OSF
SquareOut20210716.ino	Arduino file	CC-BT-SA 4.0	Available with the article

2.4 Bill of Materials

All costs are in Canadian dollars (CAD).

Designator	Component	Number	Cost per unit - currency	Total cost - currency	Source of materials	Material type
To make it easy to tell which item in the Bill of Materials corresponds to which component in your design file(s), use matching designators in both places, or otherwise explain the correspondence.	Arduino Uno	1	23	23	Arduino https://www.arduino.cc/	*Electronics*
	Instrumentation Amplifier	1	16.97	16.97	Digikey https://www.digikey.ca/en/products/detail/analog-devices-inc/AD620ANZ/750967	*Electronics*

	Solderless Breadboard	1	22.6	22.6	Digikey https://www.digikey.ca/en/products/detail/schmartboard-inc/201-0016-31/9559349	*Electronics*
	Jumper wire	1 kit	5.52	5.52	Digikey https://www.digikey.ca/en/products/detail/global-specialties/WK-3/5231342	
	BJT (PNP)	2	0.26	0.52	Digikey https://www.digikey.ca/en/products/detail/micro-commercial-co/2N4403-AP/950594	*Electronics*
	BJT (NPN)	2	0.26	0.52	Digikey https://www.digikey.ca/en/products/detail/micro-commercial-co/2N4401-AP/950593	*Electronics*
	LED (RED)	1	0.2	0.2	Digikey	*Electronics*

					https://www.digikey.ca/en/products/detail/cree-inc/C5SMF-RJF-CT0W0BB2/6138570	
	LED (GREEN)	1	0.48	0.48	Digikey https://www.digikey.ca/en/products/detail/sunled/XLVG11D/13559314	*Electronics*
	Resistor 10 MΩ	1	0.00475	0.00475	Digikey or local electronic stores	*Electronics*
	Resistor 77 KΩ	2	0.00475	0.0095	Digikey or local electronic stores	*Electronics*
	Resistor 10 KΩ	4	0.00475	0.019	Digikey or local electronic stores	*Electronics*
	Resistor 5.7 KΩ	3	0.00475	0.01425	Digikey or local electronic stores	*Electronics*
	Resistor 4.7 KΩ	2	0.00475	0.0095	Digikey or local electronic stores	*Electronics*
	Resistor 2.2 KΩ	3	0.00475	0.01425	Digikey or local electronic stores	*Electronics*

	Resistor 1 KΩ	3	0.00475	0.01425	Digikey or local electronic stores	*Electronics*
	Resistor 220 Ω	2	0.00475	0.0095	Digikey or local electronic stores	*Electronics*
	9V Battery	2	1.58	3.16	Corner store	*Electronics*
	Push Button	1	0.81	0.81	Digikey https://www.digikey.ca/en/products/detail/nidec-copal-electronics/TR1-01/5125294	*Electronics*
	Single pole Single Throw Switch	1	0.81	0.81	Digikey https://www.digikey.ca/en/products/detail/e-switch/RA11131121/2720267	*Electronics*
	Single pole Double Throw Switch	5	0.52	2.6	Digikey https://www.digikey.ca/en/products/detail/te-connectivity-alcoswitch-switches/1825232-1/4021554	*Electronics*
	DSO 138 Oscilloscope	1	27	27	JYE tech	*Electronics*

					https://jyetech.com/dso-138-oscilloscope-diy-kit/	

*[*Jumper wires can be obtained from used cell phone charger, printer, ethernet, and telephone cables. The assembled oscilloscope is also available at a slightly higher price at JYE Tech.*]*

2.5 Build Instructions

Here we provide step-by-step instructions, together with photos, in the hopes that individuals with little experience building such devices (including biology students) will feel enabled to build and use this device.

The electronic parts should be placed on the breadboard as shown in Figure 2, checking orientations of BJT and LED carefully.

A) ***Power*** (Fig. 2A)
  a. The device is powered by two 9V batteries in series. The orange wire shown in the graph is required to connect the two batteries.
  b. Attach battery holders to breadboard.
  c. Positive and negative power supply, and ground, are specified by yellow arrowhead.

B) ***Differential amplifier module*** to measure/amplify change in cleft resistance (Fig. 2B)
  a. NOTE: The bubble indicated with the red circle specifies the correct orientation of AD620. The top left pin to the bubble is pin 1 of AD620. Pins 2 – 8 follow Pin 1 counter-clockwise around the device.
  b. Attach resistor R7 (5.7 kΩ) across pin 1 and pin 8 of AD620.
  c. Connect Pin 4 to the negative power supply.
  d. Connect Pin 5 to ground.
  e. Connect Pin 7 to the positive power supply.
  f. Place feedback resistor across Pins 2 and 4.
  g. Pin 6 (output) will be connected to an oscilloscope.

C) ***Negative search pulse module*** (Fig. 2C)
  a. The search pulse provided by the Arduino feeds to the base of the transistor Q1 through a voltage divider (R1 and R2) with respect to the negative power supply.
  b. Attach R1 to the base of Q1.
  c. Place R2 across the base of Q1 and the negative power supply.
  d. Place R3 across the collector of Q1 and the negative power supply.
  e. Connect the emitter of Q1 to the ground.

D) ***Voltage divider module*** (Fig. 2D)
  a. Arduino provides a square wave with an amplitude of 5V, which can cause undesired labels during searching. The voltage divider is used to reduce the search pulse amplitude by at least 10-fold.
  b. Resistor R5 should be at least 10 times resistor R4.
  c. Place R5 near the differential amplifier module.
  d. Place R4 across R5 and the ground.
  e. Connect the voltage divider to pin 2 of AD620.

E) ***Positive stimulation module*** (Fig. 2E)
  a. The output from Arduino will feed to the base of transistor Q2 through resistor R8.
  b. Attach R8 to the base of Q2.
  c. Place R9 across the collector of Q2 and the positive power supply.
  d. Place R10 across the collector of Q2 and the base of Q3.
  e. Place R11 across the collector of Q3 and the positive power supply.
  f. Ground the emitter of Q2 and Q3.
  g. The stimulation output is at the collector of Q3.

F) ***Negative stimulation module*** (Fig. 2F)
  a. The output of Arduino will feed to the base of the transistor Q4 through a voltage divider with respect to the negative power supply.
  b. Attach R17 to the base of Q4.
  c. Place R16 across the base of Q4 and the negative power supply.
  d. Place R18 across the collector of Q4 and the negative power supply.
  e. Ground the emitter of Q4.

G) ***Arduino interface module*** (Fig. 2G)
  a. Save the Arduino sketch below**; then connect the Arduino UNO to the computer and upload the sketch to the UNO to the computer to upload the program.
    i. Note that stimulation parameters for this sketch can be easily modified and re-uploaded to the Arduino UNO.
  b. Ground the digital and analog ground of the Arduino.
  c. Connect 5V power from Arduino to the breadboard.
  d. Place LED1 and R12 in series. (Caution: Ground R12 and attach the negative end of LED1 to R12.)
  e. Place LED2 and R13 in series. (Caution: Ground R13 and attach the negative end of LED3 to R12.)
  f. Attach A12 and A13 of Arduino to the breadboard.

H) ***Testing the device***
  a. Once the various modules have been assembled, as shown in Figure 2H, the circuit is ready for testing.
  b. The modules can be connected with wires and tested individually with an oscilloscope.
  c. Connect 5V port from Arduino to the breadboard (Fig. 3A).
  d. Connect 5V to the red LED (search function indicator).

    i. If LED does not light, check LED orientation.

e. Connect 5V to the green LED (stimulate function indicator), as shown in Figure 3B.
    i. If LED does not light, check LED orientation.
f. ***Check original search pulse*** generated by the Arduino (Fig. 3C)
    i. Connect the black (ground) probe of oscilloscope to ground
    ii. Connect red (signal) probe of oscilloscope to A13 (the port that generates the search pulse).
    iii. Connect red LED (search function LED) to A2.
    iv. A square pulse with amplitude 5V and the pre-programmed duration should appear on the oscilloscope.
        1. If the square pulse shows a duration different from the pre-programmed duration, load the sketch to the Arduino again.
g. ***Check positive search pulse*** after the signal passing through the voltage divider module (Fig. 3D).
    i. Connect A13 from Arduino to breadboard.
    ii. Connect A13 pin from the breadboard (red arrow on breadboard) to the voltage divider (yellow rectangle).
    iii. Connect oscilloscope probe to output of the voltage divider.
    iv. The amplitude of the square wave shown on the oscilloscope should be approximately $\frac{5V}{R_4+R_5} \times R_4$.
h. ***Check negative search pulse, Step 1*** – invert original pulse (Fig. 3E)
    i. Connect A13 to R1.
    ii. Connect signal probe of oscilloscope to the collector of Q1.
    iii. The oscilloscope should show a negative square pulse with amplitude 9V.
i. ***Check negative search pulse, Step 2*** – scale to lower amplitude (Fig. 3F)
    i. Connect the collector of Q1 to R5.
    ii. Connect the output of the voltage divider to Pin 2 of the AD620.
    iii. Connect signal probe of oscilloscope to Pin 2 of the AD620.
    iv. The amplitude of the negative square wave at the oscilloscope should be approximately $\frac{9V}{R_4+R_5} \times R_4$.
j. ***Check original stimulation pulse*** generated by Arduino (Fig. 3G).
    i. Connect A12 to the breadboard.
    ii. Connect the signal probe of the oscilloscope to A12.
    iii. Square pulses with amplitude 5V and pre-programmed period and duty cycle should appear on the oscilloscope.
k. ***Check positive stimulation pulse, Step 1*** – flip and amplify original pulse (Fig. 3H)
    i. Connect A12 to R8.
    ii. Connect the signal probe to the collector of the transistor Q2.
    iii. The oscilloscope should display square pulses with amplitude 9V and a reciprocal duty cycle.

l. ***Check positive stimulation pulse, Step 2*** – restore preset duty cycle (Fig. 3I)
    i. Connect the signal probe to the collector of the transistor Q3.
    ii. The oscilloscope should display square pulses with amplitude 9V and the preset duty cycle.

m. ***Check negative stimulation pulse*** (Fig. 3J)
    i. Connect A12 to R17
    ii. Connect signal probe to the collector of the transistor Q4.
    iii. The oscilloscope should display negative square pulses with amplitude 9V and the preset duty cycle.

I) **Arduino Sketch

```
volatile int CellF = 0; // Search for cell
volatile int Elec = 0; // Electroporate

void interruptFunction1 () {

if (digitalRead(2) == HIGH){
   CellF = 1; // if pin D2 reads HIGH, start looking for cells
 }
  else if (digitalRead(2) == LOW){
    CellF = 0; // if pin D2 reads LOW, Stop looking for cells
 }
}

void interruptFunction2 () {
 if (digitalRead(3) == HIGH){
   Elec = 1; // if pin D3 reads HIGH, start electroporation
 }


  else if (digitalRead(3) == LOW){

    Elec = 0; // if pin D3 reads LOW, Stop electroporation
 }
}

void setup() {

attachInterrupt(0,interruptFunction1, CHANGE);// interrupt 0 for pin 2
attachInterrupt(1,interruptFunction2, CHANGE);// interrupt 1 for pin 3
pinMode(13,OUTPUT); // searching pulse at pin 13
pinMode(12,OUTPUT); // Electroporation pulse at pin 12
 Serial.begin( 9600);
```

```
}

void loop() {


if(CellF) {
 digitalWrite(13,HIGH);
delay(5); // duration in ms of 5V
digitalWrite(13,LOW);
delay(1000); // duration in ms of 0V

}

if(Elec){

//First pulse
 digitalWrite(12,HIGH);
 delay(5);
 digitalWrite(12,LOW);
 delay(10);
//Second pulse
 digitalWrite(12,HIGH);
 delay(5);
 digitalWrite(12,LOW);
 delay(1000);
// Similar to the previous wave function, duration in ms for High and Low. Note,
these numbers can be changed for different electroporation parameters.
   }
}
```

2.6 Operation Instructions

Ancillary equipment, supplies, and reagents
This device can be used with a number of different biological preparations, each of which will have its own specific requirements. The following notes are common to all:

A) Electrodes
    a. Electrode glass
        Although the precise composition and the physical parameters of the capillary glass from which the electrodes are pulled can be critical for electrophysiology, they are less crucial here. Note that a) inclusion of a filament in the capillary glass facilitates filling of the micropipette, and b)

capacitive charge build up is reduced with thicker wall glass, resulting in less noisy pulses that are easier to read on the oscilloscope.

b. Electrode resistance
Although electrodes used for SCE typically have resistances in the range 10-20MΩ, this value can be modified to optimize for tissue and cell type. The resistance is changed by modifying physical tip parameters determined by the pipette puller.

c. Electrode use
Unless the tip clogs (detectable as an increase in electrode resistance), 3-4 cells can be electroporated with a single electrode.

d. Electrode holder
The micropipette must be held securely in a microdrive or micromanipulator, which can be done simply with a piece of tape. It is however useful to apply a small amount of pressure to the back of the electrode in order to reduce the incidence of tip clogging and consequent false positive changes in resistance. If an electrode holder with air inlet is unavailable, a reasonable facsimile can be fashioned from narrow bore Tygon tubing and a syringe.

e. Electrode fabrication
As micropipettes for SCE can be pulled in advance, electrodes may be purchased in bulk. Otherwise, they may be pulled on any standard pipette puller. Consult manufacturer’s advice for tips on achieving the desired tip geometry.

B) Ag/AgCl wire
A silver wire, or a chlorided (Ag/AgCl) silver wire, electrically connects the circuit to the electrode. To make the connection, the wire is threaded into the electrode until it makes contact with the liquid filling the tip of the electrode. Silver wire can be chlorided inexpensively by dipping into chloride bleach for 10 minutes.

C) Ground wire
Regardless of the experiment preparation, a ground wire is required to complete the circuit between the biological preparation and the device. We used an Ag/AgCl wire here.

D) Manipulator/Microdriver
A simple micromanipulator is useful for positioning and then stably holding the electrode/electrode holder. For fine control when advancing/retracting the electrode, a microdrive is recommended.

E) Optical magnification
For initial electrode placement within the area of interest, it is helpful to be able to visualize the general area with a loupe or a stereo microscope.

F) Note: As this device is generally used with living cells and/or tissues, the user is responsible for following ethical, approved procedures for obtaining and working with biological specimens.

The original SCE circuit of Rae and Levis was designed for negatively charged substances. The device described here includes modules to optimize delivery of either positively or negatively charged substances. Figure 1B illustrates SCE for positively charged substances. Toggling the switches S3 – S7 allows us to deliver negatively charged material.

Operationally, the device functions in two modes, 1) Search Mode: used to position the electrode with respect to a cell membrane, and 2) Electroporation Mode: used to provide a localized electric field once electrode position has been established. To indicate whether the device is in Search or Electroporation Mode, different colors of LEDs are used (the LEDs require resistors R12 and R13 to limit current through the LEDs). Toggle switch S1 toggles between the two operation modes.

Search Mode: When S1 is toggled to the right in the circuit diagram, the electrode is connected to the resistor *R6,* and the whole circuit operates in Search Mode. In Search Mode, when switch S2 is closed, the digital input D2 takes a 5V DC input (digital high or HI). The Arduino sketch here acts such that a HI reading at D2 triggers an 'interrupt,' or event indicator, to activate digital Pin 13. When activated, digital Pin 13 continuously generates a search pulse with amplitude determined by the voltage divider with resistors R4 and R5 or R14 and R15. The frequency and the duty cycle (fraction of the square wave that is high in a period) are specified in the Arduino sketch. An oscilloscope is connected to J1 to monitor *V7*, the output of AD620. When the amplitude of *V7* drops by a user-determined fraction, we infer the electrode tip to be apposed to the cell membrane in a position appropriate for SCE. Empirically, a decrease of at least 20% is sufficient for this inference.

Electroporation Mode: When S2 is toggled to the left in the circuit diagram, the electrode is connected to the collector of transistor Q3 or Q4 (based on the polarity of the substance being electroporated), and the whole circuit operates in Electroporation Mode. During electroporation mode, when push button S3 is activated, the digital input D3 reads HI. In the included Arduino program, a reading of HI at D3 triggers an interrupt to activate digital Pin 12, which is programmed to generate electroporation pulses continuously.
For substances with positive polarity:

Setup Protocol:

1. Power the breadboard with two 9V batteries.
2. Load appropriate sketch onto Arduino UNO
3. Power the Arduino UNO with a PC or a USB plug.
4. Verify that switches S3 – S7 are in the position as shown in .
5. Toggle switch S1 to the right to enable Search Mode.

Search Protocol:

1. Close Switch S2 so that Arduino UNO generates searching pulses.

2. Adjust the display of the oscilloscope so that monitor the square pulses on display.
3. Apply positive pressure (~ 0.1 ml air) to the electrode, if desired, and slowly advance the electrode until the pulse amplitude drops below threshold.
   - Tip: advancing by a small step, waiting a few seconds, and advancing again, can be more effective than advancing continuously
   - A threshold drop of ≥20% is typically sufficient.
4. Retract and then advance the electrode again to test whether the voltage drop reoccurs.
5. If the voltage drop disappears, continue advancing the electrode or reposition the electrode in tissue and repeat the previous step until a likely cell is located.

Electroporation Protocol:

1. Open Switch S2 and toggle Switch S1 to the left to enable Electroporation Mode.
2. Push or hold Switch S3 to electroporate.

For substances with negative polarity:

Setup steps:

1. Toggle switches S3 – S7.
2. Repeat steps 2 – 4 for positively charged dye instruction.

Search steps:

3. Repeat steps 5 – 9 for positively charged dye instruction.

Electroporation step:

4. Follow step 10 for positively charged dye instruction.

Notes:

Search pulse shape: Various shapes can be used during the search phase. Because the various RC components of biological tissue can distort the search pulse, and successful electroporation relies on unambiguous amplitude changes as the electrode approaches a cell, we recommend a square-wave search pulse for use in tissue.

Electroporation parameters: The frequency and the duty cycle are programed in the Arduino and can easily be modified in the Arduino sketch. If push button S3 is held closed, a continuous stimulation square wave with user-defined frequency is delivered to the electrode. To avoid holding down push button S3 manually, a wire may be inserted across S3 (short circuit at S3). Alternatively, the user can depress S3 at different rates to manually change stimulation frequency.

Amplification: The Arduino provides a square wave with an amplitude of 5V. Empirically, an amplitude of 9V is sufficient to deliver various substances into the targeted cell. Transistors Q2 and Q3, and transistor Q4 amplify the amplitude of square wave to the voltage supplied at the collector of these transistors. The whole system is supplied with voltages of ±9V, and amplifying the square wave amplitude to 9V is coherent with the system supply voltage. If the 9V amplitude is found to be insufficient for a specific preparation (dependent on substance administered or on cell/tissue type), the user can cascade additional batteries at the collector of the transistor. As the stimulus amplitude, and local electric field increases, the probability rises of electroporating multiple cells. In this case, the user can add a voltage divider module at the collector of the transistor.

2.7 Validation and Characterization

We prepared acute living brainstem slices from young (under three week-old) rats (Alamilla and Gillespie, 2013) to test the SCE device with dyes of different polarities. This particular tissue is a good test for the device, as its relatively high optical density (Al-Juboori et al, 2013) makes visualization of the electrode tip especially challenging; moreover, rapid changes in tissue composition during this developmental period require modifications in SCE parameters for tissue from animals of different ages. In some cases, we transferred the living tissue slice to a widefield fluorescence microscope in order to crudely visualize filling of the cell body in real time.

2.7.1 Determining SCE parameters with Neurobiotin

We electroporated Neurobiotin-plus, a small dye commonly used to label nerve cells, to test a positively-charged substance. As Neurobiotin is not itself fluorescent, we used the high-affinity avidin-biotin interaction to bind a fluorophore (Alexa 488)-conjugated streptavidin to the neurobiotin for visualization (Fig. 4A). The parameters explored are summarized in Table I. We attempted to use single pulses to deliver Neurobiotin-plus. Success rates are shown in Figures 4B, C. With a lower resistance electrode (R_e = 10 MΩ), the success rate peaked at a square wave amplitude of 9V (Fig. 4B), but this amplitude also resulted in an undesirably high proportion of multiple cell electroporation (MCE) events. With higher resistance electrodes (R_e = 20 MΩ), we also found that success rates peaked at 9V, but this time without significant MCE events (Fig. 4C). Using as criterion for success a result in which exactly one cell was electroporated per attempt, the overall success rate for SCE with mono-pulse electroporation was < 30%.

Increasing the number of electroporation pulses increased the overall electroporation rate. Thus, lower resistance electrodes (R_e = 10MΩ) reliably produced electroporation events, many of which were MCE events (Fig. 4D). As with mono-pulse stimulation, using higher resistance (R_e = 20 MΩ) electrodes allowed us to minimize MCE events, whereas increasing the stimulus number increased the proportion of successful SCE events slightly (Fig. 4E). In these tests with Neurobiotin-plus, using R_e = 20 MΩ and a train of 5 pulses (20 msec, 9V square wave pulses, delivered at 1 Hz) brought the blind SCE success rate above one in three.

2.7.2 Single cell electroporation with Alexa 488 hydrazide

The negatively charged Alexa Fluor dyes are commonly used with biological cells. In this example, we show real-time fills at the cell body with Alexa Fluor^{TM} 488 hydrazide (Al 488). Stimulus protocol for Al 488 SCE is as follows:
Amplitude (Amp) = -9V, pulse duration (Dt) = 5 ms, number of pulses (NP) = 2, and Inter-Pulse-Interval (IPI) = 10 ms. This stimulus paired-pulses are delivered at 1 Hz. The only

varying parameter is the number of paired pulses. Figure 5A illustrated a labeled cell from the P11 tissue acquired through a Leica SP5 confocal microscope. Optimal SCE protocol and SCE success rates varied at different ages. Table II summarizes SCE outcome with the different numbers of paired-pulses for different age groups. The number of paired pulses (NT) was calculated based on the following criteria:

NT started at 1. We monitored the targeted cell in real-time. If we observed a bright fill of the cell with a single paired-pulse, we set NT = 1; otherwise, we increased NT with an increment of 2. If we observed a bright fill of the cell within 10 paired-pulses, we set NT Ɛ (1, 10]; otherwise, we increased NT with an increment of 5. If we observed a bright fill of the cell within 30 paired-pulses, we set NT Ɛ (10, 30]; otherwise, we increased NT with an increment of 10. If we observed a bright fill of the cell within 50 paired pulses, we set NT Ɛ (30, 50]; otherwise, we discarded the tissue slice. We have noticed that if we fail to fill a cell within 50 paired-pulses, additional paired-pulses do not increase the likelihood of success. In these cases, furthermore, we have found that the probability of filling another cell in the same tissue to be small. We suggest these observations may be symptomatic of poor slice health and that in these situations the dye may fill the cell and immediately leak out.

Table II$_{i}$ shows attempted SCE for different NT and different ages. Table II$_{ii}$ shows successful SCE with different NT at different ages. The success rates from table II$_{iii}$ are plotted in figure 5B. The decreased success rates at an older age were likely due to slice health. Success rates also decreased after 30 paired-pulses. The best SCE success rate was 33%.

2.8 Acknowledgements

I wish to acknowledge my supervisor, Deda Gillespie, for funding the project and editing the manuscript.

2.9 Declaration of interest

The authors declare that they have no known competing financial interests or personal relationships that could have appeared to influence the work reported in this paper.

2.10 Human and animal rights

All tissue collection methods for this study conformed to CCAC guidelines, and were previously approved by the McMaster University Animal Research Ethics Board

References

Alamilla J, Gillespie DC (2013) Maturation of Calcium-Dependent GABA, Glycine, and Glutamate Release in the Glycinergic MNTB-LSO Pathway. PLoS ONES ONE 8.

Bestman JE, Ewald RC, Chiu SL, Cline HT (2006) In vivo single-cell electroporation for transfer of DNA and macromolecules. Nat Protoc 1:1267–1272.

Dong Z, Jiao Y, Xie B, Hao Y, Wang P, Liu Y, Shi J, Chitrakar C, Black S, Wang YC, Lee LJ, Li M, Fan Y, Chang L (2020) On-chip multiplexed single-cell patterning and controllable intracellular delivery. Microsystems Nanoeng 6:1–11.

Haas K, Sin W, Javaherian A, Li Z, Cline HT (2001) Single-Cell Electroporation for Gene Transfer In Vivo. Neuron 29:583–591.

Judkewitz B, Rizzi M, Kitamura K, Häusser M (2009) Targeted single-cell electroporation of mammalian neurons in vivo. Nat Protoc 4:862–869.

Kinosita K, Tsong TY (1977) Hemolysis of human erythrocytes by a transient electric field. Proc Natl Acad Sci U S A 74:1923–1927.

Lundqvist J a, Sahlin F, Aberg M a, Strömberg a, Eriksson PS, Orwar O, Uesaka N, Nishiwaki M, Yamamoto N (1998) Altering the biochemical state of individual cultured cells and organelles with ultramicroelectrodes. Proc Natl Acad Sci U S A 95:10356–10360.

Mir LM, Banoun H, Paoletti C (1988) Introduction of definite amounts of nonpermeant molecules into living cells after electropermeabilization: Direct access to the cytosol. Exp Cell Res 175:15–25.

Olofsson J, Nolkrantz K, Ryttse F, Lambie BA, Weber SG, Orwar O (2003) Single-cell electroporation. Curr Opin Biotechnol 14:29–34.

Pagès S, Cane M, Randall J, Capello L, Holtmaat A (2015) Single cell electroporation for longitudinal imaging of synaptic structure and function in the adult mouse neocortex in vivo. Front Neuroanat 9:1–12.

Rae JL, Levis RA (2002) Single-cell electroporation. Pflugers Arch 443:664–670.

Schohl A, Chorghay Z, Ruthazer ES (2020) A Simple and Efficient Method for Visualizing Individual Cells in vivo by Cre-Mediated Single-Cell Labeling by Electroporation (CREMSCLE). Front Neural Circuits 14:1–11.

Zhang Z, Zheng T, Zhu R (2020) Single-cell individualized electroporation with real-time impedance monitoring using a microelectrode array chip. Microsystems Nanoeng 6.

2.11 Figures

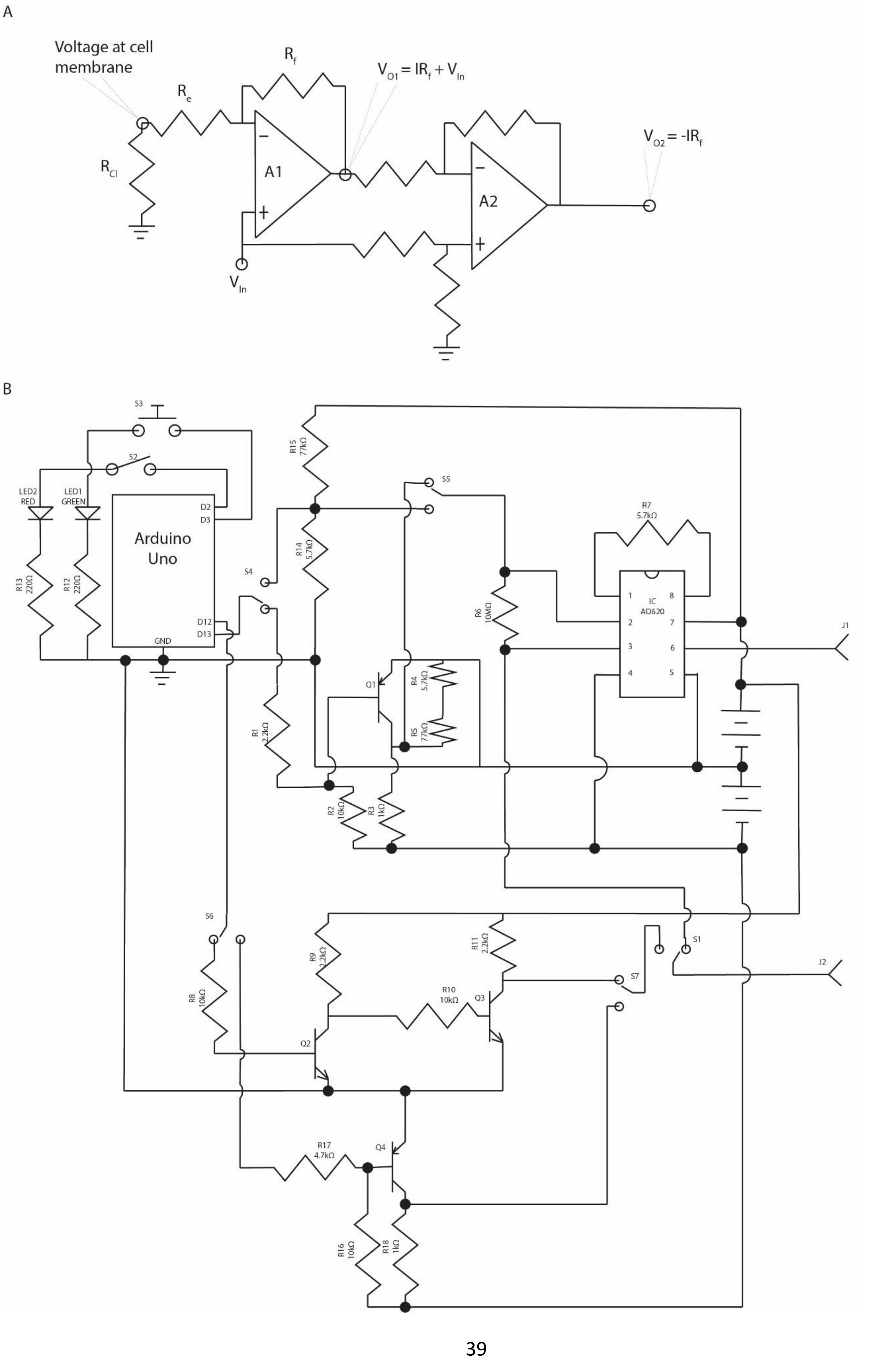
A
Voltage at cell membrane
R_e
R_f
R_Cl
A1
A2
V_O1 = IR_f + V_In
V_O2 = -IR_f
V_In
B
S3
S2
LED2 RED
LED1 GREEN
R13 220Ω
R12 220Ω
Arduino Uno
D2
D3
D12
D13
GND
S4
R15 77kΩ
R14 5.7kΩ
S5
R7 5.7kΩ
IC AD620
1
2
3
4
5
6
7
8
R6 10MΩ
J1
Q1
R4 5.7kΩ
R5 77kΩ
R1 2.2kΩ
R2 10kΩ
R3 1kΩ
S6
R8 10kΩ
R9 2.2kΩ
R11 2.2kΩ
R10 10kΩ
Q2
Q3
S7
S1
J2
R17 4.7kΩ
Q4
R16 10kΩ
R18 1kΩ

Figure 2-1

Figure 1. A. Circuit diagram in Rae and Levis approach (Rae and Levis, 2002) for modified patch clamp SCE device. R_f = feedback resistance, R_e = electrode resistance, R_{Cl} = cleft resistance, V_{In} = applied voltage stimulated to the electrode, V_{O1} = output voltage of operational amplifier A1, V_{O2} = output voltage of operational amplifier A2. B. Circuit of Arduino based blind SCE device. IC is the instrumentation amplifier AD620. R7 is the gain resistor of AD620. R6 is the feedback resistor. Q1 and Q4 are PNP BJTs, whereas Q2 and Q3 are NPN BJTs. S3 is a push-button switch, whereas S2 is a single pole single throw switch. All other switches are single pole double throw switches. Junction 1 (J1) connects to an oscilloscope. Junction 2 (J2) connects to an electrode. S1 toggles between two operation modes. S4 – S7 toggles when different polar substances are delivered. Color for search and electroporation.

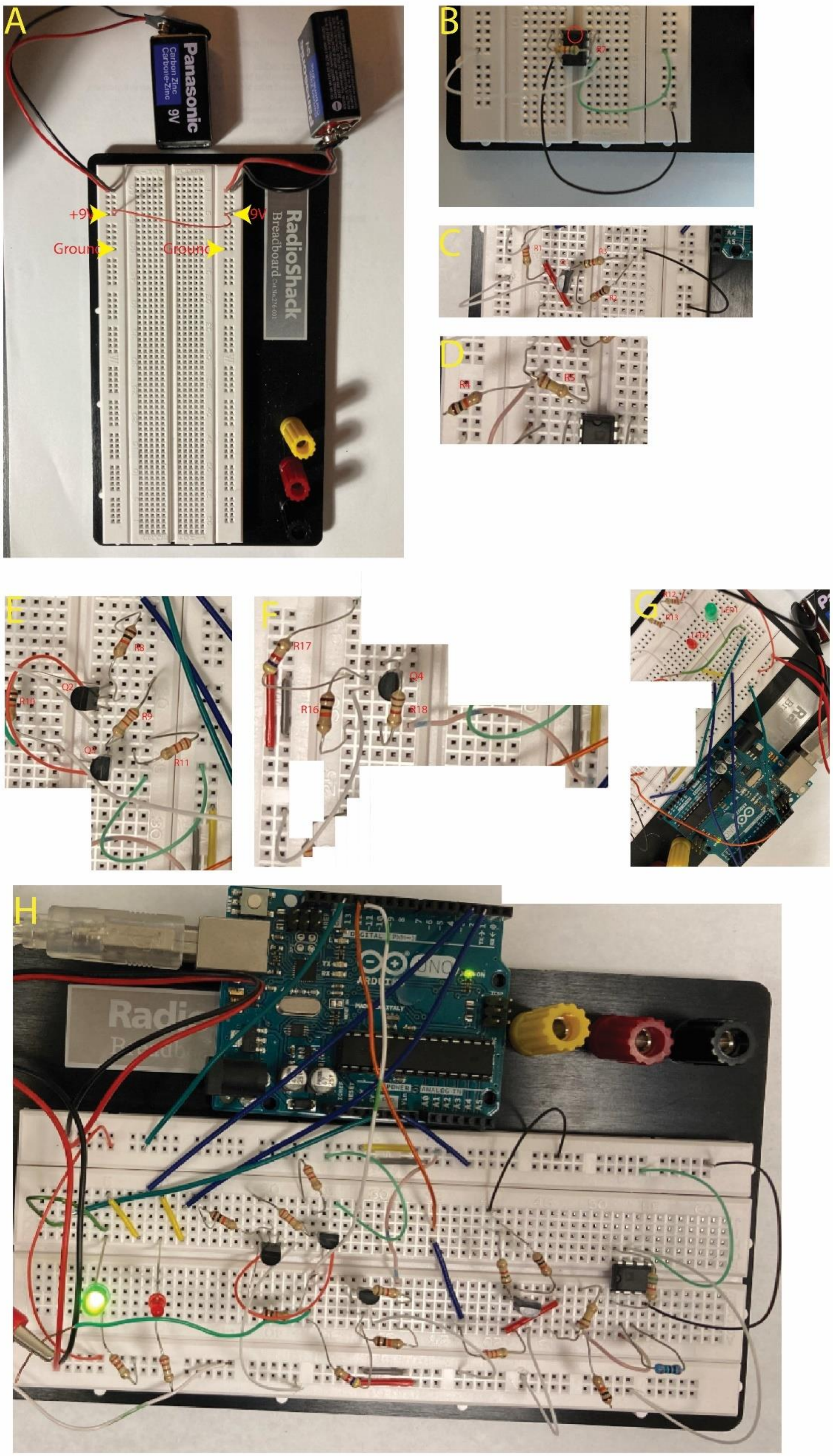
A
Panasonic
9V
+9V
-9V
Ground
Ground
RadioShack
Breadboard
B
C
R1
R3
R2
D
R4
R5
E
R8
Q2
R10
R9
Q3
R11
F
R17
Q4
R16
R18
G
R12
R13
LED1
LED2
H

Figure 2-2

Figure 2. Build instruction of SCE. (A) Build instruction for power supply. (B) Build instruction for differential amplifier module. (C) Build instruction for negative search pulse module. (D) Build instruction for voltage divider module. (E) Build instruction for positive stimulation module. (F) Build instruction for negative stimulation module. (G) Build instruction for Arduino interface module. (H) Overall circuit on the breadboard.

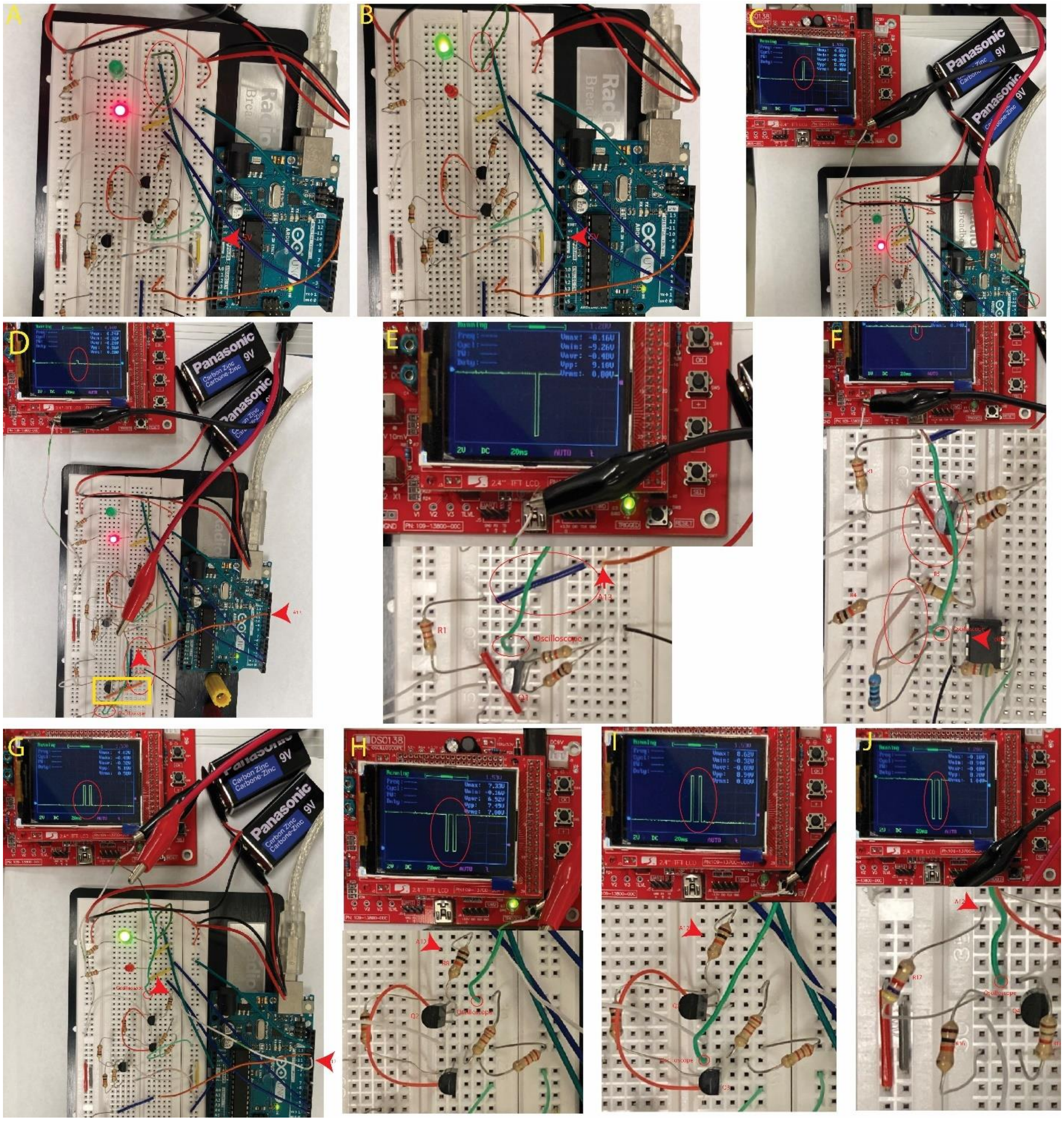

Figure 2-3

Figure 3. Instructions for testing SCE. (A) and (B) Test for the LEDs. (C) Test for the original search pulse. (D) Test for the positive search pulse. (E) and (F) Test for the negative search pulse. (G) Test for the original stimulation pulse. (H) and (I) Test for the positive stimulation pulse. (J) Test for the negative stimulation pulse.

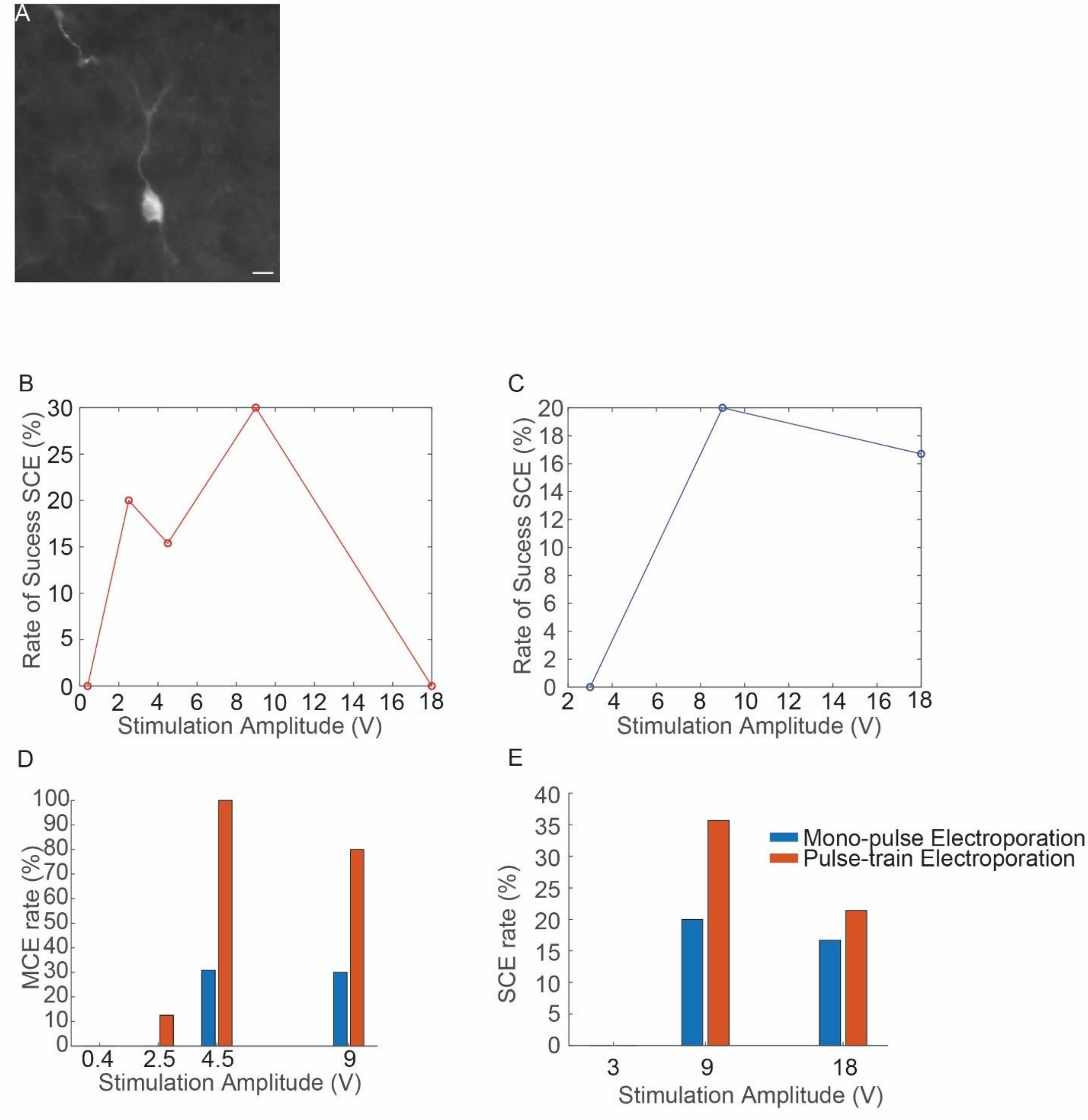

Figure 2-4

Figure 4. Blind SCE with neurobiotin-plus. (A) Example cell in superior olivary complex from P10 rat. Scale bar = 10 µm. (B – E) Changing stimulation parameters alters the SCE success rate. (B) Success rate for single-pulse electroporation as a function of the amplitude of the applied square wave, for Re = 10 MΩ (pulse duration 20 msec). (C) Success rate for single-pulse electroporation as a function of the amplitude of the applied square wave, for Re = 20 MΩ (pulse duration 20 msec). (D) with Re = 10 MΩ, increasing the number of pulses or stimulated voltage increased MCE rate. (E) with Re = 20 MΩ, increasing number of pulses increased the SCE success rate.

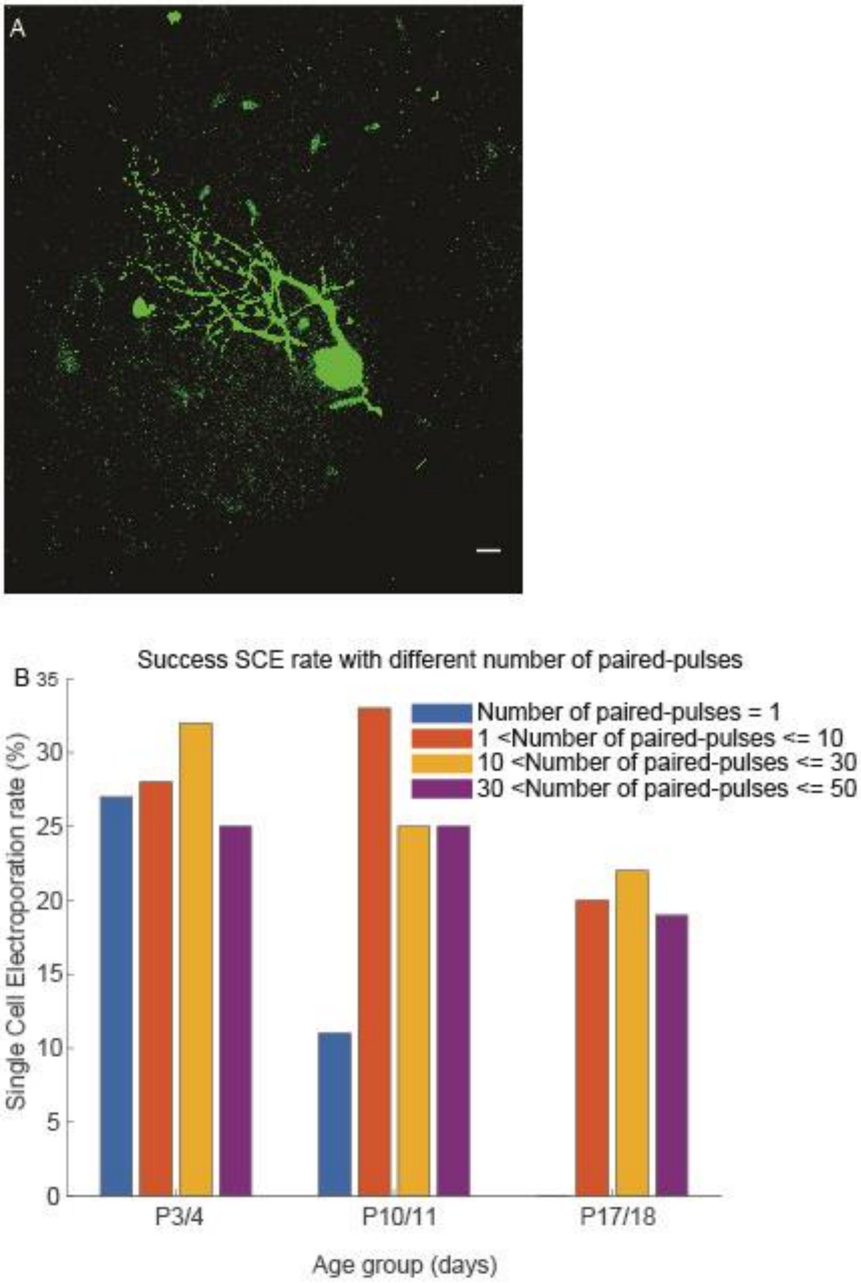

Figure 2-5

Figure 5. SCE protocol and success rate varied with respect to animal age. (A) A cell of LSO from P11 tissue filled with Alexa 488, shown in maximum Z projection. Image contrast is enhanced for illustration purposes. Scale bar = 10 µm. (B) SCE success rate against the number of pulse-pairs at different ages.

Table I Summary of SCE attempts with neurobiotin plus. We varied the pulse amplitude, the pulse duration, the inter-pulse interval, and the number of pulses.

Table 1

Amplitude (V)	Pulse Duration (ms)	Inter-Pulse Interval (ms)	Number of Pulses	Re (MΩ)	Total number of Electroporation	number of single Cell Electroporation	number of Multiple Cell Electroporation	number of No Cell Electroporation	Success Rate (%)	MCE rate (%)
18	20		1	10	7	0	4	3	0	57.14
9	20		1	10	10	3	3	4	30	30
9	20	1000	5	10	5	0	4	1	0	80
4.5	20		1	10	13	2	4	7	15.38	30.77
4.5	20		5	10	6	0	6	0	0	100
2.5	20		1	10	9	3	0	6	33.33	0
2.5	20	1000	10	10	8	0	1	7	0	12.5
2.5	20	1000	5	10	7	1	0	6	14.29	0
2.5	20	10	2	10	13	4	0	9	30.77	0
2.5	5	10	2	10	9	2	0	7	22.22	0
2.5	5	10	5	10	10	0	1	9	0	10
0.4	20		1	10	3	0	0	3	0	0
0.4	20	1000	10	10	5	0	0	5	0	0
18	5	10	5	20	5	0	0	5	0	0
18	5	10	2	20	23	7	0	16	30.43	0
18	20		1	20	12	2	0	10	16.67	0
18	20	10	2	20	14	3	0	11	21.43	0

9	20		1	20	15	3	0	12	20	0
9	20	1000	5	20	14	5	0	9	35.71	0
3	20		1	20	7	0	0	7	0	0
3	20	10	5	20	6	0	0	6	0	0

Table II Summary of SCE outcomes with Alexa 488.
Success rates (%) for different numbers of pulse-pairs in very young and juvenile rat tissue for Alexa 488. Electrodes had resistance 20 MΩ, and stimulation protocol varied in the number of pulse-pairs. Numbers under each age group indicate the success rates (%) for each protocol. Numbers in parenthesis indicate number of attempts for each condition.

Table 2

SCE % Success Rate				
	Animal Age # of paired-pulses	P3/4	P10/11	P17/18
	1	27 (11)	11 (9)	0 (1)
	2 - 10	28 (25)	33 (18)	20 (5)
	11 - 30	32 (22)	25 (32)	22 (23)
	31 - 50	25 (8)	25 (8)	19 (21)

3 Chapter 3: 3D Image Processing for Fluorescent Microscopy Images: Neuronal Reconstruction and Synapse Segmentation

3.1 Abstract

Understanding function in the nervous system is advanced by understanding structure, as the function of an individual neuron depends critically on that neuron's morphology and on the geometry of its inputs. Algorithms for reconstructing neurons in 3 dimensions have advanced rapidly over the last few decades, and existing programs have a range of strengths and weaknesses. In particular, the noisy nature of many biological images imposes an extra obstacle for reconstruction programs. A program that provides both robust reconstruction for studies of neuronal morphology and robust segmentation of subcellular structures, including most importantly the synapse, is still critically needed. The problem of synapse identification has been particularly challenging, as the successful algorithm must segment synaptic label from a noisy image while achieving reasonable proportions of false positives and false negatives. Furthermore, the size of many synapses, which is close to the diffraction limit of light microscopy, imposes additional challenges when segmenting overlapping or directly apposed signal from nearby synapses. In this chapter, I report on my evaluation of all available software packages for 3D neuronal reconstruction, and I describe our new, efficient algorithm for synapse segmentation. I then combine these approaches to provide a new and improved workflow for identifying synaptic partners in a double-labelled fluorescence micrograph.

3.2 Introduction

Over a century ago, Santiago Ramón y Cajal demonstrated the striking diversity of neuronal morphology. For all neurons, cellular morphology and the spatial distribution of synaptic inputs critically shape signal integration and the neuronal response to particular stimuli (Rall, 1959; Rall et al., 1967). With the advance of techniques in image acquisition and analysis, over the past few decades, neuroscientists been able to use stacks of two-dimensional optical microscopy images acquired at successive depths throughout neural tissue or cells and to reconstruct single neurons in three dimensions to reveal details of neuronal morphology. The process of reconstruction always requires converting the large image file to a more computationally compact format that represents the neuronal morphology with a set of points in a 3D coordinate space, consisting of information for local radius and connectivity to adjacent points, which is easier to analyze, store, and share (Ascoli, 2006). This labour-intensive process of neuronal reconstruction is extremely time consuming and can be prone to error.

In 2009, in an attempt to more quickly overcome these obstacles, several institutes participated in a competition, the DIADEM (DIgital reconstruction of Axonal and DEndritic Morphology) challenge, to boost the development of 3D neuronal reconstruction (Ascoli et al., 2009). The DIADEM challenge motivated the development of various algorithms aiming to reconstruct neurons in 3D in a fully automated manner. To date, a number of commercial concerns and academic labs have developed reconstruction software packages and can claim successful solutions to the problem of automated 3D reconstruction. In practice, however, neuroscientists often still use manual or semi-manual approaches for neural reconstruction neurons for a number of reasons related primarily to a lack of generalizability (Brown et al., 2011). For example, automated reconstruction nearly always fails to solve neurons that are incompletely labeled. Whereas human operators can use well-trained gestalt perception to trace along a dendrite even where the labeling contains gaps, automated reconstruction typically identifies the broken dendrite as two individual pieces. In cases where dendrites appear with punctate morphology – a relatively common artifact referred to as “beads on a string” – human operators can carefully align each punctum by checking back and forth along the Z axis. Automated reconstruction programs cannot perform this task at all. In addition, when two branches overlap, whereas human operators can usually separate the two branches, automated reconstruction often merges the branches into a single branch. Signal-to-noise ratios (SNRs) present an ever-present challenge for biological imaging, as labeling techniques that yield high SNRs for certain types of cells, tissues, or ages, or for labs with specific combinations of expertise, equipment, and reagents may simply not work in other situations. Unsurprisingly, reduced SNR has a pronounced effect on automated reconstruction. Finally, although some excellent machine learning algorithms now exist, these reduce the size of the dataset by the number of images required to train the algorithm. This reduction in dataset size can be a grave problem for situations in which the data are hard-fought and/or where developmentally- or experimentally-induced changes in morphology are so significant as to require new training sessions.

For studies of structure-function relationships at the cellular level, a second analytical problem that often accompanies the problem of neuronal problem is that of identifying, localizing, and quantifying synapses. For the first step of identifying synapses from a noisy biological image, the segmentation procedure is commonly performed on stacks of 2D optical microscopy images with fluorescently labelled synaptic proteins. As with studies of 3D cellular morphology, a fully automated approach for 3D synapse segmentation is critically required, and a number of classical 3D image segmentation techniques have been implemented to detect synapses. Global thresholding that automatically assigns a threshold value to the entire image (Ridler and Calvard, 1978) is useful if the synapses show homogeneous intensity values against a high contrast uniform background, a situation that occurs often for neurons raised in culture. This technique often fails, however, when applied to neural tissue, where synaptic label tends to exhibit a larger range of intensities, and where the presence of labeled tissue gives a relatively noisy background. Edge-based segmentation has also been implemented for automated 3D segmentation (Bomans et al., 1990). This approach is useful for objects with ‘good’ boundaries, i.e., those where intensity values change sharply across synapse edges. However, the intensity changes at synapse edges are often gradual and inhomogeneous, and do not always provide optimal high-contrast changes. Region-based segmentation is another classical algorithm adopted for 3D synapse segmentation. This approach exploits the spatial information by comparing the homogeneity within a small region or adjacent pixels (Bomans et al., 1990). Region-based segmentation is more computationally expensive, and always results in many voxels that remain unassigned to any region. A combination of global thresholding and region-based or edge-based segmentation can improve synapse segmentation results. However, this combined approach is heavily dependent on the initial thresholding value. If the initial threshold value is too high, on the one hand, segmentation always results in overly large putative synapses, where any number of nearby synapses may merge into an unrealistically large ('monster') synapse. If the initial threshold value is too low, on the other hand, background noise always produces false positive synapses. In neuronal tissue, synapses are commonly found in close proximity, a scenario that presents challenges for purely intensity-based algorithms. The watershed algorithm and cluster-based analysis that have been developed for 3D automated segmentation (Roysam *et al.*, 1994; Ancin *et al.*, 1996) are most effective for separating objects that just touch. However, these approaches also depend heavily on initial thresholding and tend to generate false positive signals from noisy background.

More recently, an iterative thresholding-based algorithm was developed and implemented specifically for segmentation of synapses from 3D images (Morgan et al., 2008). In this algorithm, the grayscale image is first thresholded multiple times with decreasing threshold values. The binary images from these thresholding steps are saved and summed to create a 3D map in which each voxel value is assigned the number of times the voxel passed threshold. The full width half maxima in this map define the volumes of the putative synapses. If multiple putative synapses merge at lower thresholds, they can be separated based on the peak locations. This algorithm prevents merging of multiple synapses into monster synapses and, with the addition of lower size constraints, minimizes false positive signals. Although this algorithm successfully solves the synapse segmentation problem, it is computationally expensive, and it has not been widely adopted. Still more recently, with advances in deep learning, convolutional neural networks have been implemented for 3D segmentation (Soltanian-Zadeh et al., 2019), and are seeing increasing use. This deep-learning approach, however, is not always feasible, first, in cases where similar datasets are unavailable for the intensive training required, and second, in cases where the lack of a ground truth requires interaction that could potentially bias segmentation decisions. Although leave-one-out cross validation and k-fold cross-validation have been shown to cope with the limited dataset, the low signal-to-noise ratio of the synaptic label gives rise to high variability in the dataset, further complicating the learning curve (Stone, 1977; Burman, 1989).

For the results reported in this chapter, I labeled individual neurons in brain tissue using a fluorescent dye, prepared the labeled tissue for imaging, acquired images at the confocal microscope, and used these digital images to test a variety of commercially available software and freeware for 3D neuronal reconstruction. Finding no viable software of any kind for the critical problem of synapse segmentation, I developed a new algorithm that uses a combination of iterative thresholding and watershed algorithm to segment labeled synapses in digital image stacks acquired at the confocal microscope.

3.3 Methods

3.3.1 Sample preparation and imaging

Tissue collection: All procedures were performed in accordance with Canadian Council on Animal Care Guidelines and were previously approved by the Animal Review Ethics Board of McMaster University. Sprague-Dawley rats born to animals bred on site or shipped pregnant (Charles River Laboratories, Wilmington, MA) were used throughout this study. Briefly, a neonatal rat pup was euthanized and the brain dissected. Tissue slices (300 µm) were prepared and allowed to recover for 30 minutes in a humidified interface chamber, then placed in artificial cerebrospinal fluid at an upright microscope equipped with water-immersion optics for neuronal labeling, or were placed into fixative for further processing as detailed below.

Neuronal labeling: Individual neurons were targeted with a custom single-cell electroporation device, and filled with Alexa Fluor™ 488 Hydrazide (ThermoFisher, A10436).

Tissue preparation: Acutely dissected slices were placed in fixative (4% paraformaldehyde) for 20 hours before being transferred to 30% sucrose in phosphate-buffered saline (PBS) for cryoprotection. The slices were re-sectioned at 50 µm and collected in PBS. Sections were blocked against non-specific staining by incubating for 24 hours in solution containing 5% normal serum, 2.5% bovine serum albumin (BSA), and 0.5% Triton-X in PBS. Sections were then incubated for 60 hours in solution containing 5% normal serum, 2.5% BSA, and primary antibodies raised against gephyrin, Vesicular Glutamate Transporter 1 (VGLUT1), and/or Vesicular Inhibitory Amino Acid Transporter (VIAAT) in PBS. Finally, sections were incubated for 24 hours in secondary antibodies diluted at 1:500 in 5% normal serum in PBS. Details of primary and secondary antibodies are listed in Table 2. Sections were washed in PBS before being mounted and coverslipped with high refractive index mounting medium (CFM-1, Citifluor Ltd.; RI = 1.515). Negative antibody controls were included in each staining run, and antibodies were monitored for changes in specificity across staining runs.

Image acquisition: Labeled neurons were imaged at the confocal microscope using an objective with numerical aperture (NA) 1.4 and Nyquist sampling, resulting in voxel sizes of 120 nm x 120 nm x 335nm. To minimize the chance for sample drift that might be associated with long acquisition sessions, all channels were imaged simultaneously.

3.4 Results

3.5 Evaluation of 3D reconstruction software packages

In this section, I describe the functionality of each software package I tested and comment on the performance and usability of each. A modern tool for assessing neuronal morphology makes use of the expression of fluorescent proteins under the control of promoters specific for the desired cell type(s). Powerful though this tool is, it cannot be applied to all situations. For example, in cases where appropriate promoters are not available to drive expression of the fluorescent protein in the desired cell type, or for the study of early developmental events where the fluorescent protein may not be expressed at sufficiently high levels in very young cells, researchers must use exogenous dyes. A potential disadvantage is that the labeling techniques for exogenous dyes can result in lower signal-to-noise ratios and present challenges for automated reconstruction. The single-cell electroporation labeling technique I used here provides a good test of the ability of these software packages to cope with lower signal-to noise ratios. Using the digital images acquired from electroporated cells, I tested the performance of automated 3D reconstruction and manual/semi-automated 3D reconstruction software packages. I list available software packages as of August 2019 for 3D reconstruction in Table 1. By 3D reconstruction I intend to mean not only the ability to create a 3D model of neurites (dendrites and axons) but also the ability to create a 3D model for somata and/or synapses. To distinguish between the two, I refer to neurite reconstruction as 'tracing' in Table 1.

Farsight (Wang et al., 2011), based on C++, was one of the winning solutions to the DIADEM challenge. This software incorporates all the functions including pre-processing, auto/semi-auto tracing, segmentation, 3D reconstruction and visualization. However, Farsight is no longer actively maintained and is currently unavailable for download. 3DMA-Neuron (Weaver et al., 2004) performs auto/semi-auto tracing, but is unable to segment objects or to perform 3D visualization. This software package was recently bought by Nihon Visual Science. I was unable to test these two software packages and therefore do not comment on their reconstruction performance.

Open source reconstruction software

1. **Vaa3D** (Peng et al., 2010) is a powerful open source software packages. It provides all the desired functions for 3D image processing, allows developers to contribute new plugins, and also allows users to write Matlab scripts for custom analyses. Vaa3D is actively maintained and is accompanied by intuitive tutorials. Developers answer technical questions promptly in the user forum. Tracing packages generate standard swc format files that can be used in multiple other software packages. Downsides were that auto tracing always generated false positive signals, and the semi-auto tracing was slow. The program tends to crash, especially when dealing with large datasets.
    a. **Pros**: User-friendly, versatility, universal file type and active technical support.
    b. **Cons**: Error-prone auto tracing, slow semiauto tracing, and crashing program.

2. **NeuTube** (Feng et al., 2015) is a C++-based tracing package. It is primarily use for neurite tracing and can be integrated with Vaa3D. NeuTube does not provide pre-processing or segmentation capability, and tracing relies on a high signal-to-noise ratio and homogeneous neuron label. Auto and semi-auto tracing is error-prone in the presence of a noisy background.
    a. **Pros**: User-friendly, universal file type, integrates with Vaa3D.
    b. **Cons**: Error-prone auto tracing and limited functionality.

3. **TrakEM2** (Cardona et al., 2012), a plugin for ImageJ, is primarily used for analyzing electron microscopy images. The “Trees” function extracts the skeletons of labeled neurons and exports a table containing node coordinates and edges. The traced image can be viewed only in this software package. The volume of the skeleton is error-prone in noisy images. Moreover, TrakEM2 provides manual tracing only.
    a. **Pros**: User-friendly, integrated in ImageJ.
    b. **Cons**: Only manual tracing, restricted file type, limited functionality, and poor reconstruction.

4. **NeuRA** (Broser et al., 2004) automatically traces neurites after soma segmentation. This program provides very basic image pre-processing, which sometimes does not enhance the image at all. The tracing approach always assumes that the geometric centre of the soma is the starting point of tracing. However, this placement of starting point biases the tracing results when the soma is not a perfect sphere and/or when soma size is large. The program performs poorly when the traced neuron has more than one primary dendrite. Auto tracing is also error-prone with noisy images.
    a. **Pros**: User-friendly and universal file type.
    b. **Cons**: Basic image processing function, biased starting point for tracing, error-prone auto tracing, poor tracing for neurons with multiple primary dendrites, and poor reconstruction.

5. **TREES toolbox** (Cuntz et al., 2010) is a Matlab toolbox designed for auto tracing. This toolbox exports the reconstructed neurite in swc file format, as well as in a format compatible with the NEURON simulation program. Auto tracing is error-prone with noisy images. There are a few bugs for manual editing, but this toolbox is actively maintained.
    a. **Pros**: User-friendly, universal file type, and compatible with NEURON.
    b. **Cons**: Limited function, error-prone auto tracing, buggy manual editing.

6. **ShuTu** (Jin et al., 2019), which is the Chinese name for dendrite, is a Python-based automated tracing software package. This program starts by auto-tracing the neuron and generating a swc file. Users can then interactively edit the auto-generated swc file. However, auto-tracing in a noisy image was quite error-prone, requiring more work to manually edit the reconstructed cell compared to semi-manual tracing.
    a. **Pros**: User-friendly and universal file type.
    b. **Cons**: Limited functionality, and extremely error-prone auto tracing.

7. **Neuromantic** (Myatt et al., 2012) is a software package for manual and semi-manual tracing. The tracing results are saved in swc format and can be viewed in 3D. However, during tracing process, the image is shown in 2D stacks with adjustable depth. The lack of a 3D view for the entire neurite impedes overall tracing performance.
    a. **Pros**: User-friendly and universal file type.
    b. **Cons**: Limited functionality, no auto tracing, and no 3D view during tracing.

8. **BisQue** (Kvilekval et al., 2009) is a cloud-based open source image analysis tool. This program is primarily used for 3D image visualization and analysis in Matlab or Python. The microtubule

tracking plugin of BisQue provides the possibility of neurite tracing. As this plugin was designed for tracing microtubules in time lapse images, tracing of neurites can be performed on only user-selected segment of one branch at a time. Although tracing speed is extremely slow, the cloud-based approach could be advantageous in certain circumstances.

   a. **Pros**: Versatility and cloud base.
   b. **Cons**: Extremely slow tracing process, not user friendly for tracing purpose, and poor reconstruction.

9. **ImageJ plugins for neurite tracing (including 9. Simple Neurite Tracer (SNT)** (Longair et al., 2011), **10. Tubular Geodesics** (Turetken et al., 2012), **11. NeuronJ** (Meijering et al., 2004), and **12. NeuriteTracer** (Pool et al., 2008) are all ImageJ plugins for neurite tracing. NeuriteTracer segments only the neurites and does not model them with connected vertices. NeuronJ allows semi-auto tracing and works only in 2 dimensions. Simple Neurite Tracer allows users to define two points on a branch and automatically find the path between these points. The path resembles the centreline of the neurite reasonably well, but does not determine the radius. Tubular Geodesics enhances the performance of SNT by modeling the computed neurite skeleton with tubular disks. For reconstruction that includes radius measurements, the optimal approach of all these is to combine SNT with Tubular Geodesics and to select user-defined points that are quite proximate to one another.
   a. **Pros**: User-friendly, universal file type, and integrated in ImageJ.
   b. **Cons**: Limited functionality, no auto tracing, and poor reconstruction.

Thus far, I have summarized open source software packages for 3D reconstruction. Vaa3D and its plugin together with several plugins for ImageJ provide possible solutions for auto and semi-auto neurite tracing. Together, these tools allow users to pre-process the images in order to enhance the tracing results, and they have fewer bugs than other software packages. Most of the auto-tracing software packages are error-prone, and Vaa3d and the ImageJ plugins are no exceptions. Semi-automatic tracing can deal with these errors, but because users must define points along branches and because pathfinding accuracy decreases inversely with distance between points, this solution is time consuming.

Commercial reconstruction software

13. **Imaris** (Oxford Instruments) is a commercial software package designed for intensive analysis of microscopy images. It provides basic image processing and analysis routines. It also allows users to write Matlab or Python functions to perform custom designed processing and analysis, as well as to invoke functions or plugins from ImageJ. Most notably, Imaris provides excellent 3D rendering. Although the auto-tracing is error prone, the interactive semi-auto tracing dynamically predicts the path along the branch following the user’s mouse movement without defining multiple points on the traced branch. The tracing results can be exported to Matlab-compatible files. Segmentation of the soma is based on thresholding, which often includes basal dendrites as parts of the soma. Manual editing of the segmented soma does not provide a smooth outline. Reconstruction does not provide optimal estimates of dendrite diameter.

   a. **Pros:** User-friendly, developer-friendly, versatile, training provided, viable tracing result, and fast semi-auto tracing.
   b. **Cons:** Poor soma segmentation, poor proximal dendrite reconstruction, and error-prone auto tracing.

14. **NeuroLucida** (MBF Bioscience) is a powerful commercial software package focused on neuron tracing and reconstruction and 3D brain mapping. It allows users to pre-process images and visualize neurons in 3D with excellent rendering technique. Users can trace neurons either live at the microscope using special hardware, or offline with image stacks. Auto tracing shows one of the most robust performances. Semi-auto tracing also allows dynamic prediction along a user-defined branch, following mouse movement without setting points along the branch. The program provides hundreds of morphometric analyses. The tracing results are saved in a proprietary format that can be viewed and analyzed only with NeuroLucida software. The segmentation of soma is smooth.
    a. **Pros:** User-friendly, versatile, training provided, fast and accurate semi-auto tracing, and excellent soma and dendritic reconstruction.
    b. **Cons:** Proprietary tracing result, poor synapse segmentation, and error-prone auto tracing.

15. **Aivia** (Drvision Technologies) is a recently developed commercial software package for microscopy image visualization and analysis. It incorporates machine learning technology to segment and classify neuronal objects. Auto-tracing primarily depends on thresholding of neurite. Whereas a high threshold level results in missing branches, a low threshold level results in tracing noise. The program allows users to calibrate the image with actual voxel size. However, semi-auto tracing does not work in a calibrated image at all. Tracing results can be saved as a Matlab-compatible format, which allows users to perform additional analyses with custom designed routines.
    a. **Pros:** User-friendly, versatile, training provided, viable tracing result, machine learning option for synapse segmentation.
    b. **Cons:** Semi-auto tracing is limited to uncalibrated image, error-prone auto tracing.

16. **Amira** (ThermoFisher) is a commercial software for image visualization and analysis with numerous purposes. It provides a unique block design for the image processing pipeline with decent 3D rendering. It allows users to implement different methods to segment objects. Very recently, the program also added a fiber tracing function that extracts the skeleton of the neurite. Interpolation of the neurite radius is based on the thresholded edge of the neurite, which is often not precise. The tracing results can be converted to swc format.
    a. **Pros:** Versatile, training provided, and universal file type.
    b. **Cons:** Limited functionality for neuronal tracing.

3.5.1 An efficient algorithm for 3D synapse segmentation

The iterative thresholding approach described by Morgan et al. (Morgan et al., 2008) represented an important advance in that it accurately discriminated synapses that were closely apposed; however, the algorithm is computationally expensive, as the requirement to loop through each iteration to evaluate whether to merge nearby signals quickly exhausts computational resources. Specifically, because in our 3D datasets we cannot represent neighboring voxels using linear indices, this algorithm requires a nested loop. To solve this problem, and to dramatically improve the algorithm's efficiency, we redesigned the algorithm to define putative synapse boundaries outside the nested loop and then to impose these boundaries on the segmented images. A flowchart summarizing this new synapse segmentation algorithm is shown in Figure 1.

The improved algorithm starts by iteratively thresholding the image at decreasing grey values. It then sums the binary images obtained at each threshold such that the value at each voxel represents the number of times that voxel surpassed threshold as threshold was iteratively reduced. Next, the algorithm detects local maxima from the summed image, a procedure that is more robust to noise than is detecting local maxima from a raw or median-filtered image. After identifying the local maxima, the algorithm performs two independent tasks:

A. It applies a watershed algorithm to the distance transform of the image containing the local maxima. This approach efficiently detects boundaries where nearby synaptic puncta meet. We then store the image with boundaries as an anti-merging mask.
B. It assesses voxels in the vicinity of all detected local maxima in order to model synapses as spheres or ellipsoids. Numerous algorithms using a global threshold as the first step to partition images result in either false positives or false negatives. This algorithm gradually expands a search region around each local maximum and calculates local thresholds for the voxels around each local maximum. First, we manually examined our image stacks for each synaptic label and measured the range of apparent synapse size, as determined by diameters for voxel clusters. We found that no voxel cluster had a diameter greater than 1 µm (radius <= 0.5 µm). To proceed, we assumed that local maxima were the centroids of synaptic label, in which case, for each local maximum, the potential synaptic voxel cluster would not occupy voxels more than 0.5 µm away from the local maximum. Therefore, we defined a maximum searching region of 0.5 µm in radius, here, about 4 voxels in radius. Our algorithm starts at each local maximum, assigns voxels within 1 voxel range as neighbors, and calculates the median gray value of the neighbors as local thresholds. Next, the algorithm automatically assigns each neighbor whose gray value passes the corresponding local threshold as a segmented synapse. Then, we re-assign the new centroids of each segmented synapse and iteratively repeat the above steps with increasing radius up to the maximum searching radius.

Once each of these tasks is complete, the algorithm performs a voxelwise AND operation on the results of the two independent tasks. For each resulting putative synapse, we calculate the volume and then eliminate putative synapses whose volumes are unrealistically small (less than

9 voxels). Finally, using the Object Manager tool of Imaris, we can feed our segmented synapses back into Imaris for further measurements and visualization.

Matlab codes are available in Open Science Framework (DOI 10.17605/OSF.IO/FR35X).

3.5.2 Segmentation results

Synapses of various types are typically identified at the light microscope by staining for specific proteins that are characteristic of the pre-synaptic terminal or of the post-synaptic specialization. In many neurons, excitatory synapses occur on small protrusions known as dendritic spines, and in such neurons the physical segregation of synaptic label ensures that excitatory synapse segmentation is a relatively straightforward process. Aspiny neurons, however, which lack such clearly defined synapses, can present more challenges to synapse segmentation, as can inhibitory synapses, which in mature neurons may be densely clustered near the cell body. The Lateral Superior Olive (LSO) provides an appropriate challenge for our segmentation algorithm, as the cells are aspiny and they exhibit significant inhibitory density at the cell body. Example results for synapse segmentation in the LSO are shown in Figure 2, where we stained for the synaptic protein gephyrin. Gephyrin is a postsynaptic scaffolding protein found at ionotropic inhibitory synapses (Groeneweg et al., 2018), and in mature neurons gephyrin is found primarily at or near the cell body, as seen in the (green) gephyrin stain of Figure 2A. After finding the summed image (Fig. 2B), we extracted from it the local maxima (Fig. 2C) to create an anti-merging mask (Fig. 2D). From the same set of local maxima, we iteratively expanded the searching region and applied the calculated local thresholds (Fig. 2E-H). Unsurprisingly, as the search radius increased, putative segmented synapses began to merge. By applying the anti-merging mask, we prevented this merging and maintained segregation of putative synapses (Figs. 2I and 3A3).

As shown in Figure 3, the segmentation algorithm described above was able to distinguish synapses that touch or very nearly touch (Fig. 3 A3 – D3). However, the algorithm also identified numerous small synapses that were likely falsely segmented due to background noise. In theory, one could expand the step between each iteration of threshold reduction to smooth out the noise and reduce the number of false synapse identifications. As we increased the size of the iterative thresholding steps from 2 to 20 gray-value for the 8-bit image (Fig. 3), the number of falsely identified synapses did not change appreciably.

In an ideal scenario for synapse labeling, imaging, and segmentation, the histogram of voxel gray values would reveal two easily separable peaks representing background label on the lower end and synapse label on the upper end. Due to the large number of voxels with low gray values in the background, our histogram was dramatically biased towards the lower end of the histogram. Whereas our background histograms might range from gray values of 0 to 20 or even 30, the synapse histograms had wide ranges that could dip as low as gray value 10, causing the two histograms to overlap. In this real-world example, the wide spread of gray values for synaptic label and the overlap of this range with the background label create challenges for distinguishing true signal from noise. To address this problem, we added a special user-guided noise removal procedure. Within each image stack, before the algorithm starts, we visually selected 3 to 5 potential synapses and plotted their gray value histograms. As a conservative measure, we assigned a noise threshold at a gray value that was at least 5 steps lower than the smallest value in the synapse histogram. During the iterative thresholding procedure, the lowest threshold was set to this noise threshold. In this example, we set the noise threshold at a gray value of 9. When we performed the segmentation routine after removing noise in this manner, the same data set yielded fewer false positive synapses (Fig. 4). The size of the incremental threshold reduction was an important parameter. A step size that was too large, e.g., a gray value of 20, missed some synaptic label altogether, and the ideal increment appeared to lie between 2 and 10 in gray value (Fig. 4 A -C), as increments in this range allowed the algorithm not only to separate synapses in close proximity, but also to eliminate noisy background labeling.

3.5.3 Pre- and post- synaptic partners

A common task after synapse segmentation is to determine whether two synaptic labels appose each other across a synaptic cleft. As the distance between two apposing synaptic labels across the cleft is below the resolution of conventional light microscopy, correlation-based colocalization methods have traditionally been adopted to tackle this task. For example, the Pearson's coefficient is used to estimate the degree of correlation between two labels in microscopic image analysis (for an excellent textbook, see Wu et al., 2008), whereas the Mander's overlap coefficients use the actual overlap of the signal to estimate the contribution of each labels (Mander et al., 1993). However, these correlation-based methods assume that pre- and post-synaptic label are smeared by the point-spread function of the imaging system, and provide no information about relative position. Here, using the centroids of our segmented synapses, we provide a Euclidean-distance-based method to calculate apposition and relative proximity of pre- and post- synaptic labels.

The vesicular inhibitory transporter VIAAT transports both GABA and glycine into synaptic vesicles in presynaptic inhibitory terminals, and so is generally found in pre-synaptic terminals apposed to gephyrin-positive postsynaptic densities (Burger et al., 1991; Dzyubenko et al., 2016). To segment apposed pre- and post-synaptic signal, we stained tissue for VIAAT and gephyrin (Fig. 5A-C). Gephyrin-positive clusters of staining outlined the soma, consistent with previous results from this lab and others (Alan Cooper thesis; Fischer et al. 2019; Korada and Schwartz 1999), and both gephyrin-positive and VIAAT-positive label could be segmented around the soma (Fig. 5D-H). Correlation-based colocalization approaches provide an overall estimate of overlapping intensity alone (Pearson's R value = 0.23; Manders' coefficients = 0.344 and 0.478 for VIAAT and gephyrin). To estimate the distance between these two synaptic labels, we extracted centroids for gephyrin- and VIAAT-labeled synapses (Fig. 6A). Next, for the calculated set of gephyrin centroids, we calculated the distance from the nearest VIAAT centroids (Fig. 6B), and for the set of VIAAT centroids we plotted the distribution of distances to the nearest gephyrin centroid (Fig. 6C). A clear majority (80%) of VIAAT centroids fell within 1 µm of identified gephyrin centroids, whereas only half of the gephyrin centroids fell within 1 µm of identified VIAAT centroids. This asymmetry may be partly explained by the differences in labeling for pre and postsynaptic proteins, as clusters of presynaptic label in our dataset outnumbered clusters of postsynaptic label by over 50% (348 vs 202).

In order to validate our distances between pre- and post- synaptic label, we manually examined the unprocessed stacks of gephyrin and VIAAT staining and selected 34 synapses in which both proteins were robustly labeled. We then estimated the centroid-to-centroid distance in ImageJ. The median distance was 0.83 µm 25th percentile: 0.74, 75th percentile: 0.97, n = 41), with largest distance of 1.13 µm and smallest distance of 0.58 µm. Using the 75th percentile, we defined the threshold limit for putative synaptic label with 1µm between pre- and post-synaptic label, and then applied this threshold distance to the segmented labels. We randomly selected 5 gephyrin and VIAAT centroids. For each centroid, we built a searching sphere with radius of 1 µm (z-stack corrected) and calculated the probability of at least one synaptic partner in the sphere (Fig. 7 and Fig. 8). We repeated with random selection 20 times (sampling with replacement) for each synaptic labels and calculated the cumulative probability of finding synaptic partners in the searching sphere. The probability of finding a synaptic partner in the searching sphere for a gephyrin centroid is 30% higher than the probability of finding a synaptic partner for a VIAAT centroid (gephyrin: 0.76 ± 0.22; VIAAT:0.51 ± 0.21; $p = 0.0014$ Mann-Whitney). These probabilities are consistent with the distribution of nearest-neighbour distances (Fig. 6B, C) and provide information about relative position that the correlation-based colocalization method cannot provide.

3.6 Discussion

We labeled neurons with exogenous dyes and collected image stacks at the confocal microscope to obtain realistically challenging datasets for evaluating currently available software packages for 3D reconstruction. Some of these packages are impressive, but each one lacks certain desirable features. The major advance described here is the implementation of an efficient algorithm for 3D synapse segmentation, which allows us to identify synaptic partners from either pre- or post- synaptic label.

3.6.1 Neuronal reconstruction

Since 2010, researchers have made tremendous progress by implementing auto/semi-auto reconstruction algorithms. However, none of the existing software packages for 3D reconstruction are able to automatically and robustly trace a wide range of neuron morphologies. Even semi-auto tracing requires a substantial amount of fine-scale editing. Neurolucida and Imaris provide the most efficient semi-automatic tracing interface. However, Imaris fails to reconstruct the apical dendrite when the dendrite diameter is too large. Both Neurolucida and Imaris struggle with situations in which two branches are close to each other and one branch has a gap in staining. In fact, during semi-auto tracing these programs often connect broken branches to neighboring neurons. The human operator must then construct short cylinders manually to appropriately bridge gaps at broken branches. Performance decreases for neurons that exhibit beads-on-a-string morphology.

The ideal reconstruction software packages should integrate 3D image processing, 3D tracing, 3D segmentation, and 3D visualization. Although some software packages, including Vaa3D, ImageJ (with numerous plugins), Neurolucida, Imaris, Aivia, and Amira claim to do a wide range of tasks, specific functions of any one package may be limited. For example, we found Neurolucida to be the best program for neuronal tracing, both in terms of performance under low signal-to-noise and where precise estimates of dendrite diameter were desired (e.g., for compartmental modeling of dendritic integration). However, the synapse segmentation performance was poor. Amira, on the other hand, performed well for image processing and segmentation generally, but had limited ability to trace neurons. Boosted by the DIADEM challenge, a growing number of labs and private companies are investing in the development of more robust tracing algorithm and software packages. More recently, the BigNeuron project was launched to advance parameters for state-of-the-art neuronal reconstruction, to develop standardized reconstruction and morphological analysis protocols, and to establish an open data repository/source for neuroscientists (Peng et al., 2015).

3.6.2 Synapse segmentation

Based on iterative thresholding and watershed algorithm, our synapse segmentation efficiently and accurately separates synapses in close proximity that are demonstrably challenging for other algorithms. In particular, adding an extra background removal step makes our segmentation routine robust to the kinds of noise that occur in real-world biological imaging. The size of the step at each iteration of the thresholding procedure is important; a step of 5 gray-value units appears to be optimal for accurate and robust segmentation of 8-bit images. To validate the segmentation results, a few examiners with prior knowledge on immunofluorescent image manually segmented synapses randomly. In order to do so, for a potential synapse, the examiner would go through each optical sections and count the total pixels representing the synapse and approximate the centroid of the synapse. Then, I compared the manual segmentation and automated segmentation results. By visual inspection, both results have the same overall shape. The centroid and the overall pixel (voxel) numbers are also in agreement. Ideally, we would compare our segmentation results with the ultra-structures from the same tissue. With access to appropriate infrastructure, we might carry out this comparison using correlative light and electron microscopy (CLEM), an imaging approach that correlates information obtained from fluorescence light microscopy with that obtained from electron microscopy, providing information for subcellular location of molecules as well as cell ultrastructure (for review, see van den Dries et al., 2022).

Although Pearson's and Manders' coefficients have been widely adopted for colocalization analyses of dual-labelled synapses, these measures are insufficiently precise for many questions. Our Euclidean-distance-based approach identifies the synaptic partner in the searching sphere with radius of threshold distance and calculates the probability of a synaptic partner in the searching sphere.

In order to be able to unequivocally assign synapses to a reconstructed neuron, a postsynaptic label – such as the gephyrin label used to identify inhibitory synapses – is admittedly preferred. Unfortunately, many postsynaptic receptor proteins, as well as their associated proteins, are notoriously recalcitrant to immunolabeling in tissue. For example, PSD-95 (postsynaptic density protein 95 KDa), an anchoring protein for NMDA and AMPA receptors (Gomperts, 1996), would appear to be an ideal postsynaptic marker for glutamatergic synapses. However, neither we nor others have identified PSD-95 antibodies that could be successfully used for fluorescent staining in thick tissue. Instead, we used staining for the vesicular glutamate transporter VGLUT1, which is a reliable presynaptic marker for excitatory synapses in the LSO (Blaesse et al., 2005). Because co-staining for PSD-95 and VGLUT1 was not possible, we made the assumption that calculated distances between gephyrin and VIAAT immunolabeling at inhibitory synapses could be used to estimate distances between VGLUT1 and PSD-95 at glutamatergic synapses in the same cells. This assumption is based on ultrastructure studies in cats and guinea pigs, where the distances are similar between post-synaptic membranes and various types of pre-synaptic terminals (Helfert and Schwartz, 1986; Helfert et al., 1992). If the absence of reliable methods for identifying the post-synaptic glutamatergic specialization in thick tissue, we suggest that a reasonable approach is to stain for VIAAT and gephyrin in the same tissue, measure the inhibitory synapse Euclidean distance, and then use VGLUT1 staining, informed by the VIAAT-gephyrin distance, to identify those glutamatergic synapses likely to be associated with the labeled neuron.

3.7 References

Ancin H, Roysam B, Dufresne TE, Chestnut MM, Ridder GM, Szarowski DH, Turner JN (1996) Advances in automated 3-D image analysis of cell populations imaged by confocal microscopy. Cytometry 25:221–234.

Ascoli GA (2006) Mobilizing the base of neuroscience data: The case of neuronal morphologies. Nat Rev Neurosci 7:318–324.

Ascoli GA, Svoboda K, Liu Y (2009) The DIADEM Challenge. http://www.diademchallenge.org.

Blaesse P, Ehrhardt S, Friauf E, Nothwang HG (2005) Developmental pattern of three vesicular glutamate transporters in the rat superior olivary complex. Cell Tissue Res 320:33–50.

Bomans M, Höhne K-H, Tiede U, Riemer M (1990) 3-D Segementation of MR Images of the Head for 3-D DIsplay. IEEE Trans Med Imaging 9:177–183.

Broser PJ, Schulte R, Lang S, Roth Fritjof A, Helmchen, Waters J, Sakmann B, Wittum G (2004) Nonlinear anisotropic diffusion filtering of three-dimensional image data from two-photon microscopy. J Biomed Opt 9:1253.

Brown KM, Barrionuevo G, Canty AJ, De Paola V, Hirsch JA, Jefferis GSXE, Lu J, Snippe M, Sugihara I, Ascoli GA (2011) The DIADEM data sets: Representative light microscopy images of neuronal morphology to advance automation of digital reconstructions. Neuroinformatics 9:143–157.

Burger PM, Hell J, Mehl E, Krasel C, Lottspeich F, Jahn R (1991) GABA and glycine in synaptic vesicles: storage and transport characteristics. Neuron 7:287–293.

Burman P (1989) A Comparative Study of Ordinary Cross-Validation, v-Fold Cross-Validation and the Repeated Learning-Testing Methods. Biometrika 76:503.

Cardona A, Saalfeld S, Schindelin J, Arganda-Carreras I, Preibisch S, Longair M, Tomancak P, Hartenstein V, Douglas RJ (2012) TrakEM2 software for neural circuit reconstruction. PLoS One 7.

Cuntz H, Forstner F, Borst A, Häusser M (2010) One rule to grow them all: A general theory of neuronal branching and its practical application. PLoS Comput Biol 6.

Dzyubenko E, Rozenberg A, Hermann DM, Faissner A (2016) Colocalization of synapse marker proteins evaluated by STED-microscopy reveals patterns of neuronal synapse distribution in vitro. J Neurosci Methods 273:149–159.

Feng L, Zhao T, Kim J (2015) neuTube 1.0: A New Design for Efficient Neuron Reconstruction Software Based on the SWC Format. eNeuro2 2:1–10.

Fischer AU, Müller NIC, Deller T, Del Turco D, Fisch JO, Griesemer D, Kattler K, Maraslioglu A, Roemer V, Xu-Friedman MA, Walter J, Friauf E (2019) GABA is a modulator, rather than a classical transmitter, in the medial nucleus of the trapezoid body–lateral superior olive sound localization circuit. J Physiol 597:2269–2295.

Gomperts SN (1996) Clustering membrane proteins: It’s all coming together with the PSD-95/SAP90 protein family. Cell 84:659–662.

Groeneweg FL, Trattnig C, Kuhse J, Nawrotzki RA, Kirsch J (2018) Gephyrin: a key regulatory protein of inhibitory synapses and beyond. Histochem Cell Biol 150:489–508.

Helfert RH, Juiz JM, Bledsoe SC, Bonneau JM, Wenthold RJ, Altschuler RA (1992) Patterns of glutamate, glycine, and GABA immunolabeling in four synaptic terminal classes in the lateral superior olive of the guinea pig. J Comp Neurol 323:305–325.

Helfert RH, Schwartz IR (1986) Morphological evidence for the existence of multiple neuronal classes in the cat lateral superior olivary nucleus. J Comp Neurol 244:533–549.

Jin DZ, Zhao T, Hunt DL, Tillage RP, Hsu CL, Spruston N (2019) ShuTu: Open-Source Software for Efficient and Accurate Reconstruction of Dendritic Morphology. Front Neuroinform 13:1–19.

Korada S, Schwartz IR (1999) Development of GABA, glycine, and their receptors in the auditory brainstem of gerbil: A light and electron microscopic study. J Comp Neurol 409:664–681.

Kvilekval K, Fedorov D, Obara B, Singh A, Manjunath BS (2009) Bisque: A platform for bioimage analysis and management. Bioinformatics 26:544–552.

Longair MH, Baker DA, Armstrong JD (2011) Simple neurite tracer: Open source software for reconstruction, visualization and analysis of neuronal processes. Bioinformatics 27:2453–2454.

Mander E, Verbeek F, Aten J (1993) Measurement of co-localization of objects in dual-colour confocal images. J Microsc 169:375–382.

Meijering E, Jacob M, Sarria J-CF, Steiner P, Hirling H, Unser M (2004) Design and validation of a tool for neurite tracing and analysis in fluorescence microscopy images. Cytometry 58A:167–176.

Morgan JL, Schubert T, Wong ROL (2008) Developmental patterning of glutamatergic synapses onto retinal ganglion cells. Neural Dev 3:0–18.

Myatt DR, Hadlington T, Ascoli GA, Nasuto SJ (2012) Neuromantic - from semi-manual to semi-automatic reconstruction of neuron morphology. Front Neuroinform 6:1–14.

Peng H, Hawrylycz M, Roskams J, Hill S, Spruston N, Meijering E, Ascoli GA (2015) BigNeuron: Large-scale 3D Neuron Reconstruction from Optical Microscopy Images. Neuron 87:252–256.

Peng H, Ruan Z, Long F, Simpson JH, Myers EW (2010) V3D enables real-time 3D visualization and quantitative analysis of large-scale biological image data sets. Nat Biotechnol 28:348–353.

Pool M, Thiemann J, Bar-Or A, Fournier AE (2008) NeuriteTracer: A novel ImageJ plugin for automated quantification of neurite outgrowth. J Neurosci Methods 168:134–139.

Rall W (1959) Branching dendritic trees and motoneuron membrane resistivity. Exp Neurol 1:491–527.

Rall W, Burke RE, Smith TG, Nelson PG, Frank K (1967) Location of Synapses and Mechanisms for the Monosynaptic in Motoneurons Possible. J Neurophysiol 30:884–915.

Ridler TW, Calvard S (1978) Picture Thresholding Using an Iterative Slection Method. IEEE Trans Syst Man Cybern SMC-8:630–632.

Roysam B, Ancin H, Bhattacharjya AK, Chisti MA, Seegal R, Turner JN (1994) Algorithms for automated characterization of cell populations in thick specimens from 3-D confocal fluorescence microscopy data. J Microsc 173:115–126.

Soltanian-Zadeh S, Sahingur K, Blau S, Gong Y, Farsiu S (2019) Fast and robust active neuron segmentation in two-photon calcium imaging using spatiotemporal deep learning. Proc Natl Acad Sci U S A 116:8554–8563.

Stone M (1977) Asymptotics For and Against Cross-Validation. Biometrika 64:29–35.

Turetken E, Benmansour F, Fua P (2012) Automated reconstruction of tree structures using path classifiers and Mixed Integer Programming. Proc IEEE Comput Soc Conf Comput Vis

Pattern Recognit:566–573.

van den Dries K, Fransen J, Cambi A (2022) Fluorescence CLEM in biology: historic developments and current super-resolution applications. FEBS Lett 596:2486–2496.

Wang Y, Narayanaswamy A, Tsai CL, Roysam B (2011) A broadly applicable 3-D neuron tracing method based on open-curve snake. Neuroinformatics 9:193–217.

Weaver CM, Hof PR, Wearne SL, Lindquist WB (2004) Automated algorithms for multiscale morphometry of neuronal dendrites. Neural Comput 16:1353–1383.

Wu Q, Merchant FA, Castleman KR (2008) Microscope Image Processing. Academic press.

3.8 Tables

Table 1

Freeware	Image Processing	Image Segmentation	3D Reconstruction	3D Visualization	Auto Tracing	Manual Edition	Stitching	Script Interaction	Integration	Language for Developer
Vaa3D	*****	****	***	**	Y	***	Y	Matlab		C++
Farsight	Y	Y	Y	Y	Y	Y	Y	Python		C++
NeuTube	N	N	N	**	Y	***	N	N/A	Vaa3D	C++
TrakEM2	N	**	N	N	N	**	Y	N/A	ImageJ	Java
NeuRA	**	**	+	N	Y	**	N	N/A		Java
TREES Toolbox	**	**	**	N	Y	**	N	Matlab/ NEURON		
ShuTu	N	N	N	**	Y	**	Y	Python		N/A
Neuromantic	**	N	**	N	N	**	N	N/A		N/A
BisQue	****	**	**	**	N	*	Y	Matlab/ Python		C++/ JAVA
Simple Neurite Tracer	N	N	**	**	N	**	N	N/A	ImageJ	N/A
Tubular Geodesics	**	N	**	**	N	N	N	N/A	ImageJ	N/A
NeuronJ	**	N	N	N	N	**	Y	N/A	ImageJ	N/A
NeuriteTracer	N	**	N	N	Y	N	N	N/A	ImageJ	N/A
Commercial Software										
Imaris	*****	****	****	*****	Y	****	Y	Matlab/ Python		N/A
NeuroLucida	*****	**	*****	*****	Y	*****	Y	N/A		N/A
Aivia	*****	****	***	***	Y	***	N	N/A		N/A
3DMA-NEURON	Y	N	Y	N	Y	Y	N	N/A		N/A
Amira	*****	***	****	***	N	N	Y	N/A		C++

Available software packages for 3D neuronal reconstruction as of August 2019. Image processing rates the package on the performance and versatility of image processing. Image segmentation rates the package on segmenting objects including somata and synapses. 3D reconstruction rates the package on the performance of creating the 3D model for segmented objects or traced neurites. 3D visualization rates the package on the performance of 3D visualization. Auto tracing asks whether the package can trace neurites automatically. Manual edition rates the package on the performance of semiauto/manual tracing. Stitching asks if the package itself is able to register images. Script interaction asks whether and what script language the package allows users to write to implement their own functions within the package. Integration indicates that the package acts as a plugin to another piece of software. Language for developer indicates that the package is open source and allows the developer to modify and/or contribute.
***** best performance of tested packages
*** average performance
* poor performance.
Note: As Farsight and 3DMA-NEURON were unavailable for testing, their claimed performance is in gray.

Table 2

Antigen	Host (Isoform)	Catalogue number	Dilution	Conjugated Fluorophores
Gephyrin	Mouse IgG1	Synaptic System 147021	1:250	
VGLUT1	Guinea pig	Millipore AB5905	1:2000	
VIAAT	Rabbit	Synaptic System 131002	1:1000	
Mouse	Donkey	Jackson Immuno Research 715605151	1:500	Alexa 647
Guinea pig	Donkey	Jackson Immuno Research 715165151	1:500	Cy 3
Rabbit	Donkey	Jackson Immuno Research 711486152	1:500	Dylight 488

Antibodies used in this study.

3.9 Figures

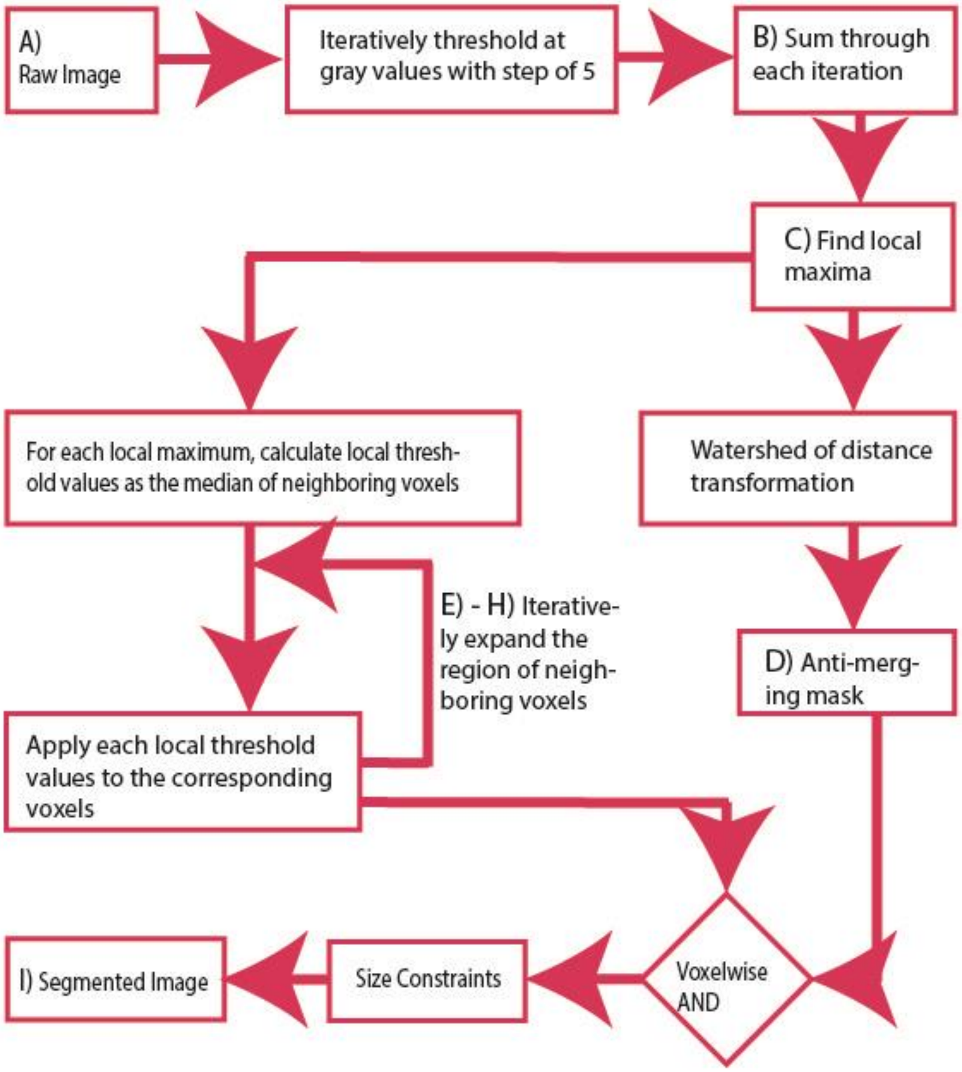

Figure 3-1

Figure 1. Flowchart of algorithm pipeline for 3D synapse segmentation.

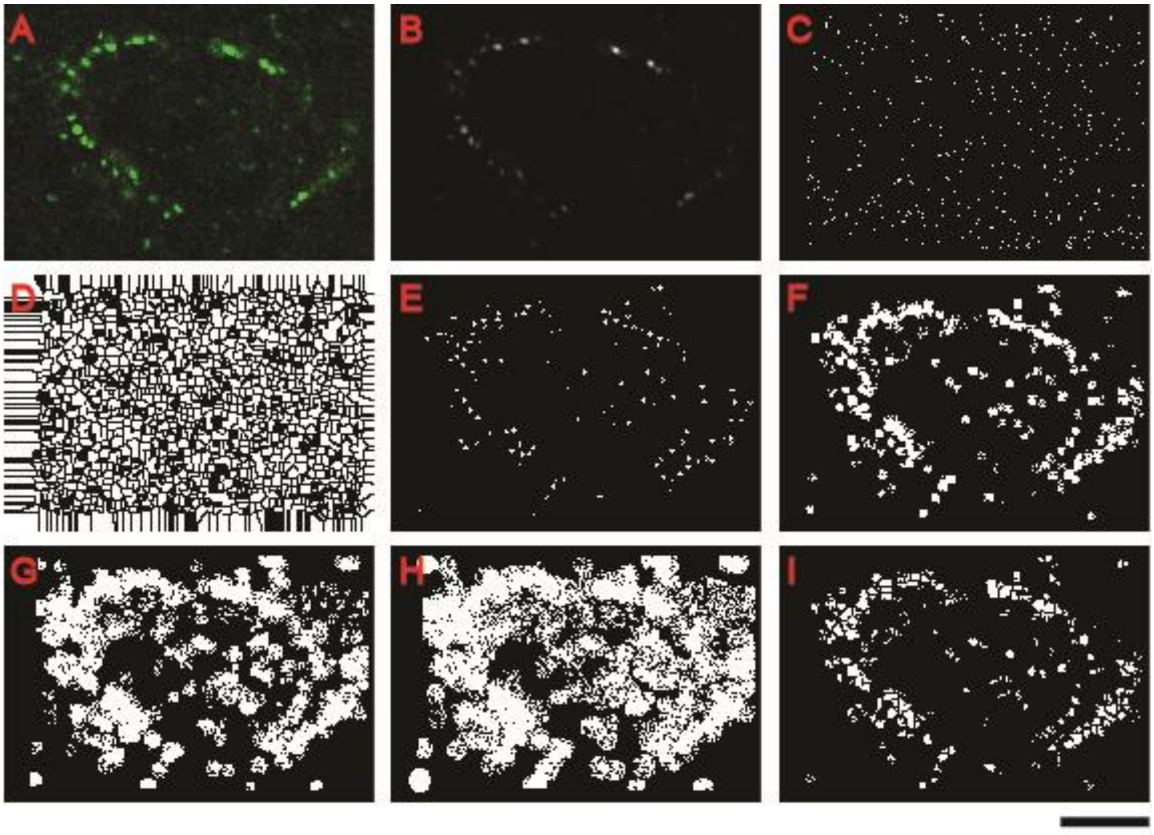

Figure 3-2

Figure 2. Segmentation results step by step corresponding to steps from figure 1. A. Raw image with gephyrin labelled in green. B. Sum of each binary image that passes the threshold. C. Local maxima of the image. D. Anti-merging mask. E. Segmentation result after applying local thresholds with searching sphere of 1 voxel radius. F. Segmentation result after applying local thresholds with searching sphere of 2 voxel radius. G. Segmentation result after applying local thresholds with searching sphere of 3 voxel radius. H. Segmentation result after applying local thresholds with searching sphere of 4 voxel radius. I. Final segmentation result. All images are contrast enhanced for illustration purpose. Scale bar = 5 µm.

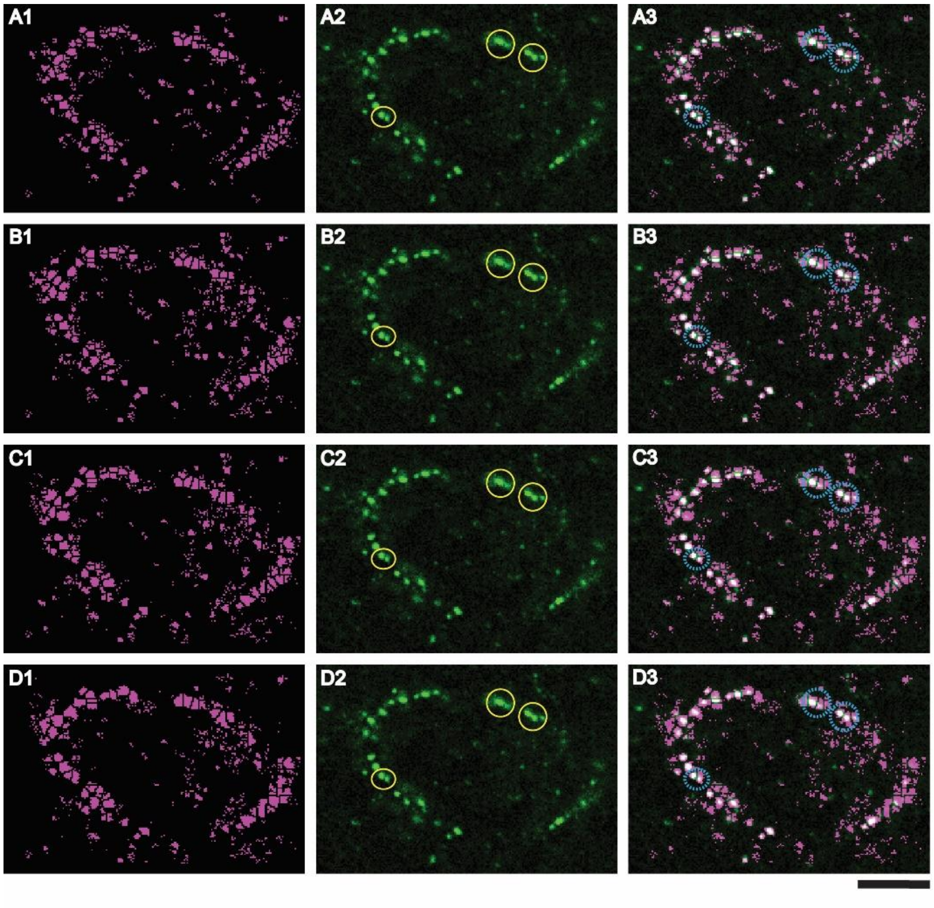

Figure 3-3

Figure 3. Increasing the size of iterative thresholding step below 20 does little to reduce false positive rate. A - D: Segmentation results with iterative thresholding step size of 2 gray value (A1), 5 gray value (B1), 10 gray value (C1), and 20 gray value (D1) are merged (A3 - D3) with raw images (A2 - D2). Solid yellow circles show potential synapses that are touching or close to each other. Dashed cyan circles show that segmentation can distinguish synapses that are touching or close to each other (shown in solid circles). All images are contrast-enhanced for illustration purposes. Scale bar = 5 µm.

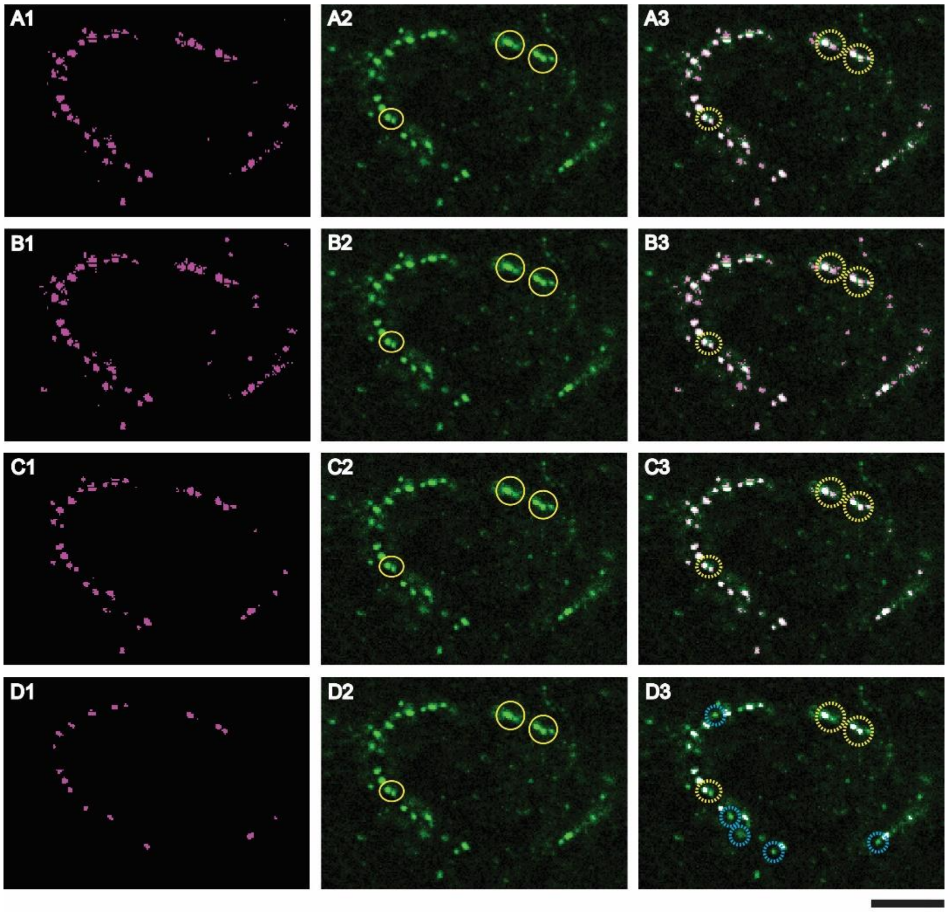

Figure 3-4

Figure 4. Increasing the size of iterative thresholding step changes segmentation results in noise-smoothed images. A - D: Segmentation results with iterative thresholding step size of 2 gray value (A1), 5 gray value (B1), 10 gray value (C1), and 20 gray value(D1) are merged (A3 - D3) with raw images (A2 - D2). Solid yellow circles show potential synapses are toughing or close to each other. Dashed yellow circles show the segmentation results of synapses shown in solid circle. Dashed cyan circles show missed potential synapses. All images are contrast-enhanced for illustration purposes. Scale bar = 5 µm.

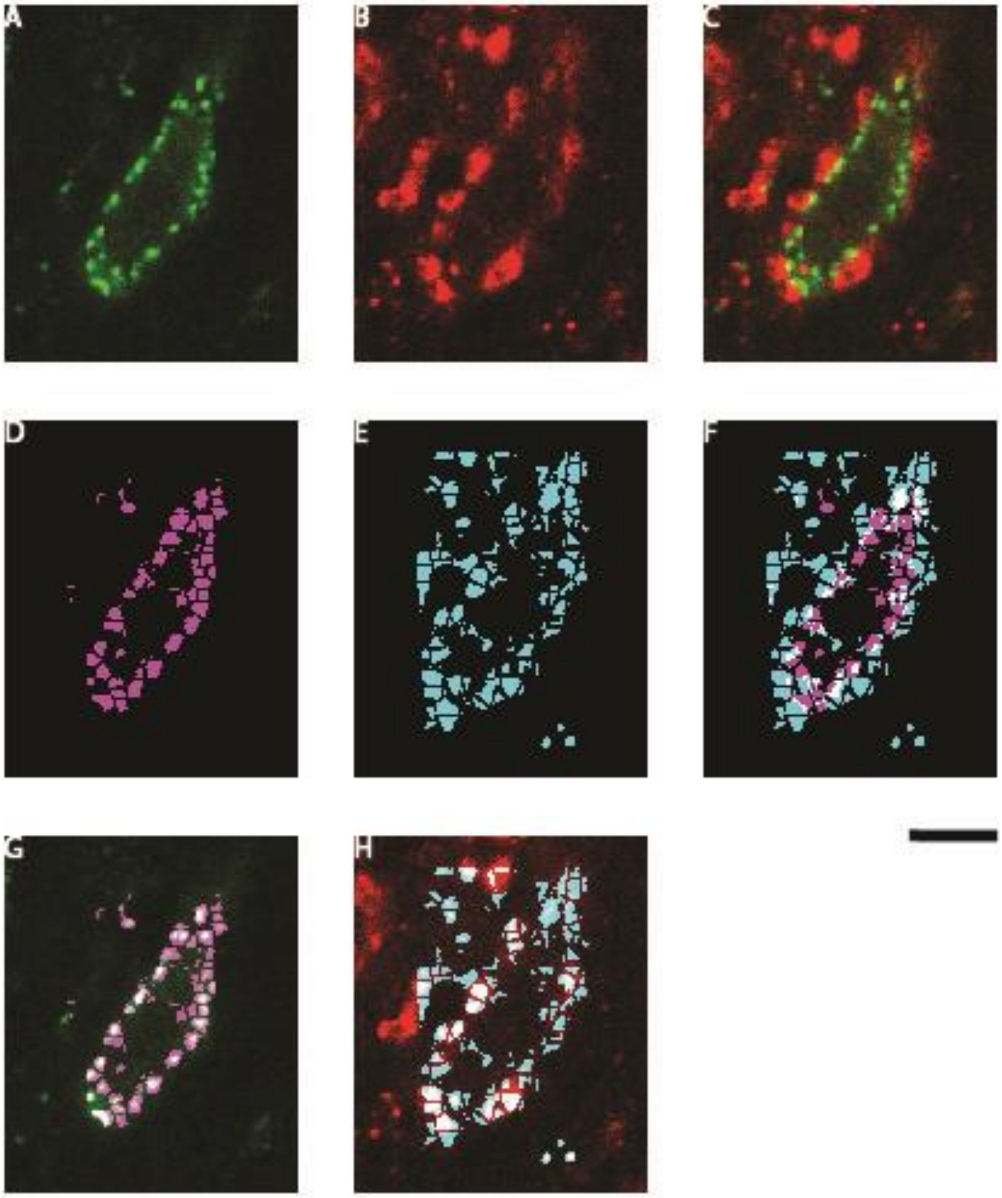

Figure 3-5

Figure 5. Segmentation of somatic gephyrin and VIAAT labels at single optical section. A. Raw image of gephyrin label. B. Raw image of VIAAT label. C. Merged image of gephyrin and VIAAT labels. D. Gephyrin segmentation. E. VIAAT segmentation. F. Merged image of gephyrin and VIAAT segmentation. G. Merged image of gephyrin label and gephyrin segmentation. H. Merged image of VIAAT label and VIAAT segmentation. All images are contrast enhanced for illustration purposes. Scale bar = 5 µm.

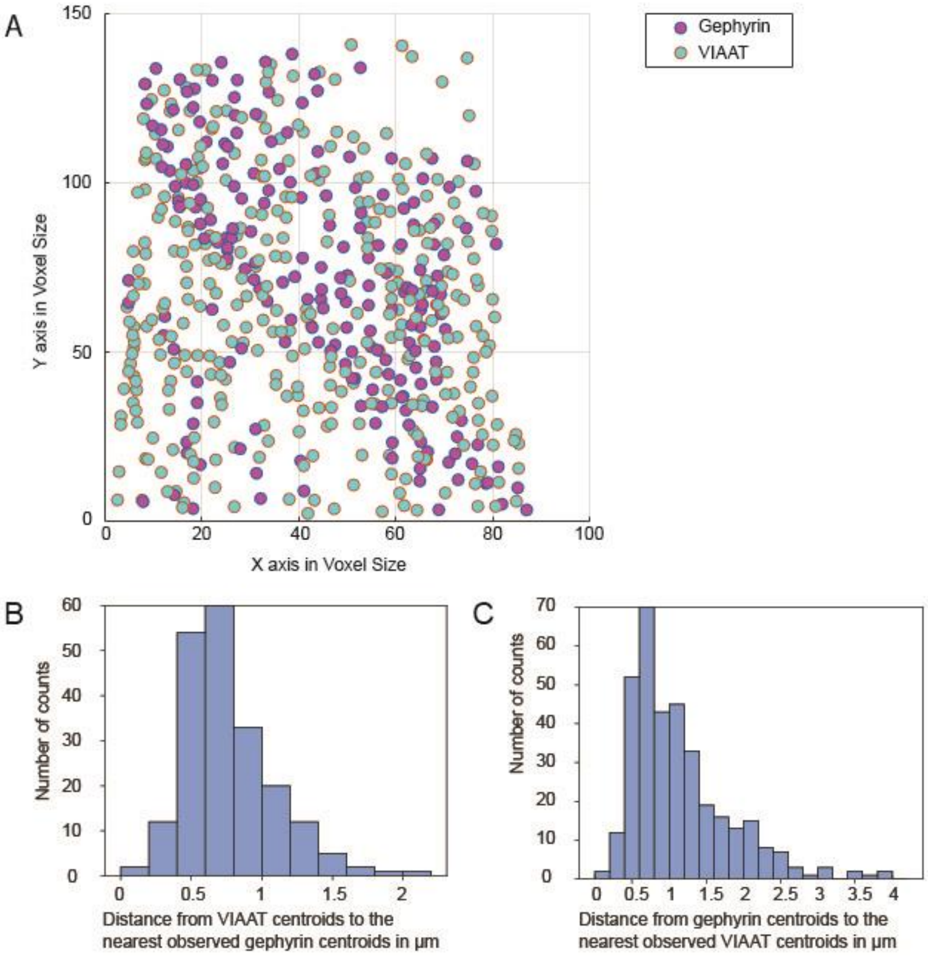

Figure 3-6

Figure 6. Nearest neighbor analysis of gephyrin and VIAAT centroids. A. Centroids of gephyrin and VIAAT. B. For each individual gephyrin centroid, the distance to the nearest VIAAT centroid is calculated. The histogram shows the counts of distances to nearest VIAAT centroids. C. For each individual VIAAT centroid, the distance to the nearest gephyrin centroid is calculated. The histogram shows the counts of distances to nearest gephyrin centroids.

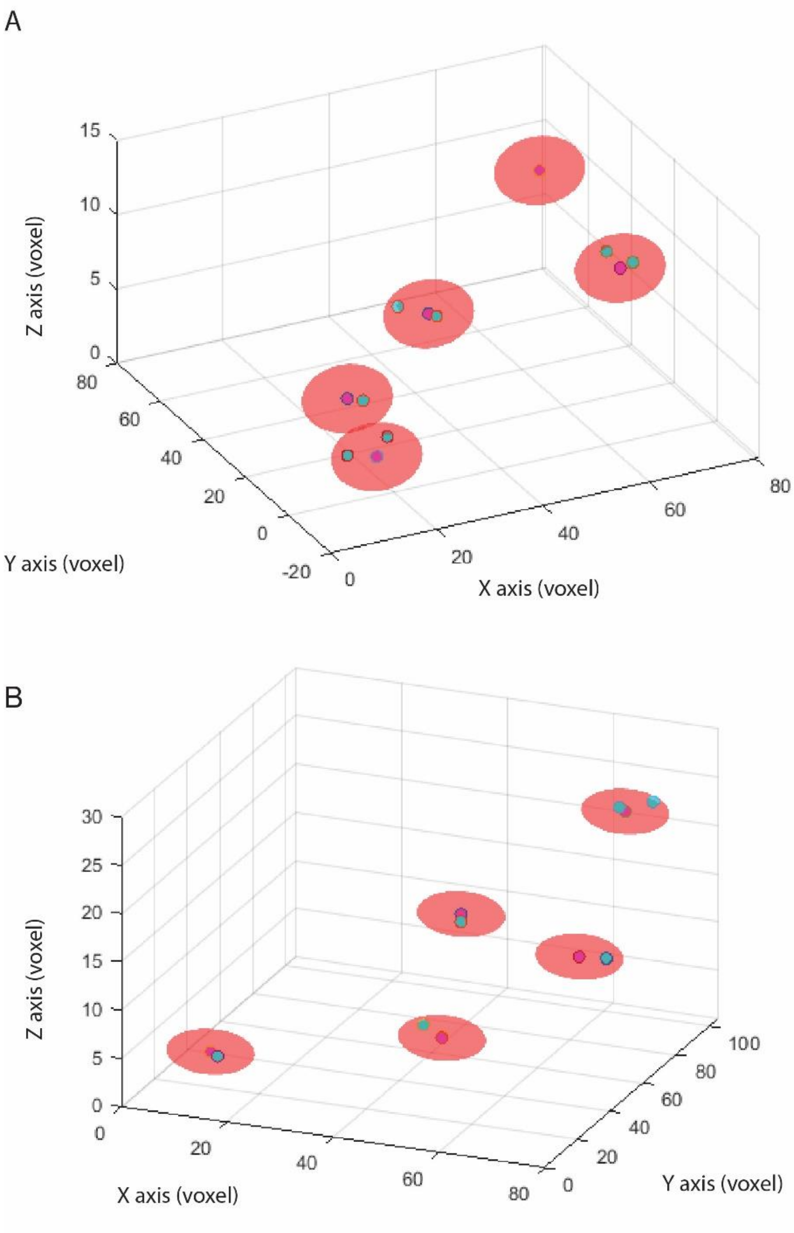

Figure 3-7

Figure 7. Searching spheres for observed postsynaptic labels with potential presynaptic partner. A and B searching spheres for 10 randomly selected gephyrin centroids. Magenta dots: Gephyrin centroids. Cyan dots: VIAAT centroids. Red sphere: searching sphere for gephyrin centroid.

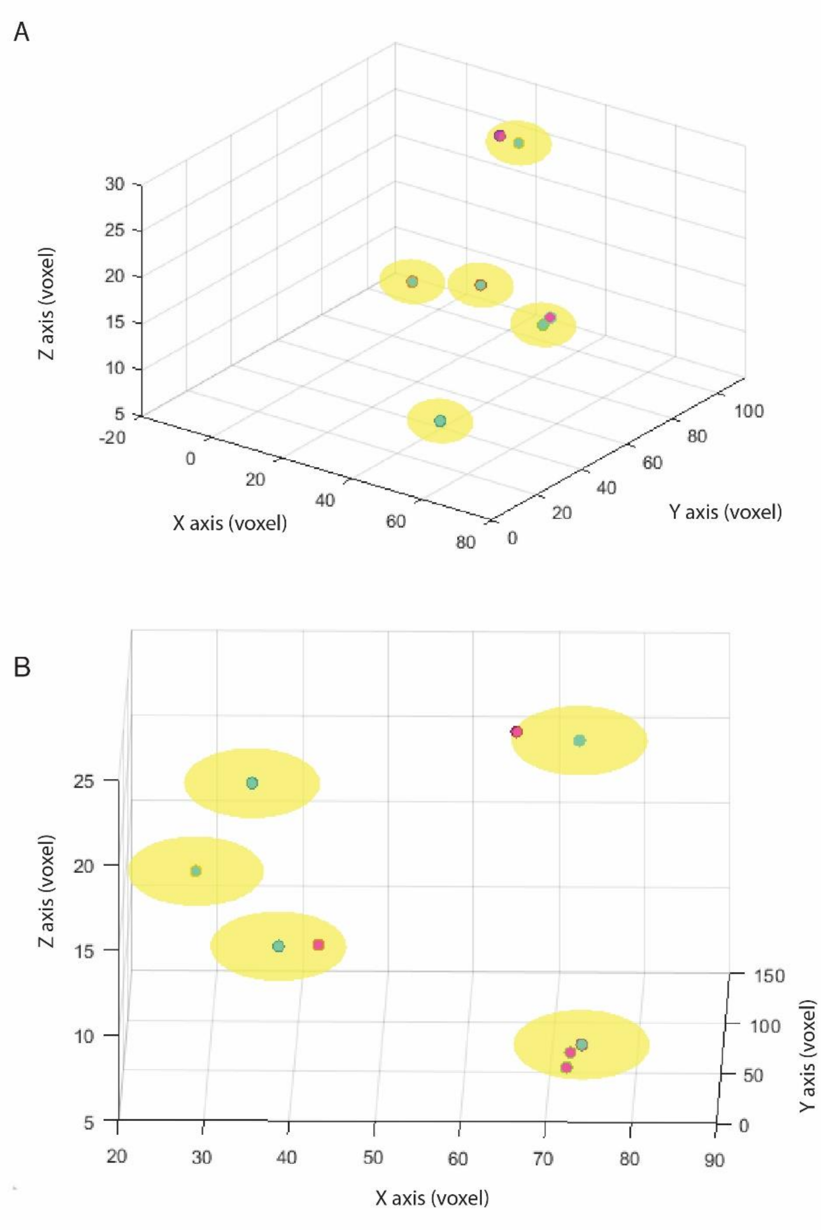

Figure 3-8

Figure 8. Searching spheres for observed presynaptic labels with potential postsynaptic parterner. A and B searching spheres for 10 randomly selected VIAAT centroids. Magenta dots: Gephyrin centroids. Cyan dots: VIAAT centroids. Yellow sphere: searching sphere for VIAAT centroid.

4 Chapter 4: Redistribution of synaptic inputs in the neonatal rat auditory brainstem occurs in the absence of acoustically driven activity

4.1 Abstract

Principal cells of the lateral superior olive (LSO) integrate excitatory and inhibitory inputs that are precisely matched for stimulus frequency. Despite the importance of frequency-matched inputs to the LSO's task, how this precise registration is established and refined is not well understood. Both excitatory and inhibitory inputs to LSO undergo significant physiologically measurable refinement before hearing onset. Although physiological measurable refinement could be attributed in part to the change in the subcellular location of the synapses, how excitatory and inhibitory synapses are distributed and/or re-distributed during developmental refinement has not been closely studied in the LSO. In the medial superior olive (MSO), a neighboring nucleus to the LSO, inhibitory synapses onto principal cells have been shown to be re-distributed towards the soma under the influence of acoustic experience. Here, we asked how synapses in LSO are distributed in early postnatal life, and whether this distribution can occur in the absence of acoustic activity. To answer this question, we labeled individual principal cells in the LSO of rats at about postnatal days 4 and 11 (P4 and P11), both ages before hearing onset, and stained for markers of excitatory and inhibitory synapses. We then reconstructed the labeled cells, together with their associated synapses, in three dimensions. Surprisingly, at early ages, excitatory synapses outnumbered inhibitory synapses at the soma by a factor of 2. As expected, within the week before hearing onset, synapse size increased for both excitatory and inhibitory inputs. For inhibitory synapses, absolute synapse density decreased at distal dendrites and increased at soma and proximal dendrites. Excitatory synapses showed a complementary trend, such that absolute synapse density increased at distal dendrites and decreased at soma and proximal dendrites. Together, these trends resulted in a situation in which by P11, just before hearing onset, inhibitory synapses outnumbered excitatory synapses at the soma by a factor of 3. Our results show that in the immature LSO, inhibitory synapses are re-distributed toward the soma, and excitatory synapses re-distributed away from the soma, in the absence of acoustic activity.

4.2 Introduction

Neural circuit function is heavily influenced by cellular morphology and protein expression, and it has long been known that neural activity, especially during development, alters efficacy of excitatory synapses through changes in both dendritic morphology (Yuste, 2010) and protein expression. Efficacy of inhibitory synapses can also by modified by changes in protein structure and function (Rivera et al., 1999; Ganguly et al., 2001; Schubert et al., 2013). Perhaps the best-known way in which neural activity alters synaptic efficacy is through protein expression; and such changes can be quite dynamic even at adult synapses. Although both the subcellular location and the relative distribution of synapses also affect synapse efficacy (Rall and Rinzel, 1973; Bernander et al., 1994), less is known about the role of neural activity in specifying synapse position.

In retinal ganglion cells, the number of glutamatergic synapses increases concomitant with a decrease in dendritic field density (Morgan et al., 2008). In primary visual cortex, blockade of GABAergic transmission from basket cells results in more synapses with smaller size on the somata of pyramidal cells (Wu et al., 2012). Thus, in both excitatory and inhibitory circuits, protein expression at individual synapses and subcellular distribution of those synapses can change significantly, whether permitted or guided by neural activity. Understanding how individual neurons coordinately refine the location and strength of their excitatory and inhibitory synapses however remains unknown. What is known is that neural activity can regulate the subcellular distribution of synaptic inputs to individual neurons such that neighbouring synapses cluster with each other through local calcium signals (Kleindienst et al., 2011; Druckmann et al., 2014; Winnubst et al., 2015; Lee et al., 2016). In one of the best-studied preparations, mature proportions of excitatory and inhibitory synapses are established onto different types of retinal ganglion cells at different times during development (Bleckert et al., 2013). In this system, the ratio of excitatory to inhibitory synapse onto given segments of dendrite is maintained throughout early postnatal development (Soto et al., 2011a; Bleckert et al., 2013).

The lateral superior olive (LSO) is a model system for studies of the coordinate refinement of excitatory and inhibitory synapses. Principal cells in LSO compute interaural level difference (ILD) (Boudreau and Tsuchitani, 1968) by integrating excitatory input from the ipsilateral anteroventral cochlear nucleus (AVCN) (Cant and Casseday, 1986) and inhibitory input from the ipsilateral medial nucleus of the trapezoid body (MNTB), which receive excitatory input from the contralateral AVCN (Moore and Caspary, 1983; Bledsoe et al., 1990; Sommer et al., 1993; Smith et al., 1998). The period between birth and hearing onset (around P12 in rats (Geal-Dor et al., 1993)) in the LSO comprises many developmental events for both pathways. The excitatory and inhibitory inputs to LSO are crudely aligned already at birth (Sanes and Siverls, 1991; Kandler and Friauf, 1993; Kil et al., 1995), and each input pathway undergoes further refinement before hearing onset. For example, the number of excitatory inputs to individual LSO neurons decreases, with the remaining inputs growing stronger (Case et al., 2011). This physiologically measurable refinement coincides with developmental changes in ionotropic glutamate receptor expression, including increased expression of the GluR4 AMPA receptor subunit, decreased expression of the GluN2B NMDA receptor subunit, and a shift from NMDAR- to AMPAR-mediated transmission (Caicedo and Eybalin, 1999; Case et al., 2011). During the same time, inhibitory inputs to LSO also undergo functional refinement. In particular, the overall area of MNTB that can elicit a response in a single LSO neuron decreases – in other words, the number of distinct inputs to each LSO cell decreases – and the strength of the remaining inputs increases (Kim and Kandler, 2003). This physiologically measurable refinement coincides with developmental changes in inhibitory receptor expression, including a shift from GABAergic to glycinergic transmission and increased expression of α1-containing glycine receptors (Friauf et al., 1997; Kotak et al., 1998). These results support a model in which changes in protein expression may significantly underlie changes in synaptic efficacy in the LSO. Interestingly, the immature inhibitory pathway also releases glutamate, which is loaded into synaptic vesicles by vesicular glutamate transporter 3 (VGLUT3) (Gillespie et al., 2005), and expression of VGLUT3 is understood to play an important role in developmental refinement of this inhibitory pathway (Noh et al., 2010).

Although developmental changes in protein expression likely alter synaptic efficacy in the immature LSO, subcellular distribution at least of inhibitory inputs occurs during circuit optimization in the auditory brainstem. In particular, the LSO's neighbouring nucleus, the medial superior olive (MSO), also receives inhibitory inputs from MNTB. In the gerbil MSO, glycine receptors are diffusely distributed along the dendrites of MSO principal cells at hearing onset and are subsequently redistributed towards the soma under the influence of acoustic experience (Kapfer et al., 2002). As low-frequency hearing specialists, gerbils depend heavily on MSO for azimuthal sound localization. It is intriguing to ask whether the LSO of a high frequency specialist such as rat also requires acoustic experience for synapse redistribution. In pre-hearing LSO, patterned spontaneous activity (Tritsch et al., 2007) is required for functional refinement of the inhibitory pathway (Clause et al., 2014). Do the immature synapses of this LSO input pathway undergo redistribution, and if so, is acoustic activity required for such refinement? This question can be tested by examining synaptic redistribution before hearing onset. Here, we labelled individual LSO principal cells, immunostained for protein markers of excitatory and inhibitory synapses, and reconstructed the labeled neurons together with their identified synaptic inputs, in order to examine whether and how excitatory and inhibitory synapses are redistributed in an early postnatal stage in the absence of acoustic activity.

4.3 Methods

4.3.1 Single-cell electroporation

All procedures were performed in accordance with Canadian Council on Animal Care guidelines and were approved by the Animal Research Ethics Board of McMaster University. The single-cell electroporation (SCE) equipment and procedure is described in Chapter 2. In brief, Sprague-Dawley rats aged at postnatal days 3/4, 10/11, and 17/18 (P3/4, P10/11, and P17/18) were anesthetized, and the brain was quickly removed and placed in ice-cold, oxygenated artificial cerebrospinal fluid (ACSF) containing NaCl, 124 mM; $MgSO_4$, 1 mM; KCl, 5 mM; KH_2PO_4, 1.25 mM; Dextrose, 10 mM; $NaCO_3$ 26 mM; $CaCl_2{\cdot}H_2O$, 2 mM; and Kynurenic acid 1 mM. Postnatal day 3/4 is associated with the onset of physiologically measurable refinement in LSO for both excitatory and inhibitory pathways (Kim and Kandler, 2003; Case et al., 2011). Postnatal day 10/11 is just prior the onset of hearing (Geal-Dor et al., 1993). For each P10/11 pup, a loud hand clap was used to test for the existence of an acoustic startle reflex. (Davis et al., 1982). As none of these pups showed a response to the clap we judged them as pre-hearing. Coronal slices (300 µm for P3/4 and P10/11 rats, and 250 µm for P17/18 rats) were cut with a vibratome. Slices containing the LSO were placed in a humidified, oxygenated interface chamber filled with ACSF at room temperature for at least 30 minutes. The recovered tissue slices were then transferred to an immersion chamber continuously perfused with oxygenated ACSF.

Micropipettes were pulled from borosilicate glass to a resistance of 10 - 20 MΩ and filled with 0.05% Alexa Fluor^{TM} 488 Hydrazide (Thermo Fisher) in 0.9% saline solution. The filled electrode was positioned above the LSO and advanced with a square-wave searching pulse while monitoring the output at the oscilloscope. The system was switched to electroporation mode once the amplitude of the monitored square wave dropped by at least 20%. Electroporation pulses consisted of -9V square pulse-pairs delivered at 1 Hz (single-pulse duration 5 ms; inter-pulse-interval 10 ms). Filled cells were visualized with epifluorescence after delivery of 10 or more pulse-pairs. If principal fusiform neurons were strongly labeled, another 5 pulse-pairs were delivered. In more highly scattering P17/18 tissue, only the soma could be visualized, and electroporation was performed completely blind. The slice was then transferred to the interface chamber for at least 10 minutes before being fixed with 4% paraformaldehyde in PBS for 20 hours at 4 °C.

4.3.2 Immunohistology

After fixation, slices were transferred to 30% sucrose in PBS for cryoprotection, and were later resectioned at 50 µm at a freezing microtome. Tissue sections were blocked for 24 hours in solution containing 5% normal serum, 2.5% bovine serum albumin (BSA), and 0.5% triton-X in PBS. Then, sections were incubated for 60 hours in a solution containing 5% normal serum, 2.5% BSA, and primary antibodies raised against gephyrin and vesicular glutamate transporter 1 (VGLUT1) in PBS. Next, sections were incubated for 24 hours in secondary antibodies diluted at 1:500 in 5% normal serum in PBS. Details of primary and secondary antibodies are listed in Table 1. Sections were washed in PBS before being mounted and coverslipped in a mounting medium (CFM-1, Citifluor Ltd.) with a high refractive index (RI) of 1.515 to minimize refractive mismatch error. Staining runs were occasionally performed with a condition in which the primary antibodies were deleted, in order to test for artifactual staining.

4.3.3 Image acquisition and analysis

Images were acquired at the confocal microscope (Leica SP5), using 488, 532, and 633 laser lines to excite Alexa 488, Cy3, and Alexa 647. A single image was acquired at low magnification to record cell's location within the LSO, and then image stacks were collected with a 63X lens (NA 1.4) using Nyquist sampling, resulting in a voxel size of 120 nm x 120nm x 335 nm. To minimize the possibility of FRET-induced photobleaching between the densely fluorophore-labeled cell and surrounding synaptic label (pers. comm. A Cooper & D Gillespie), the two synaptic labels were first imaged simultaneously throughout the stack, and the cell was subsequently imaged.

All images were converted to 8-bit tiff files in ImageJ (Abràmoff, Magalhães, and Ram, 2004). Multiple files containing image stacks of the same cell were stitched together in Image J. Images were first deconvolved in Autoquant (Media Cybernetics, Inc.), and dendrites were then traced manually with the Filament Tracer module of Imaris (Oxford Instruments). Dendritic data, including vertex position, vertex radius, and edge that connects adjacent vertices, were saved in *.mat files for further analysis in Matlab (MathWorks). The soma was segmented with Imaris and exported as a mask in the tiff file. Excitatory and inhibitory synapses, as identified from VGLUT1- and gephyrin-positive puncta, were segmented using the watershed-based, iterative thresholding algorithm described in Chapter 3. After segmentation, the centroid position and the radius of each identified synapse were imported to Imaris (using Open Object Manager) for visualization and further manipulation.

To quantify dendritic complexity we used 3D Sholl analysis. We set the center of the mass of the soma as the center of the Sholl sphere. We then increased the radius of each Sholl sphere by 5 µm and counted the number of intersections between dendrites and spheres.

To assign synapses to the reconstructed cell, for each soma mask, we dilated the mask spherically by 1 µm to capture presynaptic (VGLUT1) label and by 100 nm to capture postsynaptic (gephyrin) label. The putative synapses located inside the dilated mask were identified as somatic synapses. In the dendrites, for each putative synapse, we calculated the Euclidean distance between the centroid of the putative synapse and every vertex of the traced dendrite. If the calculated distance was below our distance threshold, the putative synapse was identified as a dendritic synapse belonging to the labeled cell. The distance threshold values for VGLUT1 and gephyrin were 1 µm + vertex radius and 100 nm + vertex radius. One potential caveat to the identification of dendritic synapses occurred with the putative synapses along the proximal dendrite. Proximal dendrites, especially for P10 and above neurons, are much thicker than distal dendrites, and our reconstruction software was unable to create a smooth model for the thick proximal dendrite. Therefore, the 1 µm and 100 nm threshold distances likely underestimated the number of synapses along the proximal dendrite. To address this issue, we imported all the putative synapses to Imaris and manually selected dendritic synapses along the proximal dendrite. We overlaid the deconvolved neuron and its putative synapses, and then retained those synapses that 'colocalized' with the neuron in this overlay.

After identifying dendritic synapses, we calculated the linear distance of each synapse from the soma along the dendrite. Here, we assigned each dendritic synapse to a dendritic vertex. First, we set the root vertex of each dendrite as the starting point of the soma. Next, we determined the linear distance between each vertex and the starting point, using a calculation based on Dijkstra's algorithm (Dijkstra, 1959). We assigned each edge between two vertices a weight of one. Dijkstra's algorithm labels the distance from the starting point to all other vertices as infinity and marks these vertices unvisited. Note that the distance from the starting point to the starting point is zero. Dijkstra's algorithm then iteratively visits the nearest unvisited vertex and calculates the current distance by summing all the weighted edges that connect the starting point to the currently visited vertex. If the current distance is less than the previous distance, all the visited vertices are added to a queue that represents the shortest path from the starting point to the current vertex. The algorithm iterates until all vertices have been visited. All vertices are visited exactly once, and no vertices are revisited. We used the shortest path to assign the linear distance from the starting point to each vertex, and labeled each vertex and its corresponding synapse with this linear distance from the starting point. We used the linear distance to quantify synapse density along the dendrite, synapse clustering along the dendrite, and nearest-neighbor relationships among synapses.

4.4 Results

We labeled and reconstructed fusiform cells in LSO and segmented their excitatory and inhibitory synapses in 3D for three age groups. As the number of cells in the oldest age group was relatively small, analyses of dendritic complexity and synapse position for P17/18 are omitted here.

4.4.1 Dendritic complexity decreases

We quantified the dendritic complexity of principal fusiform cells in LSO (N = 12, 13, 2 for P3/4, P10/11, and P17/18), using a 3D Sholl analysis, expanding the spheres in 5 µm increments in radius. The somata of P10/11 cells were, on average, larger than those of P3/4 cells (Fig. 1). Within 80 µm of the soma centroid, the average number of Sholl intersections decreased between P3/4 and P10/11 (Fig. 1), a reduction also illustrated in the fractional change plot (Fig. 2).

Cellular morphology underwent a dramatic simplification between P3/4 and P10/11: within the first 20 µm from the soma centre, the number of Sholl intersections decreased by nearly 50%. Between 20 – 80 µm from the centre of the soma, the number of Sholl intersections decreased by 25%. Complexity of more distal dendrites, beyond 80 µm from the soma centre, remained largely unchanged (Figs. 1, 2).

4.4.2 Gephyrin-positive synapses are redistributed toward the soma in the week before hearing onset

We immunostained for gephyrin as a marker of inhibitory synapses. In neonates (P3/4) gephyrin was distributed apparently randomly, whereas at P11 and P18, gephyrin clustered around the soma and the proximal dendrite (Fig. 3). Between P4 and P11, the number of gephyrin-positive synapses at the soma increased by 100% (P4: 68.33 ± 6.44, n = 12 VS P11: 139.3 ± 18.63, n = 13, p = 9.99e-04, Wilcoxon rank-sum test). Between P4 and P11, despite an increase in soma surface of over 20%, the surface density of gephyrin-positive synapses increased by 166% (Fig. 4; P4: 0.13 ± 0.02 puncta/µm^2, n = 12 VS P11: 0.21 ± 0.03 puncta/µm^2, n=13, p = 0.024, Wilcoxon rank-sum test), indicating an absolute addition of synapses at the soma. Somatic gephyrin-positive synapses increased not only in number and density, but also in size (Fig. 5; P4 median = 0.2 µm^3; 25th percentile 0.16 µm^3; 75th percentile 0.37 µm^3; n = 623 and P11 median = 0.5 µm^3, 25th percentile 0.25 µm^3; 75th percentile 0.61 µm^3; n = 975, p = 3.673e-37, Wilcoxon rank-sum test).

We further examined the distribution and volume of gephyrin-positive synapses along dendrites (Fig. 6). In P4 tissue, although almost 50% of the gephyrin puncta fell within 50 µm of the soma, the distribution of these synapses was apparently random and did not appear to cluster in specific locations. About 75% of these synapses were smaller than 0.3 μm^3. Within the subsequent week, 50% of the gephyrin puncta became more constrained, occupying the proximal 20 µm of dendrite, and these synapses grew in volume (P4 median = 0.24 μm^3; 25th percentile 0.14 μm^3; 75th percentile 0.36 μm^3; n = 2112 and P11 median = 0.36 μm^3, 25th percentile 0.24 μm^3; 75th percentile 0.47 μm^3; n = 1713, p = 0, Wilcoxon rank-sum test). Taken together, the cumulative distribution of gephyrin showed that inhibitory synapses were redistributed towards the soma (Fig. 7; whereas the proximal 40 µm of dendrite contained 80% of the gephyrin puncta at P4, by P11, the proximal 20 µm of dendrite accounted for 80% of the gephyrin-positive puncta).

4.4.3 VGLUT1-positive synapses are redistributed away from the soma in the week before hearing onset

We immunostained for VGLUT1 as a marker for excitatory synapses. In contrast to inhibitory synapses, VGLUT1-positive synapses initially clustered thickly around the soma, becoming sparser in the ensuing week (Fig. 8). Between P4 and P11, the number of VGLUT1 at soma decreased by 50% (P4: 107.8 ± 14.52, n = 12 VS P11: 53.38 ± 4.52, n = 13, p = 0.012, Wilcoxon rank-sum test). Between P4 and P11, the density of VGLUT1 at the soma decreased by 246% (Fig. 9; P4: 0.19 ± 0.03, n = 12 *vs* P11: 0.08 ± 0.01, n=13, p = 9.99e-04, Wilcoxon rank-sum test). The VGLUT1 puncta remaining at the soma increased in volume (Fig. 10, P4: 0.42 ± 0.33 n = 822 VS P11: 0.48 ± 0.32 n = 412; p = 1.37e-06, Wilcoxon rank-sum test 2).

Excitatory synapses were also redistributed along the dendrites. At P4, 60% of the dendritic VGLUT1 puncta were found within the proximal 40 µm. The overall number of dendritic VGLUT1-positive synapses decreased, such that by P11, 60% of the dendritic VGLUT1 puncta extended to 60 µm from the soma. As did somatic synapses, dendritic excitatory synapses grew in size (Fig. 11; P4 median = 0.29 μm^3; 25th percentile 0.18 μm^3; 75th percentile 0.39 μm^3; n = 2588 and P11 median = 0.34 μm^3, 25th percentile 0.248 μm^3; 75th percentile 0.40 μm^3; n = 1387, p = 1.40e-40, Wilcoxon rank-sum test). Taken together, the cumulative distribution of VGLUT1 showed that excitatory synapses, which were common at the soma and proximal dendrite in the neonate, were removed in the week before hearing onset (Fig. 12; 80% of the VGLUT1 puncta were located within the proximal 30 µm of dendrite for P4 neurons and proximal 50 µm of dendrite for P11 neurons).

4.4.4 Complementary changes in excitatory and inhibitory synapses

We observed significant redistribution of excitatory and inhibitory synapses during the week before hearing onset. In the neonate, excitatory synapses outnumbered inhibitory synapses at the soma by nearly a factor of 2 (VGLUT1: 107.8 ± 14.52, n = 12 VS gephyrin: 68.33 ± 6.44, n = 12, p = 0.02, Wilcoxon rank-sum test). By P11 – due to the elimination of excitatory synapses at the soma and the redistribution of inhibitory synapses toward the soma – this proportion was reversed, and inhibitory synapses outnumbered excitatory synapses at the soma by more than a factor of 2 (VGLUT1: 53.38 ± 4.52, n = 13 VS gephyrin: 139.3 ± 18.63, n = 13, p = 5.06e-05, Wilcoxon rank-sum test). Similar complementary changes were seen in the dendrites, where gephyrin density in the first 10-µm segment increased dramatically, but decreased beyond 20 µm; at the same time, VGLUT1 density in the first 30-µm segment decreased by about 50% and increased slightly beyond 80 µm (Fig. 13).

4.4.5 Nearest-neighbour relationships among excitatory and inhibitory synapses

A motivating question for this work centers on the co-registration of excitatory and inhibitory inputs to the LSO neurons and on whether synapses might engage in direct uni- or bi-directional signaling. In light of the possibility of reciprocal signaling through glutamate spillover (Alamilla and Gillespie, 2011), we examined nearest-neighbour relationships among synapses of same and different phenotype. We first delineated10-µm segments along the dendrites, assigning somatic synapses to 0 µm from the soma. For each dendrite segment (soma at 0 µm), we randomly selected 5 synapses as seeds, or ‘source synapses.’ If the number of synapses was less than 5 for a given segment, all the synapses on this segment were used as source synapses. For each source synapse, we then found the linear distances, along the dendrite, from the source synapse to the nearest 50 synapses of the same phenotype and of the opposite phenotype. In all cases, these calculations were performed along the same primary dendrite, thus excluding any cross-soma distances. Figures 14-21 show these relationships, with the distances to the nearest 50 synapses binned into 10-µm segments (Figs. 14 -21). Note that the soma is treated as a point so that the distance from a somatic synapse to another somatic synapse is 0 and the distance from one dendritic synapse to any somatic synapse is the same as the distance from that dendritic synapse to any other somatic synapse. Using this approach shows a strong bias in distance counts towards the soma. Regardless, these nearest-neighbour counts show initial clustering of both excitatory and inhibitory synapses near the soma, with a shift toward the soma among inhibitory synapses, and a shift away from the soma among excitatory synapses.

To examine more closely the potential for interactions between individual synapses, we found the single-nearest-neighbor (1NN) distances along dendrites at P4 and P11 (excluding somatic synapses from this calculation). Regardless of phenotype, the 1NN distance decreased between P4 and P11. The inhibitory-inhibitory 1NN distance decreased by 50% (P4: 1.56 µm ± 0.05 µm, n = 2112 VS P11: 0.78 µm ± 0.03 µm, n = 1713; p = 2.40e-63, Wilcoxon rank-sum test) and the excitatory-excitatory 1NN distance decreased by 30% (P4: 1.33 µm ± 0.03 µm, n = 2588 VS P11: 0.99 µm, ± 0.03 µm, n = 1387; p = 6.02e-15, Wilcoxon rank-sum test). The excitatory-inhibitory 1NN distance (starting from excitatory puncta), and the inhibitory-excitatory 1NN distance also both decreased, the first by about 30% (P4: 1.40 µm ± 0.05 µm, n = 2588 VS P11: 1.02 µm ± 0.05 µm, n = 1387; p = 4.32e-04, Wilcoxon rank-sum test), and the second by 15% (P4: 0.90 µm ± 0.04 µm, n = 2112 VS P11: 0.74 µm ± 0.02 µm, n = 1713; p = 4.20e-05, Wilcoxon rank-sum test). Already at P4, dendritic synapses were more likely to be found near synapses of the same than different type (Figs. 22, 24), as indicated by the positive y-intercept and slope <1. This tendency was further enhanced at P11, showing a developmental increase in preferential clustering with synapses of the same phenotype.

4.5 Discussion

Here, we sought to better understand how refinement of synapse position contributes to developmental optimization of the LSO circuit. To do so, we characterized changes in cell morphology, as well as in location and volume of excitatory and inhibitory synapses onto LSO cells, in the week before hearing onset, a period known to be characterized by numerous physiologically measurable changes (Kim and Kandler, 2003, 2010; Gillespie et al., 2005; Case and Gillespie, 2011).

The LSO cells in our sample exhibited a dramatic decrease in complexity before hearing onset, as previously reported (Rietzel and Friauf, 1998). During this period, inhibitory synapses also increased – while excitatory synapses decreased – in number and density at the soma. In general, the distribution of inhibitory dendritic synapses shifted toward the soma, while the distribution of excitatory dendritic synapses shifted away from the soma, in the week before hearing onset. It is common throughout the central nervous system for inhibitory synapses to be restricted to a specific subcellular compartment of the postsynaptic cell (Iwakura et al., 2012; Jiang et al., 2013; Kubota et al., 2015; Gamlin et al., 2020), and this cellular compartment-specific targeting of inhibitory synapses has been shown to be established and refined during postnatal development (Kapfer et al., 2002; Luján et al., 2008; Cioni et al., 2013; Bleckert et al., 2018).

This is not the first study to examine development of glycinergic synapses in the developing LSO, but it is the first to examine development of inhibitory synapses in an unbiased manner. Before it was well understood that GABAergic transmission is common – and indeed more prevalent than glycinergic transmission – in the immature MNTB-LSO pathway (Kotak et al., 1998; Nabekura et al., 2004), glycine receptor staining showed that an apparently random distribution of glycinergic at P4 became perisomatic after hearing onset (Friauf et al., 1997). Although the biological function of early GABAergic transmission at glycinergic synapses is still unknown, one model suggests that GABAergic synapses may be more amenable than glycinergic synapses to developmental refinement. In this model, GABAergic transmission is used to perform refinement at immature synapses, instantiated perhaps in expression of the scaffolding protein gephyrin, and then glycine receptors are substituted in for GABA_A receptors at previously fine-tuned synapses. To find all inhibitory synapses, we took advantage of the fact that gephyrin clusters both glycine receptors and GABA_A receptors at the membrane (Kirsch et al., 1993; Sassoè-Pognetto et al., 1995; Essrich et al., 1998) and is broadly associated with ionotropic inhibitory synapses. Using this more inclusive measure of inhibitory synapses, we found that already at P4 inhibitory synapses are distributed non-randomly, being skewed toward the soma and proximal dendrite. Although elimination of somatic excitatory synapses has been reported after hearing onset (Blaesse et al., 2005), we found that a substantial amount of excitatory synapse pruning occurred before hearing onset, due in part to the surprising abundance of excitatory synapses at the soma and proximal dendrite neonatally; many of these perisomatic excitatory synapses disappeared by P11.

In mature cerebral cortex, excitatory synapses are found throughout the dendritic field, though they are outnumbered by inhibitory synapses at the soma and proximal dendrite (Megiâs et al., 2001; Santuy et al., 2018; Iascone et al., 2020). In mature LSO as well, inhibitory synapses outnumber excitatory synapses at the soma and proximal dendrite (Cant, 1984; Helfert and Schwartz, 1986; Helfert et al., 1992; Brunso-Bechtold et al., 1994; Gjoni et al., 2018). Our approach allows us to reconstruct individual cells together with their synapses to ask how synapse position changes before hearing onset. We found that in neonates excitatory synapses outnumbered inhibitory synapses 2 to 1 at the soma, and 1.3 to 1 along the proximal dendrite. By hearing onset, this excitatory-inhibitory synapse ratio was inverted, registering 1:3 at the soma and 1:2 along the proximal dendrite. Developmental optimization of the ratio of excitatory to inhibitory synapses has also been studied is the retina, where, in contrast to the LSO principal cells studied here, retinal ganglion cells maintain their excitatory-inhibitory synapse ratio within individual dendritic compartments during early postnatal development (Soto et al., 2011b; Bleckert et al., 2013), and the amplitudes and kinetics of miniature excitatory and inhibitory postsynaptic potentials are balanced through postnatal development in retinal ganglion cells (Tian and Copenhagen, 2001). By contrast, in the LSO, though latencies for both excitatory and inhibitory postsynaptic potentials decrease, those of inhibitory postsynaptic potentials show a larger decrement (Kandler and Friauf, 1995), a finding consistent with the complementary redistribution of excitatory and inhibitory synapses reported here.

Experience-dependent mechanisms have been implicated in specifying synapse position onto individual cells elsewhere in the auditory brainstem. In the neighbouring MSO, a nucleus with the same origin, inhibitory synapses have been shown to be redistributed toward the soma and the proximal dendrite after hearing onset (Kapfer et al., 2002). [Note, however, that as those measurements were performed after hearing onset, they are not directly comparable to the data reported here.] Associated with this synapse redistribution, axonal arbourizations of MNTB cells narrow within the MSO, and a larger proportion of axonal arbours come to terminate in the somatic region of MSO cells (Werthat et al., 2008). Furthermore, altered acoustic experience disrupts both the redistribution of inhibitory synapses and the pruning of MNTB axonal arbours within the MSO (Kapfer et al., 2002; Werthat et al., 2008), supporting a role for acoustic experience in directing synapse position. Together, these studies suggest that acoustic experience drives selective pruning of axonal branches innervating distal dendrites, and causes the inhibitory synapse distribution to shift soma-ward, in the MSO.

Studies in the peripheral and central nervous systems show newer, less stable synapses being deleted through axon retraction (Rich and Lichtman, 1989; Balice-Gordon and Lichtman, 1990, 1993; Haas et al., 2006; Ruthazer et al., 2006). In the optic tectum, visual experience can enhance the stability of new synapses and induce the retraction of retinal ganglion cell axon (Haas et al., 2006; Ruthazer et al., 2006).

Translating to the LSO, a mechanism of synapse deletion through axon retraction could easily explain the developmental redistribution of excitatory synapses. The increase in inhibitory synapse density at the soma and proximal dendrite cannot however be attributed to axonal pruning, and these results therefore point to separate mechanisms for synapse redistribution of excitatory and inhibitory inputs.

The developmental redistribution of inhibitory synapses must involve a mechanism distinct from that used for redistribution of excitatory synapses, and may require multiple mechanisms. Whereas elimination of synapses on distal dendrites can be explained through axon retraction, redistribution onto the soma and proximal dendrite requires either that existing synapses be moved or that that new synapses be established and stabilized. Possibly, MNTB axons explore the space, extending and retracting branches (Portera-Cailliau et al., 2005; Steinecke et al., 2017), and forming new synapses that are strengthened through neural activity (Wu and Cline, 1998; Sin et al., 2002). Alternatively, synapses from more distal dendrite could be drawn toward the soma. Transmembrane proteins can diffuse randomly within the lipid bilayer (Kusumi et al., 1993; Sako and Kusumi, 1994), and lateral diffusion of individual receptors has been directly observed at both excitatory and inhibitory synapses (Meier et al., 2001; Borgdorff and Choquet, 2002; Tovar and Westbrook, 2002; Dahan et al., 2003; Meissner and Häberlein, 2003; Tardin et al., 2003; Thomas et al., 2005). In the absence of gephyrin, inhibitory receptors perform a random walk in the membrane; gephyrin however acts as a trap for freely diffusing glycine and $\mathrm{GABA_A}$ receptors, alternately trapping them between mobile and confined states and preventing their free diffusion within the membrane (Meier et al., 2001; Mukherjee et al., 2011; Masson et al., 2014). Results from cultured hippocampal neurons show vesicular inhibitory amino acid transporter (VIAAT), a presynaptic protein at inhibitory synapses, and gephyrin diffusing roughly simultaneously, with accumulation of VIAAT preceding that of gephyrin (Dobie and Craig, 2011). One speculation might therefore be that the leading cause of synapse redistribution is not receptor diffusion but rather the addition before hearing onset of new axon branches of VIAAT-expressing MNTB terminals near somatic sites of LSO principal cells, leading to translocation of inhibitory synapses toward the soma.

Estimates of synaptic strength from protein label are necessarily indirect, and yet it is generally accepted that the volume of synaptic protein label correlates with synaptic strength. Inhibitory synaptic currents in particular have been shown to correlate with gephyrin cluster size in both AVCN bushy cells and Renshaw cells (Lim et al., 1999; Oleskevich et al., 1999; Gonzalez-Forero et al., 2005). We found, in the pre-hearing LSO, that median synaptic volume increased for both excitatory and inhibitory synapses. Assuming the same packing density of glutamate in vesicles, the increased VGLUT1 cluster volume indicates increased size of excitatory synapses. Our showing increases in synapse cluster volume for both excitatory and inhibitory synapses are consistent with physiological results showing increases in mean synaptic strength for both phenotypes (Kim and Kandler, 2003; Case et al., 2011). However, the strengthen in synaptic inputs may not be due to the shift of synapse location along dendrite (Kim and Kandler, 2010). In acute living slice recording from mice, the average rise time of single-fiber PSC in P10-P12 animals is half as much as in P1-3 animals, suggesting the inhibitory synapses shift proximally. The independence of rise time and amplitude of individual PSC suggests that the increase in synaptic strength is not dependent on the position of the synapses.

Our study confirms that LSO neurons undergo significant structural refinement, which includes the spatial specification of their synaptic inputs, during a postnatal period in which acoustic experience is absent. During this period, the developing cochlea contains a cluster of columnar-shaped inner supporting cells that form a transient structure known as Kölliker's organ, located just medial to the IHCs (Hinojosa, 1977). Cells of Kölliker's organ spontaneously release ATP, activating purinergic receptors in nearby inner hair cells (IHCs). The depolarized IHCs release glutamate, triggering bursts of action potentials in auditory nerve fibres. This spontaneous activity in the cochlea begins a few days after birth (~P3) and ceases after hearing onset (Tritsch and Bergles, 2010). The patterned spontaneous activity in the immature cochlea is understood to guide physiologically measurable refinement in the LSO (Tritsch et al., 2007; Clause et al., 2014; Müller et al., 2019), and such activity may be permissive or instructive for the synapse redistribution shown here. As the number of synaptic boutons formed by MNTB axons within the LSO is reduced within the week after hearing onset (Sanes and Siverls, 1991), it is possible that further redistribution of synaptic inputs occurs in the presence of acoustic experience. Determining whether activity plays any role in localizing synapses before or after hearing onset will be of interest.

One motivation for examining relationships between nearby synapses was to better understand how the local geometry could contribute to interactions between synapses of different phenotype, which might in turn mediate tonotopic registration of the phenotypically distinct pathways. In mature LSO, the excitatory and inhibitory inputs must carry signals about precisely matched stimulus frequencies (Tollin, 2003). How the two phenotypically different inputs come to achieve registration onto individual neurons reflects a fundamental question in developmental neuroscience. The excitatory and inhibitory inputs to LSO are crudely aligned already at birth (Sanes and Siverls, 1991; Kandler and Friauf, 1993; Kil et al., 1995), and each input pathway undergoes further refinement before hearing onset. Interestingly, bushy cells in AVCN receive commissural connections from contralateral cochlear nucleus (Babalian et al., 2002). During the period before hearing onset, the commissural connections between the two cochlear nuclei could potentially provide synchronization to the patterned spontaneous activity arisen from the developing cochlea. This potentially synchronized spontaneous activity may lead to the initial crude alignment of the two inputs. Our results cannot directly address the issue of alignment, however, provide critical information on the synapse location along individual neurons. At least some close apposition of excitatory and inhibitory synapses was presupposed, given evidence for bidirectional glutamate spillover occurs between synapses of the excitatory and inhibitory input pathways to the LSO in the first postnatal week (Alamilla and Gillespie, 2011). In the spillover study, the authors proposed that slightly longer and more variable rise times for glutamate-mediated events in the inhibitory pathway might be explained by a longer diffusion path from release site to receptors under the inhibitory pathway. They however made this suggestion under the explicit assumption that the relative distributions of excitatory and inhibitory synapses in their young slices conformed to known adult distributions, and therefore that they could rule out a contribution of clamping artifact to apparent differences in latency. Our current data invalidate this assumption, raising the possibility that the observed latency differences were artifactual and the proposed differences in diffusion path nonexistent. Our data showing close apposition of excitatory and inhibitory synapses at the somata of neonatal LSO, however, especially in conjunction with presumed immature expression of glutamate transporters, are consistent with substantial glutamate spillover at early ages.

4.6 References

Abràmoff MD, Magalhães PJ, Ram SJ (2004) Image processing with imageJ. Biophotonics Int 11:36–41.

Alamilla J, Gillespie DC (2011a) Glutamatergic inputs and glutamate-releasing immature inhibitory inputs activate a shared postsynaptic receptor population in lateral superior olive. Neuroscience 196:285–296.

Alamilla J, Gillespie DC (2011b) Glutamatergic inputs and glutamate-releasing immature inhibitory inputs activate a shared postsynaptic receptor population in lateral superior olive. Neuroscience 196:285–296.

Balice-Gordon RJ, Lichtman JW (1990) In vivo visualization of the growth of pre- and postsynaptic elements of neuromuscuolar junctions in the mouse. J Neurosci 10:894–908.

Balice-Gordon RJ, Lichtman JW (1993) In vivo observations of pre- and postsynaptic changes during the transition from multiple to single innervation at developing neuromuscular junctions. J Neurosci 13:834–855.

Bernander O, Koch C, Douglas RJ (1994) Amplification and linearization of distal synaptic input to cortical pyramidal cells. J Neurophysiol 72:2743–2753.

Blaesse P, Ehrhardt S, Friauf E, Nothwang HG (2005) Developmental pattern of three vesicular glutamate transporters in the rat superior olivary complex. Cell Tissue Res 320:33–50.

Bleckert A, Parker ED, Kang YH, Pancaroglu R, Soto F, Lewis R, Craig AM, Wong ROL (2013) Spatial Relationships between GABAergic and Glutamatergic Synapses on the Dendrites of Distinct Types of Mouse Retinal Ganglion Cells across Development. PLoS One 8.

Bleckert A, Zhang C, Turner MH, Koren D, Berson DM, Park SJH, Demb JB, Rieke F, Wei W, Wong RO (2018) GABA release selectively regulates synapse development at distinct inputs on direction-selective retinal ganglion cells. Proc Natl Acad Sci U S A 115:E12083–E12090.

Bledsoe SC, Snead CR, Helfert RH, Prasad V, Wenthold RJ, Altschuler RA (1990) Immunocytochemical and lesion studies support the hypothesis that the projection from the medial nucleus of the trapezoid body to the lateral superior olive is glycinergic. Brain Res 517:189–194.

Borgdorff AJ, Choquet D (2002) Regulation of AMPA receptor lateral movements. Nature 417:649–653.

Boudreau JC, Tsuchitani C (1968) Binaural interaction in the cat superior olive S segment. J Neurophysiol 31:442–454.

Brunso-Bechtold JK, Linville MC, Henkel CK (1994) Terminal types on ipsilaterally and contralaterally projecting lateral superior olive cells. Hear Res 77:99–104.

Caicedo A, Eybalin M (1999) Glutamate receptor phenotypes in the auditory brainstem and mid-brain of the developing rat. Eur J Neurosci 11:51–74.

Cant NB (1984) The fine structure of the lateral superior olivary nucleus of the cat. J Comp Neurol 227:63–77.

Cant NB, Casseday JH (1986) Projections from the anteroventral cochlear nucleus to the lateral and medial superior olivary nuclei. J Comp Neurol 247:457–476.

Case DT, Gillespie DC (2011) Pre- and postsynaptic properties of glutamatergic transmission in the immature inhibitory MNTB-LSO pathway. J Neurophysiol 106:2570–2579.

Case DT, Zhao X, Gillespie DC (2011) Functional refinement in the projection from ventral cochlear nucleus to lateral superior olive precedes hearing onset in rat. PLoS One 6.

Cioni JM, Telley L, Saywell V, Cadilhac C, Jourdan C, Huber AB, Huang JZ, Jahannault-Talignani C, Ango F (2013) SEMA3A signaling controls layer-specific interneuron branching in the cerebellum. Curr Biol 23:850–861.

Clause A, Kim G, Sonntag M, Weisz CJC, Vetter DE, Rubsamen R, Kandler K (2014) The Precise Temporal Pattern of Prehearing Spontaneous Activity Is Necessary for Tonotopic Map Refinement. Neuron 82:822–835.

Dahan M, Lévi S, Luccardini C, Rostaing P, Riveau B, Triller A (2003) Diffusion Dynamics of Glycine Receptors Revealed by Single-Quantum Dot Tracking. Science (80-) 302:442–445.

Dijkstra EW (1959) A note on two problems in connexion with graphs. Numer Math 1.

Dobie FA, Craig AM (2011) Inhibitory synapse dynamics: Coordinated presynaptic and postsynaptic mobility and the major contribution of recycled vesicles to new synapse formation. J Neurosci 31:10481–10493.

Druckmann S, Feng L, Lee B, Yook C, Zhao T, Magee JC, Kim J (2014) Structured Synaptic Connectivity between Hippocampal Regions. Neuron 81:629–640.

Essrich C, Lorez M, Benson JA, Fritschy JM, Lüscher B (1998) Postsynaptic clustering of major GABAA receptor subtypes requires the γ2 subunit and gephyrin. Nat Neurosci 1:563–571.

Friauf E, Hammerschmidt B, Kirsch J (1997) Development of adult-type inhibitory glycine receptors in the central auditory system of rats. J Comp Neurol 385:117–134.

Gamlin CR, Zhang C, Dyer MA, Wong ROL (2020) Distinct Developmental Mechanisms Act Independently to Shape Biased Synaptic Divergence from an Inhibitory Neuron. Curr Biol 30:1258-1268.e2.

Ganguly K, Schinder AF, Wong ST, Poo M ming (2001) GABA itself promotes the developmental switch of neuronal GABAergic responses from excitation to inhibition. Cell 105:521–532.

Gillespie DC, Kim G, Kandler K (2005) Inhibitory sypnapses in the developing auditory system are glutamatergic. Nat Neurosci 8:332–338.

Gjoni E, Aguet C, Sahlender DA, Knott G, Schneggenburger R (2018) Ultrastructural basis of strong unitary inhibition in a binaural neuron. J Physiol 596:4969–4982.

Gonzalez-Forero D, Pastor AM, Geiman EJ, Benítez-Temiño B, Alvarez FJ (2005) Regulation of gephyrin cluster size and inhibitory synaptic currents on renshaw cells by motor axon excitatory inputs. J Neurosci 25:417–429.

Haas K, Li J, Cline HT (2006) AMPA receptors regulate experience-dependent dendritic arbor growth in vivo. Proc Natl Acad Sci U S A 103:12127–12131.

Helfert RH, Juiz JM, Bledsoe SC, Bonneau JM, Wenthold RJ, Altschuler RA (1992) Patterns of glutamate, glycine, and GABA immunolabeling in four synaptic terminal classes in the lateral superior olive of the guinea pig. J Comp Neurol 323:305–325.

Helfert RH, Schwartz IR (1986) Morphological evidence for the existence of multiple neuronal classes in the cat lateral superior olivary nucleus. J Comp Neurol 244:533–549.

Iascone DM, Li Y, Sümbül U, Doron M, Chen H, Andreu V, Goudy F, Blockus H, Abbott LF, Segev I, Peng H, Polleux F (2020) Whole-Neuron Synaptic Mapping Reveals Spatially Precise Excitatory/Inhibitory Balance Limiting Dendritic and Somatic Spiking. Neuron 106:566-578.e8.

Iwakura A, Uchigashima M, Miyazaki T, Yamasaki M, Watanabe M (2012) Lack of molecular-anatomical evidence for GABAergic influence on axon initial segment of cerebellar Purkinje cells by the pinceau formation. J Neurosci 32:9438–9448.

Jiang X, Wang G, Lee AJ, Stornetta RL, Zhu JJ (2013) The organization of two new cortical interneuronal circuits. Nat Neurosci 16:210–218.

Kandler K, Friauf E (1993) Pre- and postnatal development of efferent connections of the cochlear nucleus in the rat. J Comp Neurol 328:161–184.

Kandler K, Friauf E (1995) Development Transmission of Glycinergic and Glutamatergic Synaptic in the Auditory Brainstem of Perinatal Rats. J Neurosci 15:6890–6904.

Kapfer C, Seidl AH, Schweizer H, Grothe B (2002) Experience-dependent refinement of inhibitory inputs to auditory coincidence-detector neurons. Nat Neurosci 5:247–253.

Kil J, Hkageyama G, Semple MN, Kitzes LM (1995) Development of ventral cochlear nucleus projections to the superior olivary complex in gerbil. J Comp Neurol 353:317–340.

Kim G, Kandler K (2003) Elimination and strengthening of glycinergic/GABAergic connections during tonotopic map formation. Nat Neurosci 6:282–290.

Kim G, Kandler K (2010) Synaptic changes underlying the strengthening of GABA/ glycinergic connections in the developing lateral superior olive. Neuroscience 171:924–933.

Kirsch J, Wolters I, Triller A, Betz H (1993) Gephyrin antisense oligonucleotides prevent glycine receptor clustering in spinal neurons. Nature 366:745–748.

Kleindienst T, Winnubst J, Roth-Alpermann C, Bonhoeffer T, Lohmann C (2011) Activity-dependent clustering of functional synaptic inputs on developing hippocampal dendrites. Neuron 72:1012–1024.

Kotak VC, Korada S, Schwartz IR, Sanes DH (1998) A developmental shift from GABAergic to glycinergic transmission in the central auditory system. J Neurosci 18:4646–4655.

Kubota Y, Kondo S, Nomura M, Hatada S, Yamaguchi N, Mohamed AA, Karube F, Lübke J, Kawaguchi Y (2015) Functional effects of distinct innervation styles of pyramidal cells by fast spiking cortical interneurons. Elife 4:1–27.

Kusumi A, Sako Y, Yamamoto M (1993) Confined lateral diffusion of membrane receptors as studied by single particle tracking (nanovid microscopy). Effects of calcium-induced differentiation in cultured epithelial cells. Biophys J 65:2021–2040.

Lee KFH, Soares C, Thivierge JP, Béïque JC (2016) Correlated Synaptic Inputs Drive Dendritic Calcium Amplification and Cooperative Plasticity during Clustered Synapse Development. Neuron 89:784–799.

Lim R, Alvarez FJ, Walmsley B (1999) Quantal size is correlated with receptor cluster area at glycinergic synapses in the rat brainstem. J Physiol 516:505–512.

Luján R, de Cabo C, Juiz JM (2008) Inhibitory synaptogenesis in the rat anteroventral cochlear nucleus. Neuroscience 154:315–328.

Masson JB, Dionne P, Salvatico C, Renner M, Specht CG, Triller A, Dahan M (2014) Mapping the energy and diffusion landscapes of membrane proteins at the cell surface using high-density single-molecule imaging and bayesian inference: Application to the multiscale dynamics of glycine receptors in the neuronal membrane. Biophys J 106:74–83.

Megiâs M, Emri Z, Freund TF, Gulyâs AI (2001) TOTAL NUMBER AND DISTRIBUTION OF INHIBITORY AND EXCITATORY SYNAPSES SYNAPSES ON HIPPOCAMPAL CA1 PYRAMIDAL CELLS. Neuroscience 102:527–540.

Meier J, Vannier C, Sergé A, Triller A, Choquet D (2001) Fast and reversible trapping of surface glycine receptors by gephyrin. Nat Neurosci 4:253–260.

Meissner O, Häberlein H (2003) Lateral mobility and specific binding to GABAA receptors on hippocampal neurons monitored by fluorescence correlation spectroscopy. Biochemistry 42:1667–1672.

Moore MJ, Caspary DM (1983) Strychnine blocks binaural inhibition in lateral superior olivary neurons. J Neurosci 3:237–242.

Morgan JL, Schubert T, Wong ROL (2008) Developmental patterning of glutamatergic synapses onto retinal ganglion cells. Neural Dev 3:0–18.

Mukherjee J, Kretschmannova K, Gouzer G, Maric HM, Ramsden S, Tretter V, Harvey K, Davies PA, Triller A, Schindelin H, Moss SJ (2011) The residence time of GABA ARs at inhibitory synapses is determined by direct binding of the receptor α1 subunit to gephyrin. J Neurosci 31:14677–14687.

Nabekura J, Katsurabayashi S, Kakazu Y, Shibata S, Matsubara A, Jinno S, Mizoguchi Y, Sasaki A, Ishibashi H (2004) Developmental switch from GABA to glycine release in single central synaptic terminals. Nat Neurosci 7:17–23.

Noh J, Seal RP, Garver JA, Edwards RH, Kandler K (2010) Glutamate co-release at GABA/glycinergic synapses is crucial for the refinement of an inhibitory map. Nat Neurosci 13:232–238.

Oleskevich S, Alvarez FJ, Walmsley B (1999) Glycinergic miniature synaptic currents and receptor cluster sizes differ between spinal cord interneurons. J Neurophysiol 82:312–319.

Portera-Cailliau C, Weimer RM, De Paola V, Caroni P, Svoboda K (2005) Diverse modes of axon elaboration in the developing neocortex. PLoS Biol 3.

Rall W, Rinzel J (1973) Branch Input Resistance and Steady Attenuation for Input to One Branch of a Dendritic Neuron Model. Biophys J 13:648–688.

Rich MM, Lichtman JW (1989) In vivo visualization of pre- and postsynaptic changes during synapse elimination in reinnervated mouse muscle. J Neurosci 9:1781–1805.

Rietzel HJ, Friauf E (1998) Neuron types in the rat lateral superior olive and developmental changes in the complexity of their dendritic arbors. J Comp Neurol 390:20–40.

Rivera C, Voipio J, Payne JA, Ruusuvuori E, Lahtinen H, Lamsa K, Pirvola U, Saarma M, Kaila K (1999) The K+/Cl- co-transporter KCC2 renders GABA hyperpolarizing during neuronal maturation. Nature 397:251–255.

Ruthazer ES, Li J, Cline HT (2006) Stabilization of axon branch dynamics by synaptic maturation. J Neurosci 26:3594–3603.

Sako Y, Kusumi A (1994) Compartmentalized structure of the plasma membrane for receptor movements as revealed by a nanometer-level motion analysis. J Cell Biol 125:1251–1264.

Sanes DH, Siverls V (1991) Development and specificity of inhibitory terminal arborizations in the central nervous system. J Neurobiol 22:837–854.

Santuy A, Rodriguez JR, DeFelipe J, Merchan-Perez A (2018) Volume electron microscopy of the distribution of synapses in the neuropil of the juvenile rat somatosensory cortex. Brain Struct Funct 223:77–90.

Sassoè-Pognetto M, Kirsch J, Grünert U, Greferath U, Fritschy JM, Möhler H, Betz H, Wässle H (1995) Colocalization of gephyrin and GABAA-receptor subunits in the rat retina. J Comp Neurol 357:1–14.

Schubert T, Hoon M, Euler T, Lukasiewicz PD, Wong ROL (2013) Developmental regulation and activity-dependent maintenance of GABAergic presynaptic inhibition onto rod bipolar cell axonal terminals. Neuron 78:124–137.

Sin WC, Haas K, Ruthazer ES, Cline HT (2002) Dendrite growth increased by visual activity requires NMDA receptor and Rho GTPases. Nature 419:475–480.

Smith PH, Joris PX, Yin TCT (1998) Anatomy and physiology of principal cells of the medial nucleus of the trapezoid body (MNTB) of the cat. J Neurophysiol 79:3127–3142.

Sommer I, Lingenhöhl K, Friauf E (1993) Principal cells of the rat medial nucleus of the trapezoid body: an intracellular in vivo study of their physiology and morphology. Exp Brain Res 95:223–239.

Soto F, Bleckert A, Lewis R, Kang Y, Kerschensteiner D, Craig AM, Wong ROL (2011a) Coordinated increase in inhibitory and excitatory synapses onto retinal ganglion cells during development. Neural Dev 6:31.

Soto F, Bleckert A, Lewis R, Kang Y, Kerschensteiner D, Craig AM, Wong ROL (2011b) Coordinated increase in inhibitory and excitatory synapses onto retinal ganglion cells during development. Neural Dev 6.

Steinecke A, Hozhabri E, Tapanes S, Ishino Y, Zeng H, Kamasawa N, Taniguchi H (2017) Neocortical chandelier cells developmentally shape axonal arbors through reorganization but establish subcellular synapse specificity without refinement. eNeuro 4:1–14.

Tardin C, Cognet L, Bats Â, Lounis B (2003) Direct imaging of lateral movements of AMPA receptors inside synapses. EMBO J 22:16.

Thomas P, Mortensen M, Hosie AM, Smart TG (2005) Dynamic mobility of functional GABAA receptors at inhibitory synapses. Nat Neurosci 8:889–897.

Tian N, Copenhagen DR (2001) Visual deprivation alters development of synaptic function in inner retina after eye opening. Neuron 32:439–449.

Tollin DJ (2003) The lateral superior olive: A functional role in sound source localization. Neuroscientist 9:127–143.

Tovar KR, Westbrook GL (2002) Mobile NMDA receptors at hippocampal synapses. Neuron 34:255–264.

Tritsch NX, Yi E, Gale JE, Glowatzki E, Bergles DE (2007) The origin of spontaneous activity in the developing auditory system. Nature 450:50–55.

Werthat F, Alexandrova O, Grothe B, Koch U (2008) Experience-dependent refinement of the inhibitory axons projecting to the medial superior olive. Dev Neurobiol 68:1454–1462.

Winnubst J, Cheyne JE, Niculescu D, Lohmann C (2015) Spontaneous Activity Drives Local Synaptic Plasticity InVivo. Neuron 87:399–410.

Wu G-Y, Cline HT (1998) Stabilization of Dendritic Arbor Structure in Vivo by CaMKII. Science (80-) 279:222–226.

Wu X, Fu Y, Knott G, Lu J, Cristo G Di, Josh Huang Z (2012) GABA signaling promotes synapse elimination and axon pruning in developing cortical inhibitory interneurons. J Neurosci 32:331–343.

Yuste R (2010) Dendritic spines. Cambridge, Massachusetts: The MIT Press.

4.7 Tables

Table 1

Antigen	Host (Isoform)	Catalogue number	Dilution	Conjugated Fluorophores
Gephyrin	Mouse IgG1	Synaptic System 147021	1:250	
VGLUT1	Guinea pig	Millipore AB5905	1:2000	
Mouse	Donkey	Jackson Immuno Research 715605151	1:500	Alexa 647
Guinea pig	Donkey	Jackson Immuno Research 715165151	1:500	Cy 3

Antibodies used in this study.

4.8 Figures

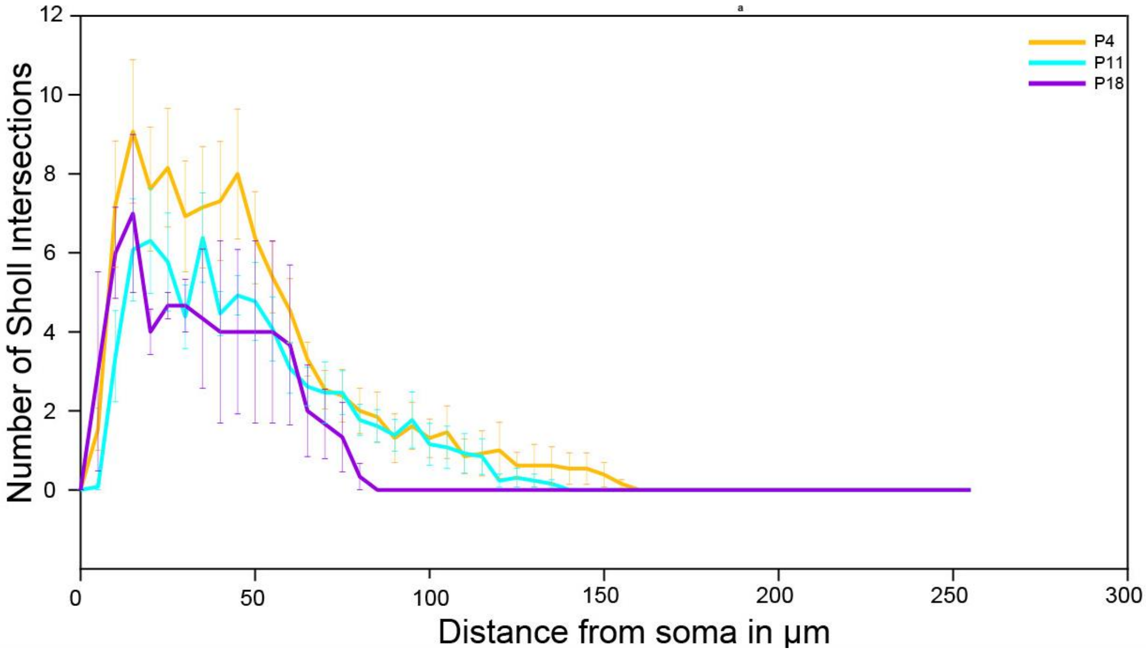

Figure 4-1

Figure 1. Mean number of Sholl intersections as a function of distance from the centroid of the soma. Sholl intersections are measured in every 5 µm. The number of intersections in the first 5 µm indicates the radius of the soma. Error bars show s.e.m.

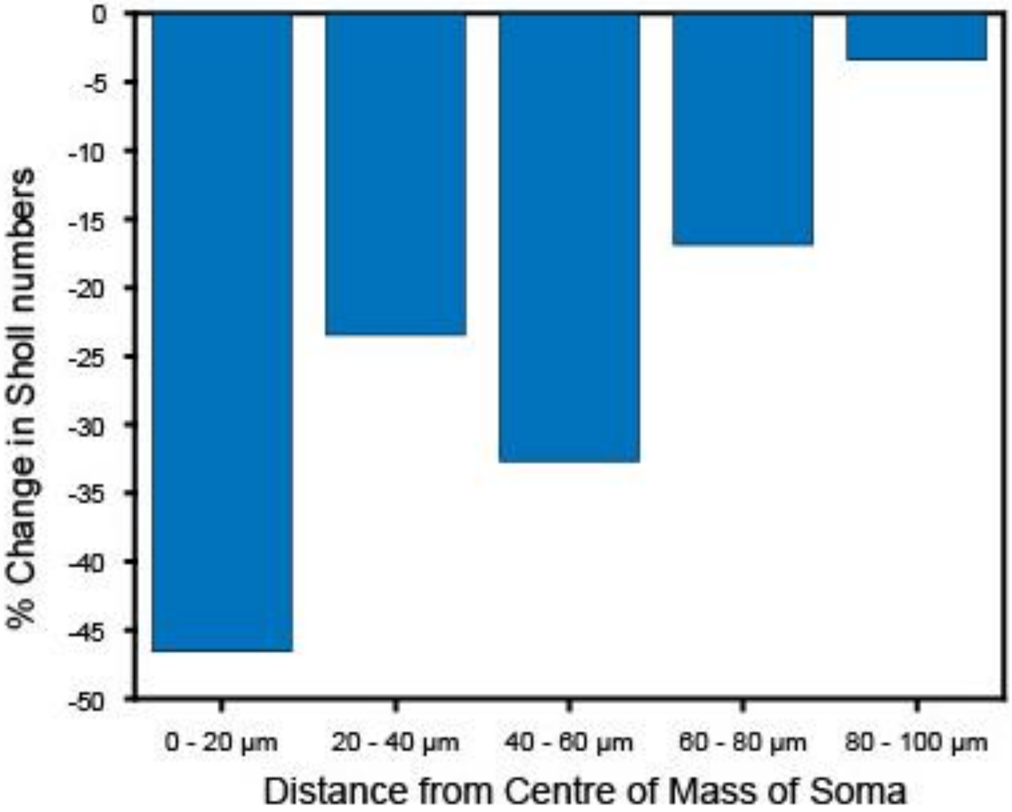

Figure 4-2

Figure 2. Percent change in mean number of Sholl intersections during the week before hearing onset (measured in 20-µm bins).

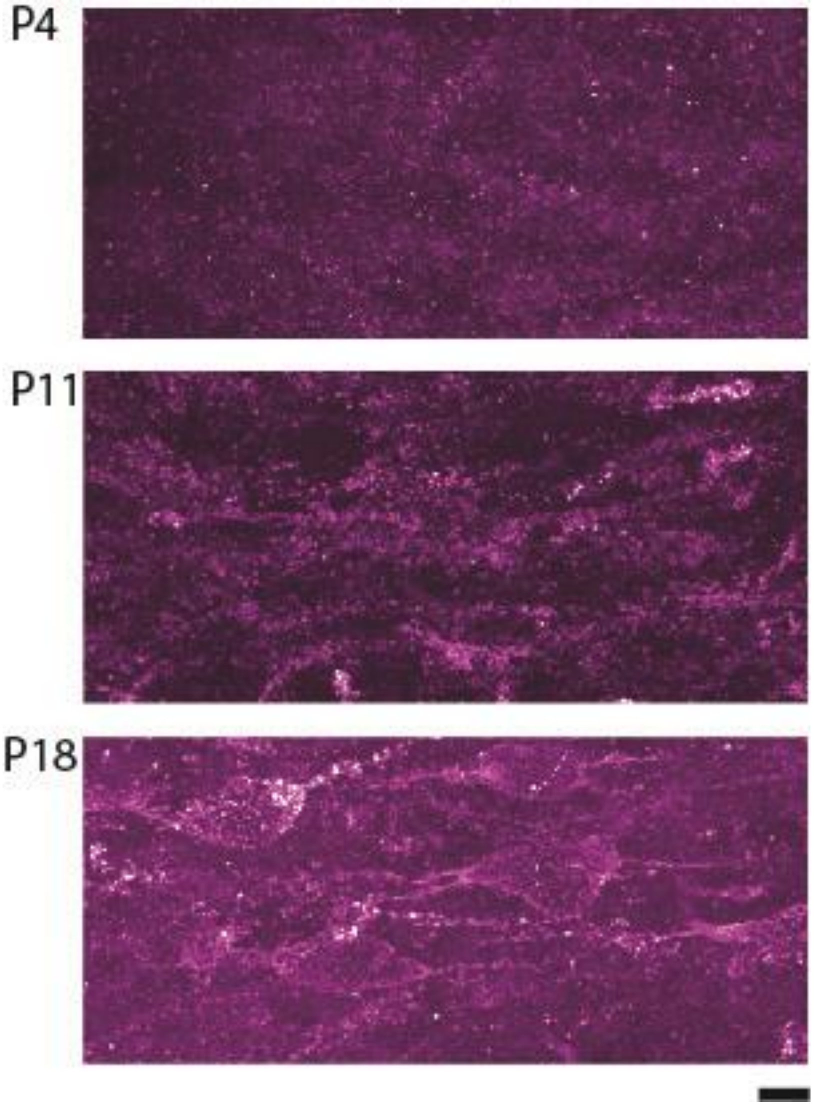

Figure 4-3

Figure 3. Putative inhibitory synapses (gephyrin staining) are shown in maximum projection. By P11 and P18, the somata and proximal dendrites can be clearly seen, outlined by the gephyrin positive puncta. Scale bar = 5 µm.

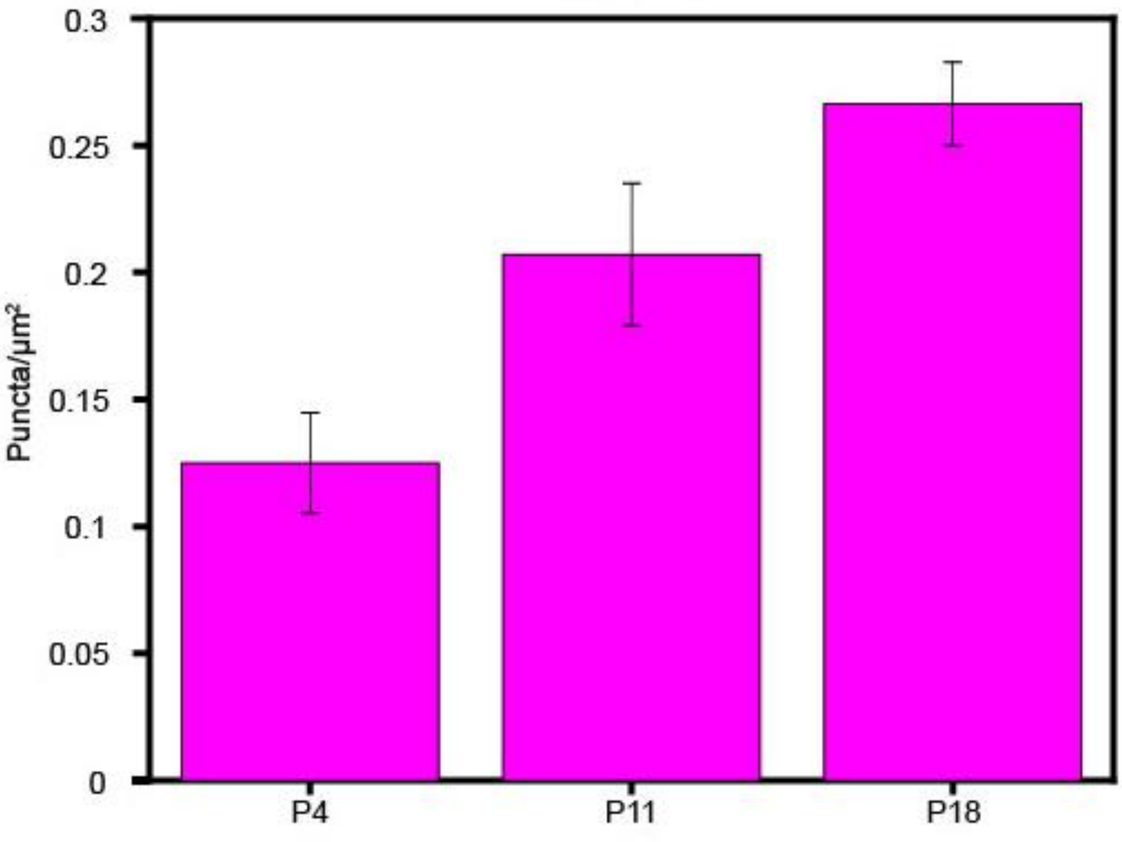

Figure 4-4

Figure 4. Mean density of gephyrin at the soma increases in the first three postnatal weeks. Average surface density of gephyrin puncta increases from 0.125 puncta/µm^2 to 0.207 puncta/µm^2 between P4 and P11, followed by a further increase to 0.2663 from P11 to P18. Error bars show s.e.m.

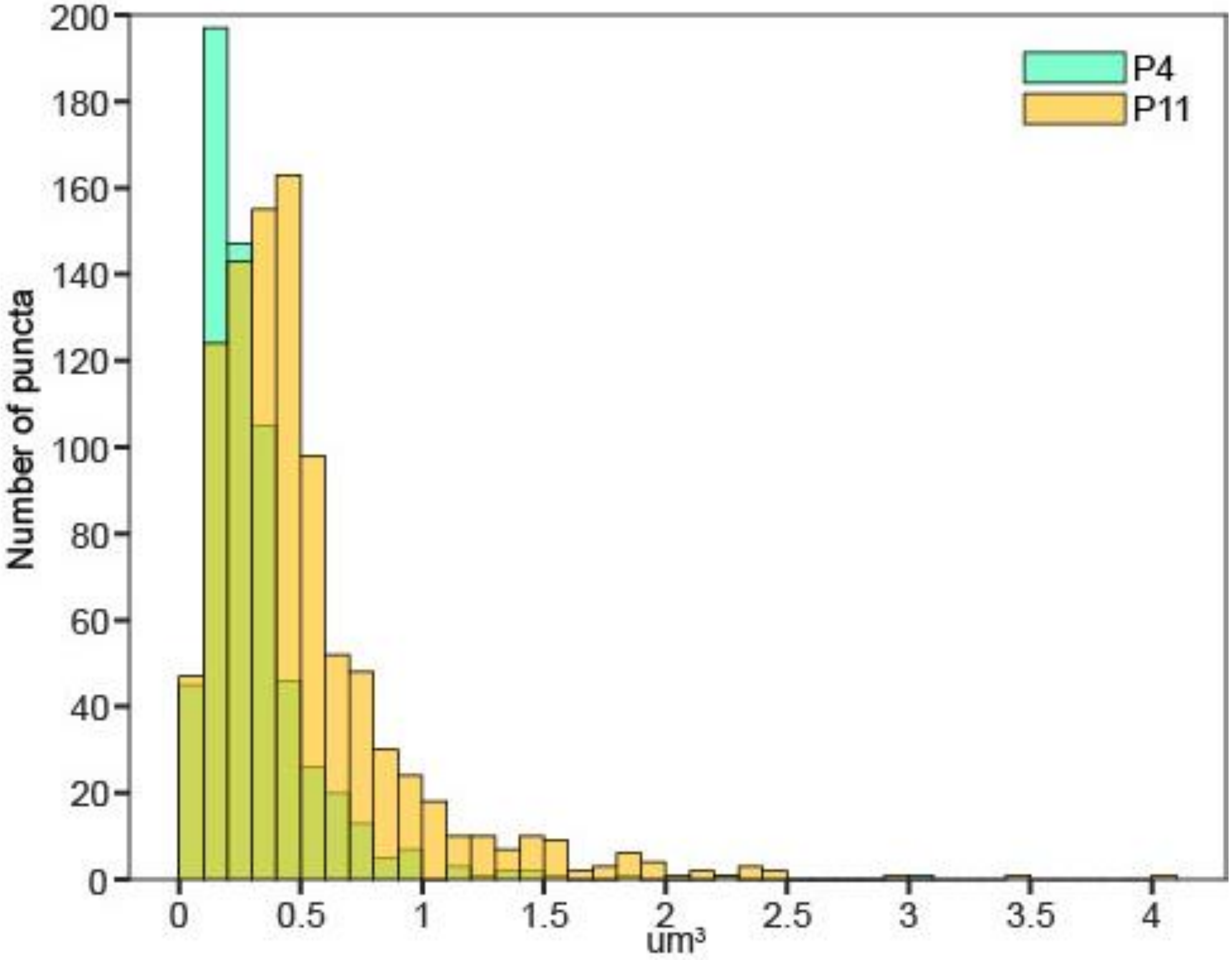

Figure 4-5

Figure 5. Histogram of somatic gephyrin volume. Median gephyrin-positive synapse volume is higher in P11 than P4 neurons.

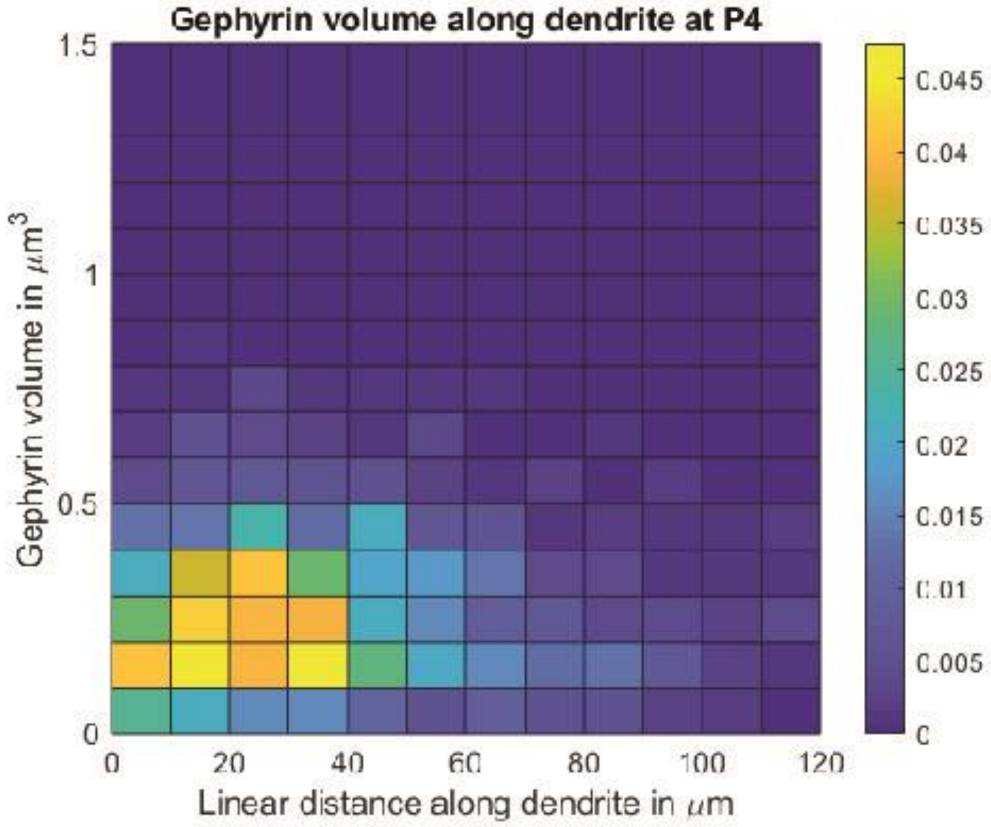
Gephyrin volume along dendrite at P4
Gephyrin volume in μm^3
Linear distance along dendrite in μm
0
0.5
1
1.5
0
20
40
60
80
100
120
0
0.005
0.01
0.015
0.02
0.025
0.03
0.035
0.04
0.045

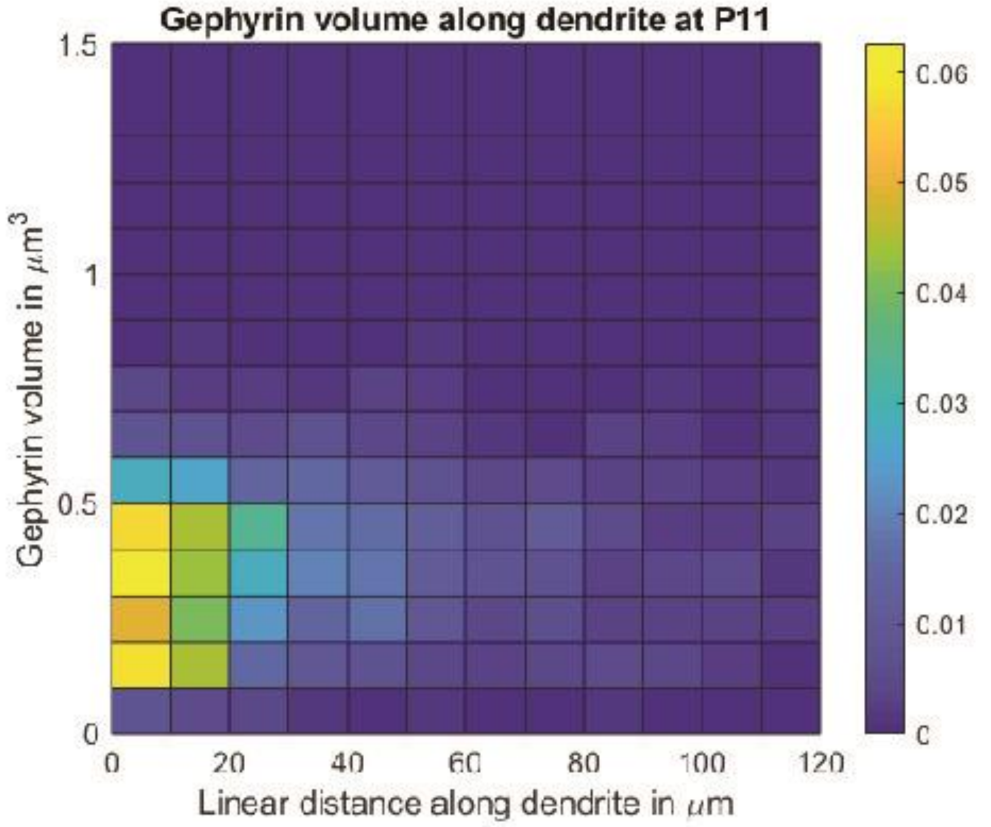
Gephyrin volume along dendrite at P11
Gephyrin volume in μm^3
Linear distance along dendrite in μm
0
0.5
1
1.5
0
20
40
60
80
100
120
0
0.01
0.02
0.03
0.04
0.05
0.06

Figure 4-6

Figure 6. Heatmap shows the probabilities density function of gephyrin along the dendrite with a specific volume. More and larger gephyrin positive synapses are located at the proximal dendrite in P11 neurons. Both the number and the size of gephyrin in P4 neurons are more randomly distributed.

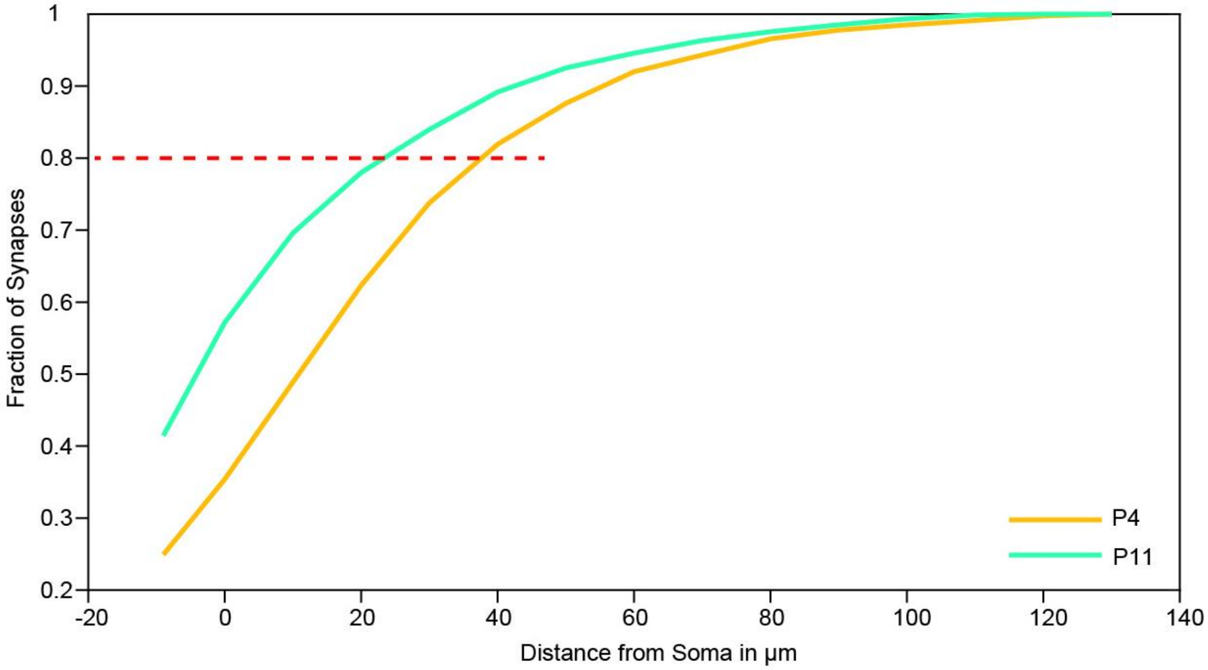

Figure 4-7

Figure 7. Cumulative distribution of gephyrin puncta as a function of dendritic distance (somatic synapses in the negative region). The red dashed line indicates the 80% of the gephyrin puncta are located within the proximal 20 µm dendrite for P11 neurons and proximal 40 µm dendrite for P4 neurons.

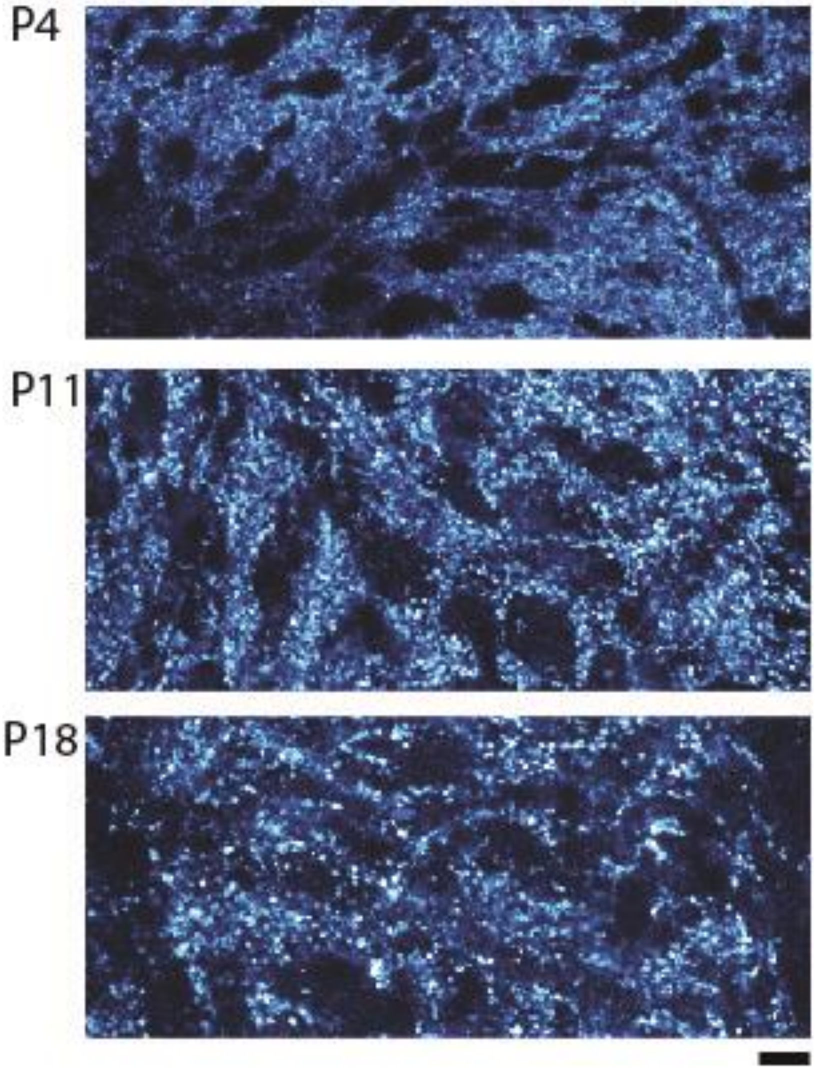

Figure 4-8

Figure 8. Putative excitatory synapses (VGLUT1 staining) are shown in maximum projection. Somata are outlined by the VGLUT1 positive puncta in P4 and P11 tissue. Scale bar = 5 µm.

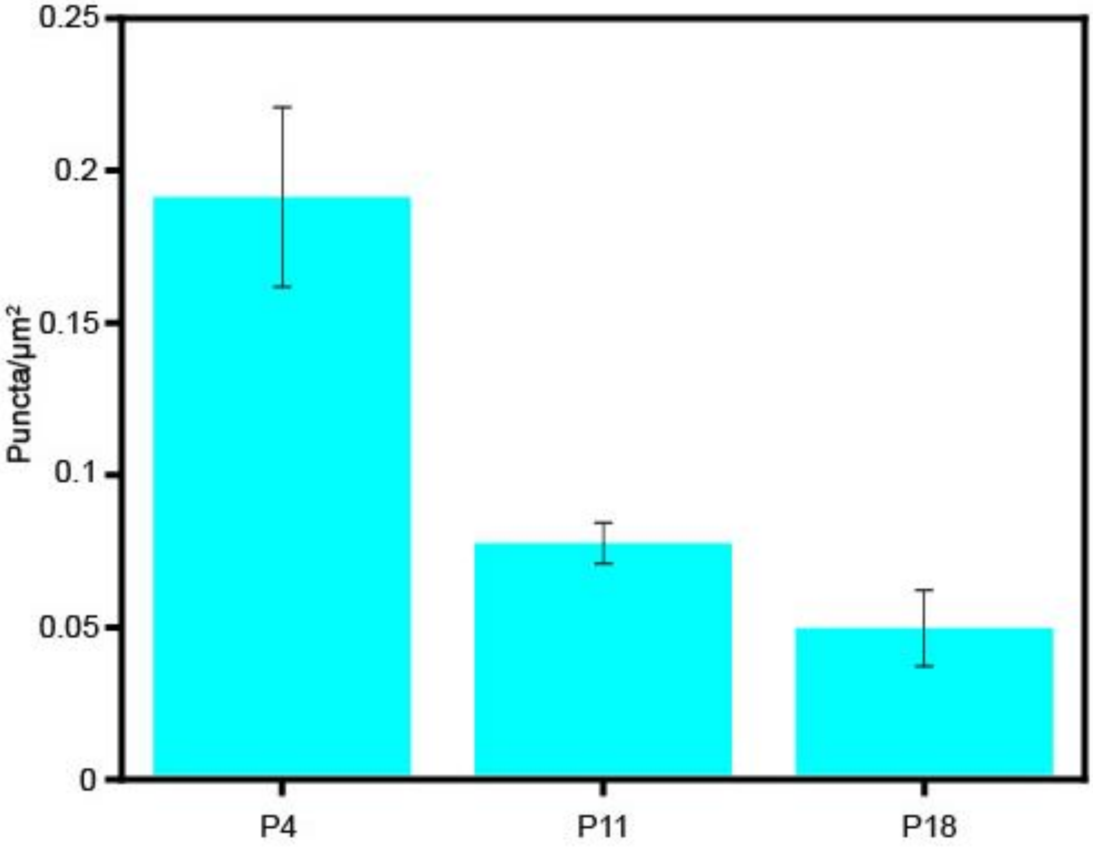

Figure 4-9

Figure 9. Excitatory synapses (VGLUT1 staining) become sparse at the soma between P4 and P11. The average surface density of VGLUT1 at the soma decreases from 0.1913 puncta/µm^2 to 0.07761 puncta/µm^2 between P4 and P11. Error bars represent s.e.m.

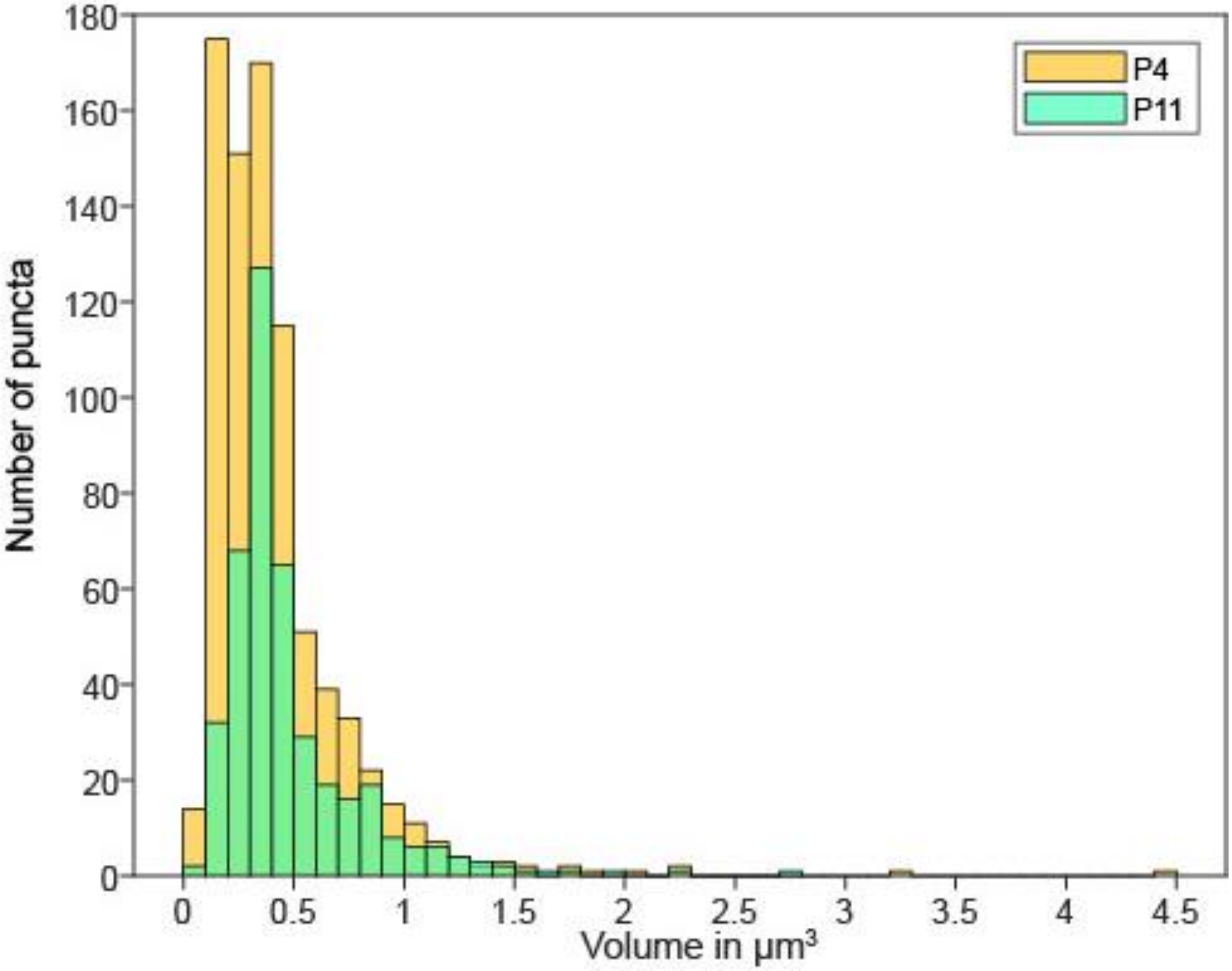

Figure 4-10

Figure 10. Distribution of volumes for somatic VGLUT1 puncta. The average somatic VGLUT1 volumes for P4 and P11 are 0.4166 ± 0.3332 µm^3 and 0.4782 ± 0.3170 µm^3.

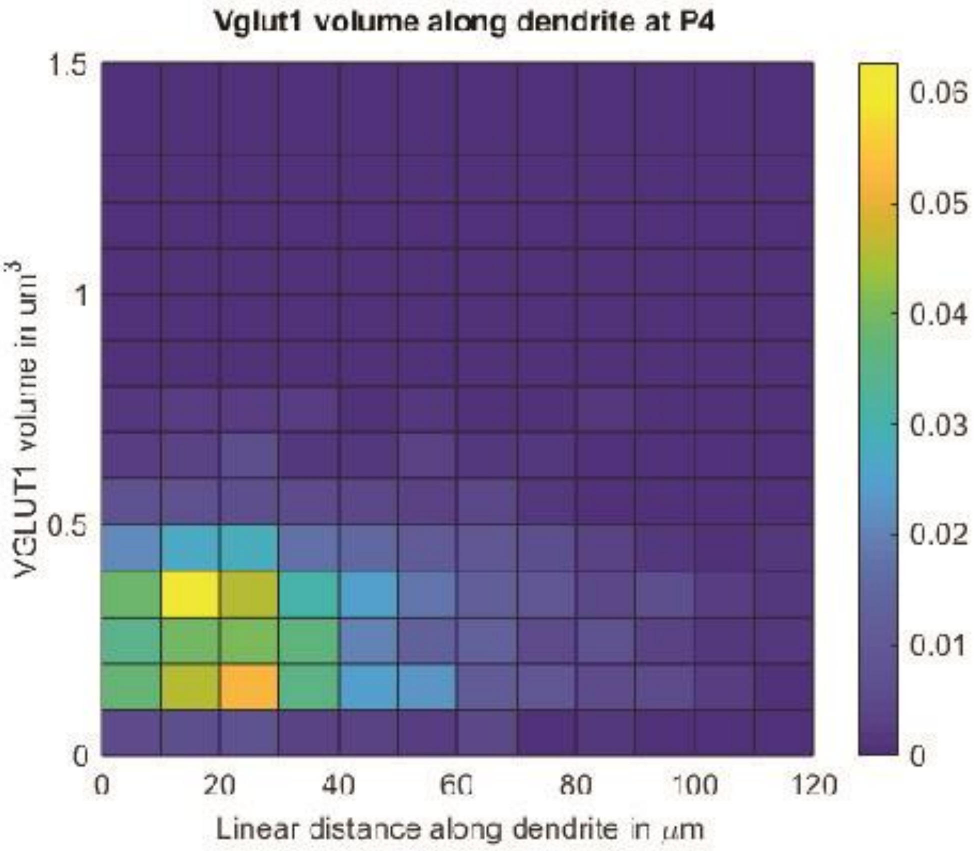
Vglut1 volume along dendrite at P4

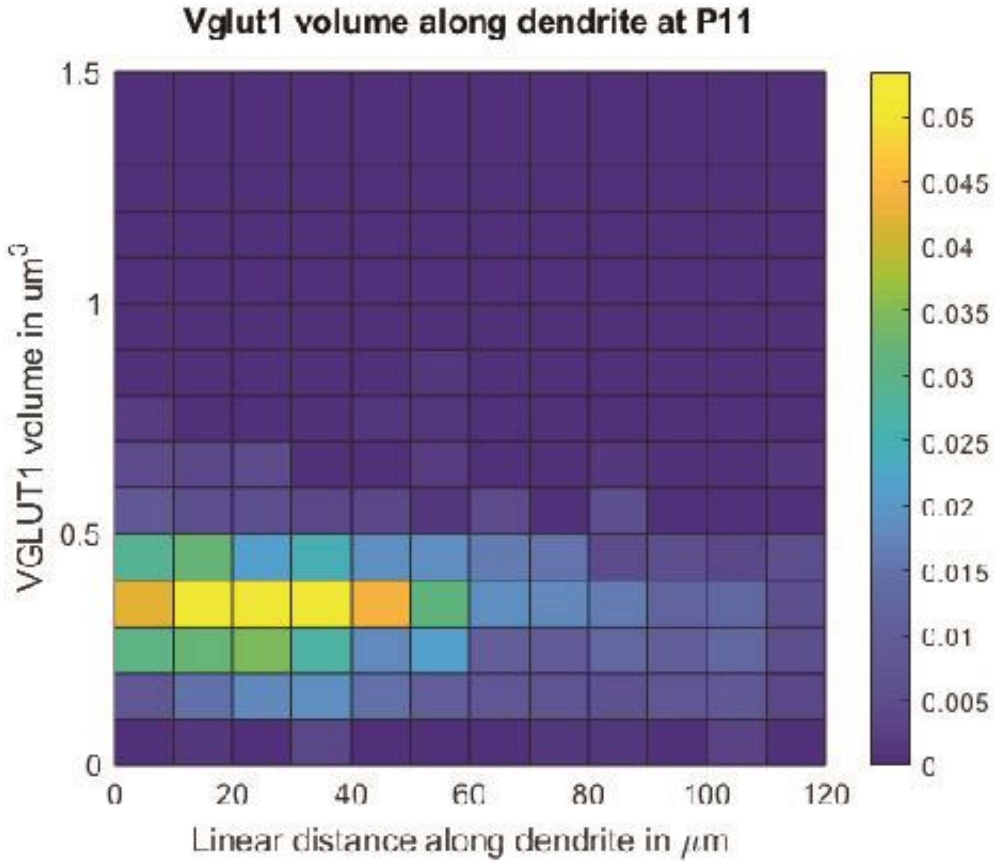
Vglut1 volume along dendrite at P11

Figure 4-11

Figure 11. Heatmap showing the probabilities of encountering VGLUT1 puncta of specific volumes along the dendrite. Whereas most of the VGLUT1 puncta at P4 are restricted to the proximal 40 µm of the dendrite, VGLUT1 puncta at P11 extended to a more distal region. The volumes of VGLUT1 puncta were larger at P11.

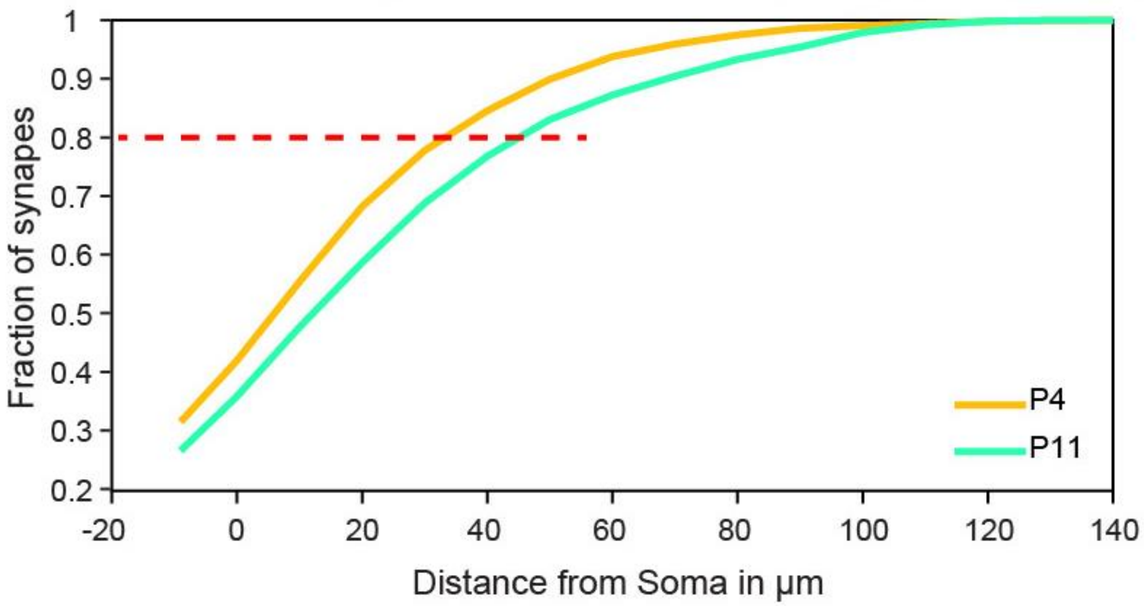

Figure 4-12

Figure 12. Cumulative distribution of VGLUT1 puncta as a function of dendritic distance (somatic synapses in the negative region). The red dashed line indicates where 80% of the VGLUT1 puncta can be found for P4 neurons (proximal 30 µm of dendrite) and proximal for P11 neurons (proximal 50 µm of dendrite).

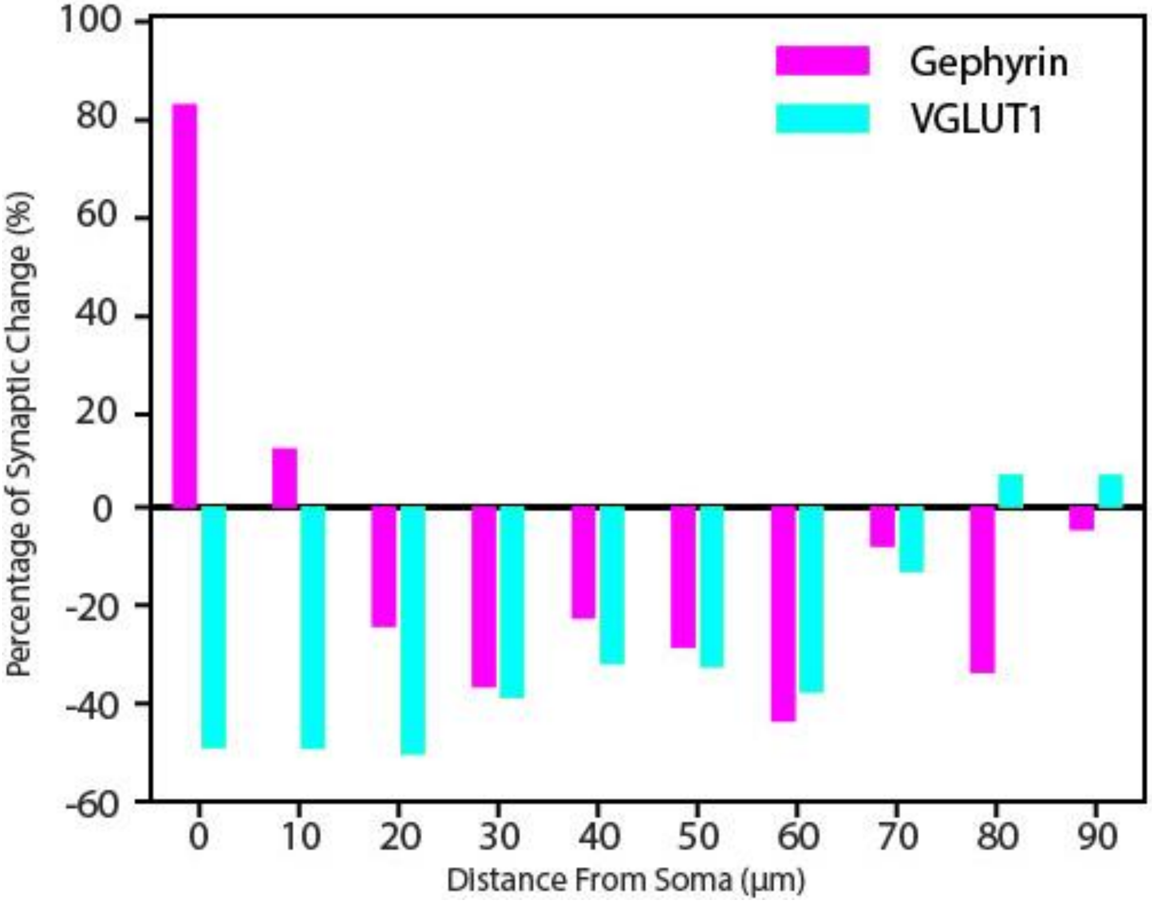

Figure 4-13

Figure 13. Percent change of in number of gephyrin-positive and VGLUT1-positive synapses from P4 to P11. Gephyrin-positive synapse density in the first 10-um segment increased by 80% between P4 and P11, whereas VGLUT1-positive synapse density decreased by about 50% between P4 and P11 in the first 30-um segment.

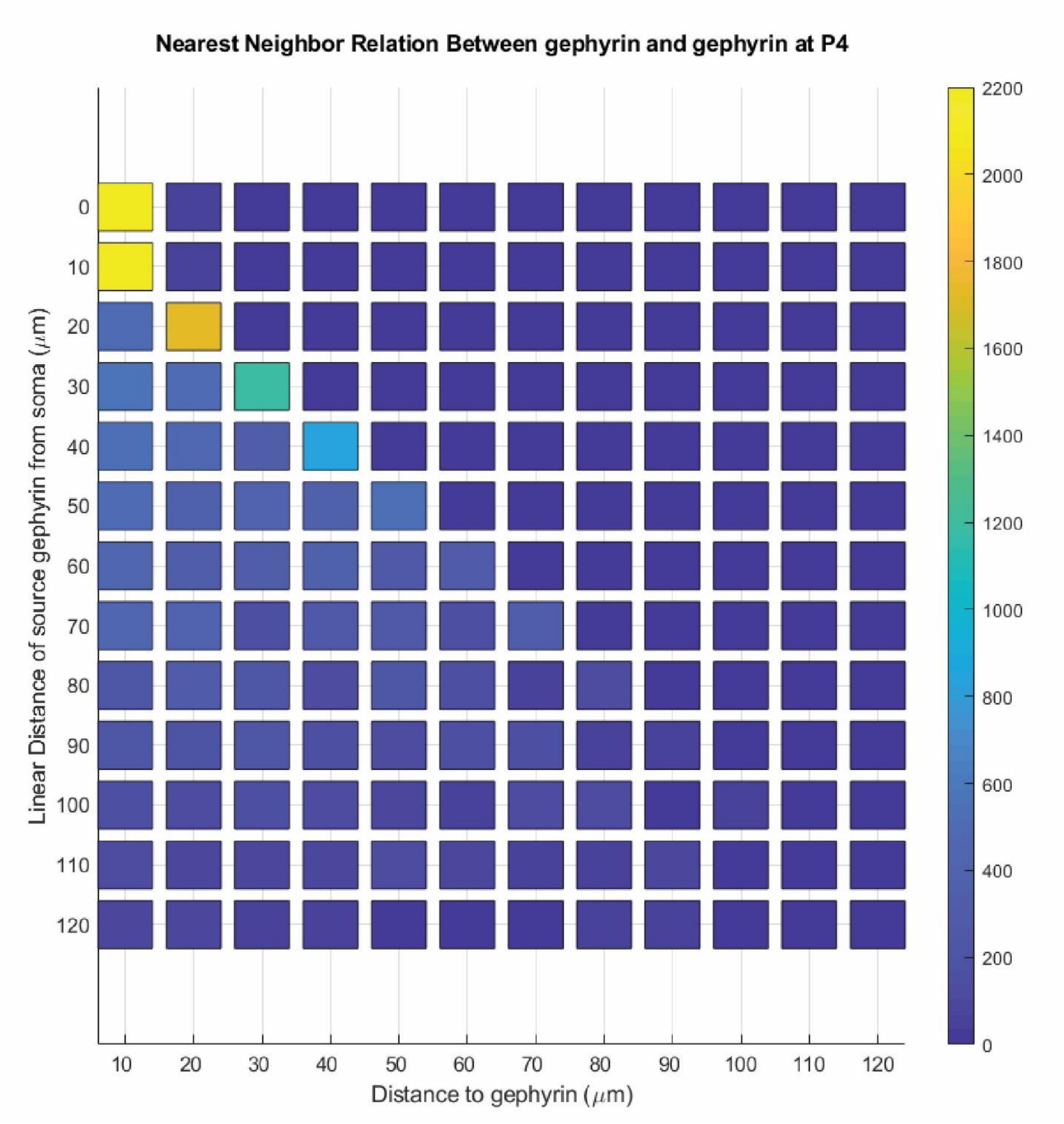

Figure 4-14

Figure 14. Heatmap shows aggregate distance counts from a given source gephyrin punctum to its nearest 50 neighboring gephyrin puncta at P4. Source gephyrin puncta are sampled in 10-µm segments, with somatic gephyrin puncta at 0 µm. Distances are sampled every 10 µm.

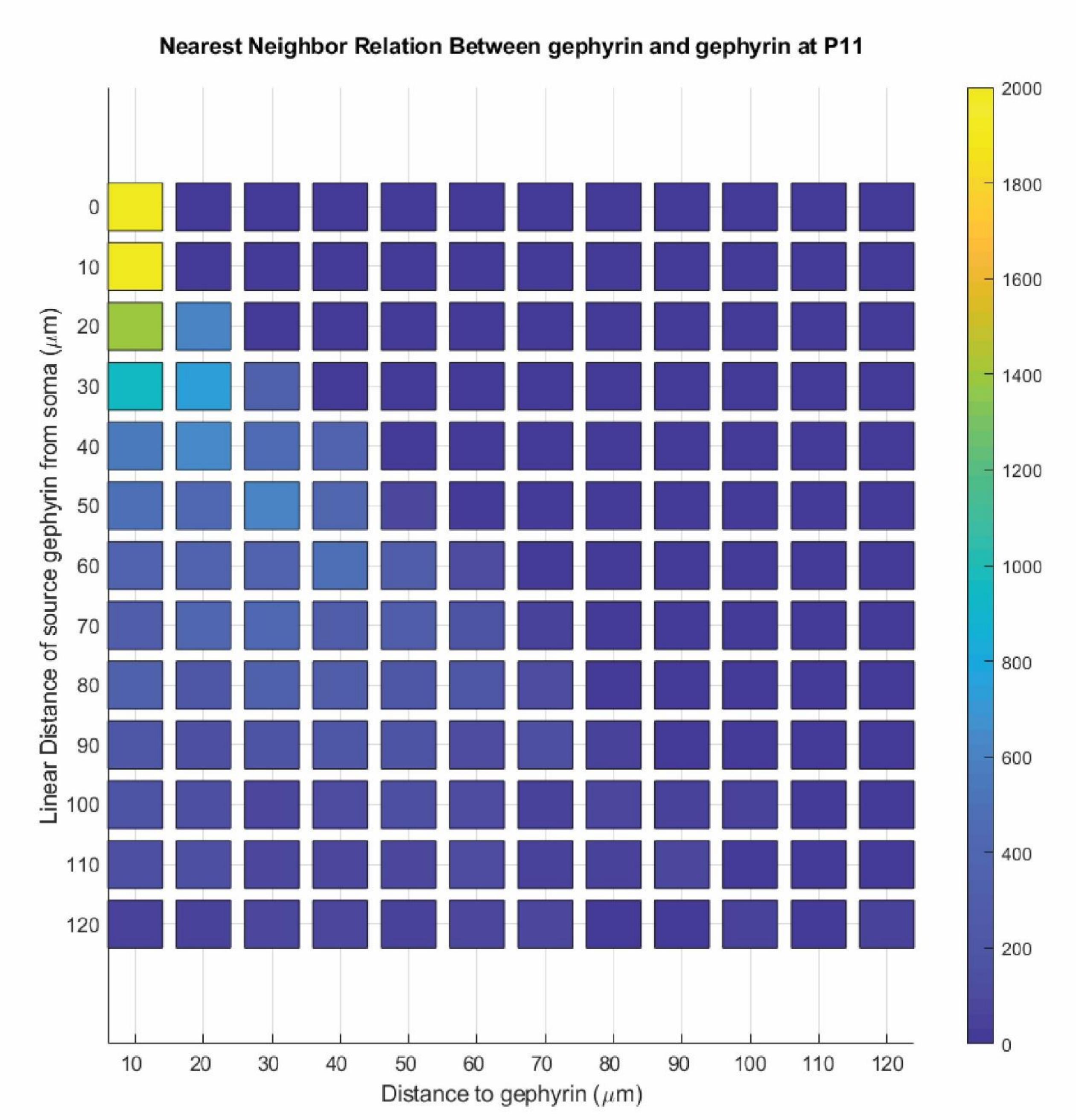

Figure 4-15

Figure 15. Heatmap shows aggregate distance counts from a given source gephyrin punctum to the nearest 50 neighboring gephyrin puncta at P11. Source gephyrin puncta are sampled in 10-µm segments, with somatic gephyrin puncta at 0 µm. Distances are sampled every 10 µm.

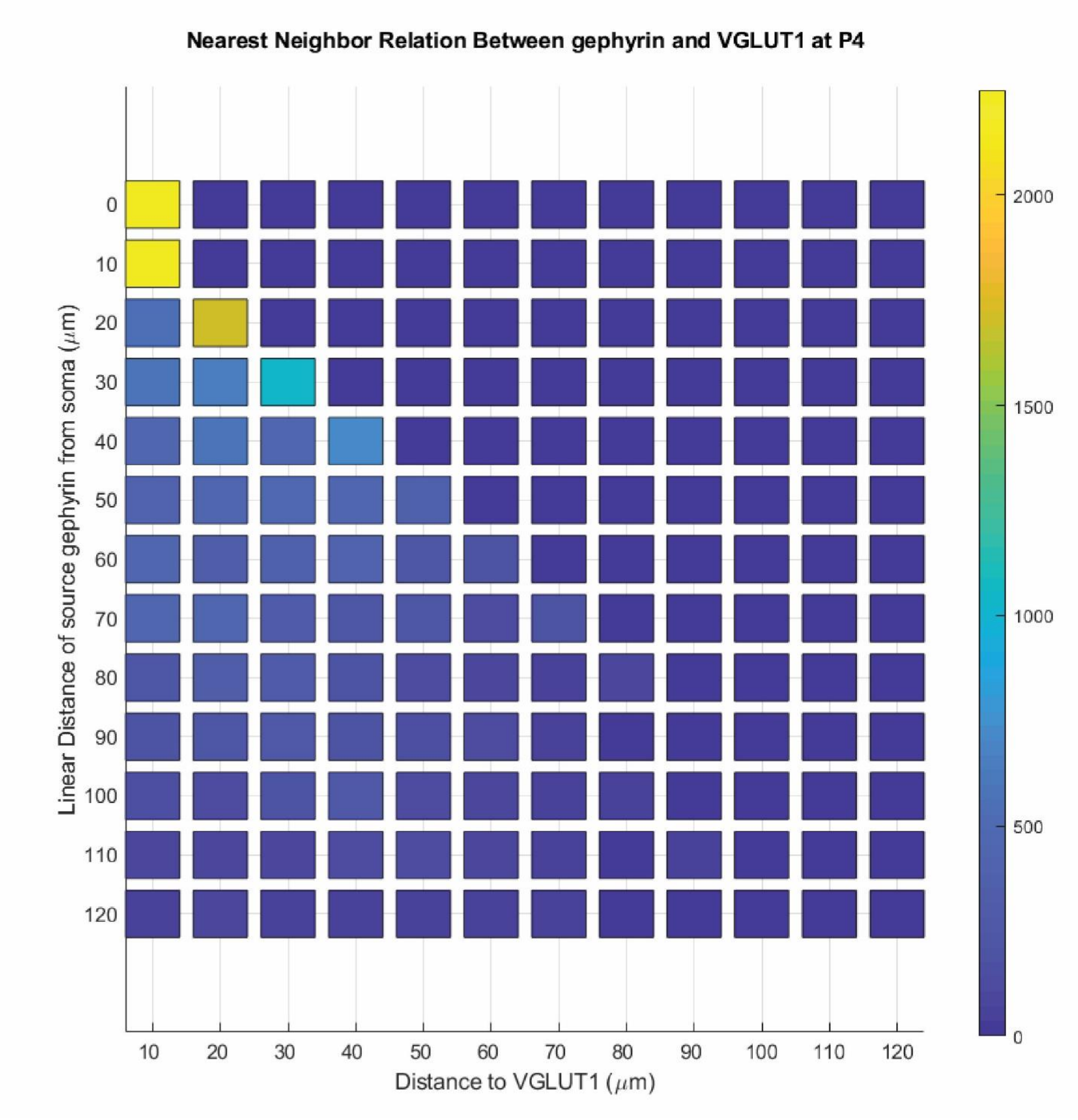

Figure 4-16

Figure 16. Heatmap shows aggregate distance counts from a given source gephyrin punctum to the nearest 50 neighboring VGLUT1 puncta at P4. Source gephyrin puncta (5) are sampled from each 10-µm segment, with somatic gephyrin puncta at 0 µm. The counted distances are sampled every 10 µm.

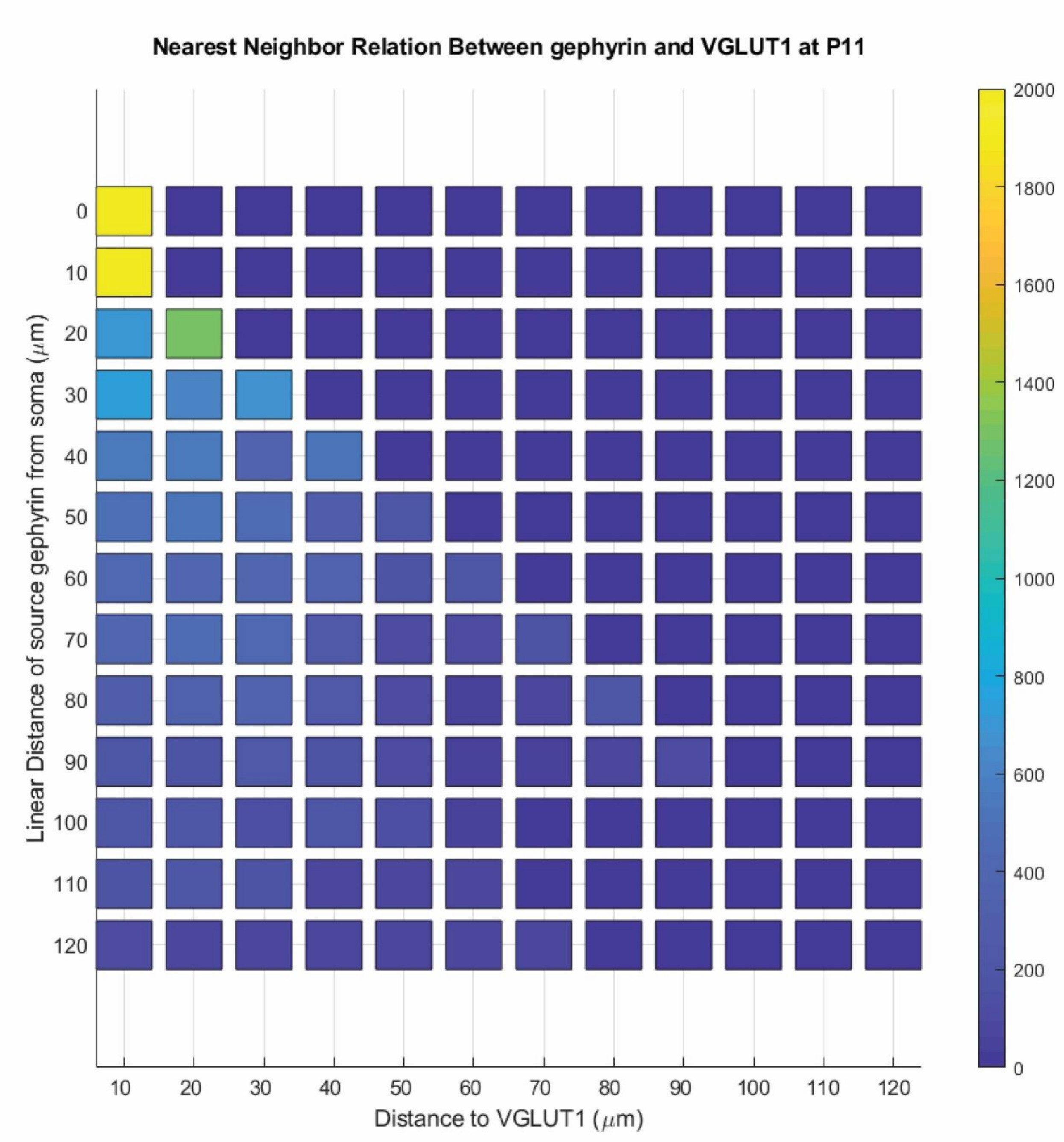

Figure 4-17

Figure 17. Heatmap shows aggregate distance counts from a given source gephyrin punctum to the nearest 50 neighboring VGLUT1 puncta at P11. Source gephyrin puncta are sampled at every 10 µm segments, with somatic gephyrin puncta at 0 µm. The counted distances are sampled every 10 µm.

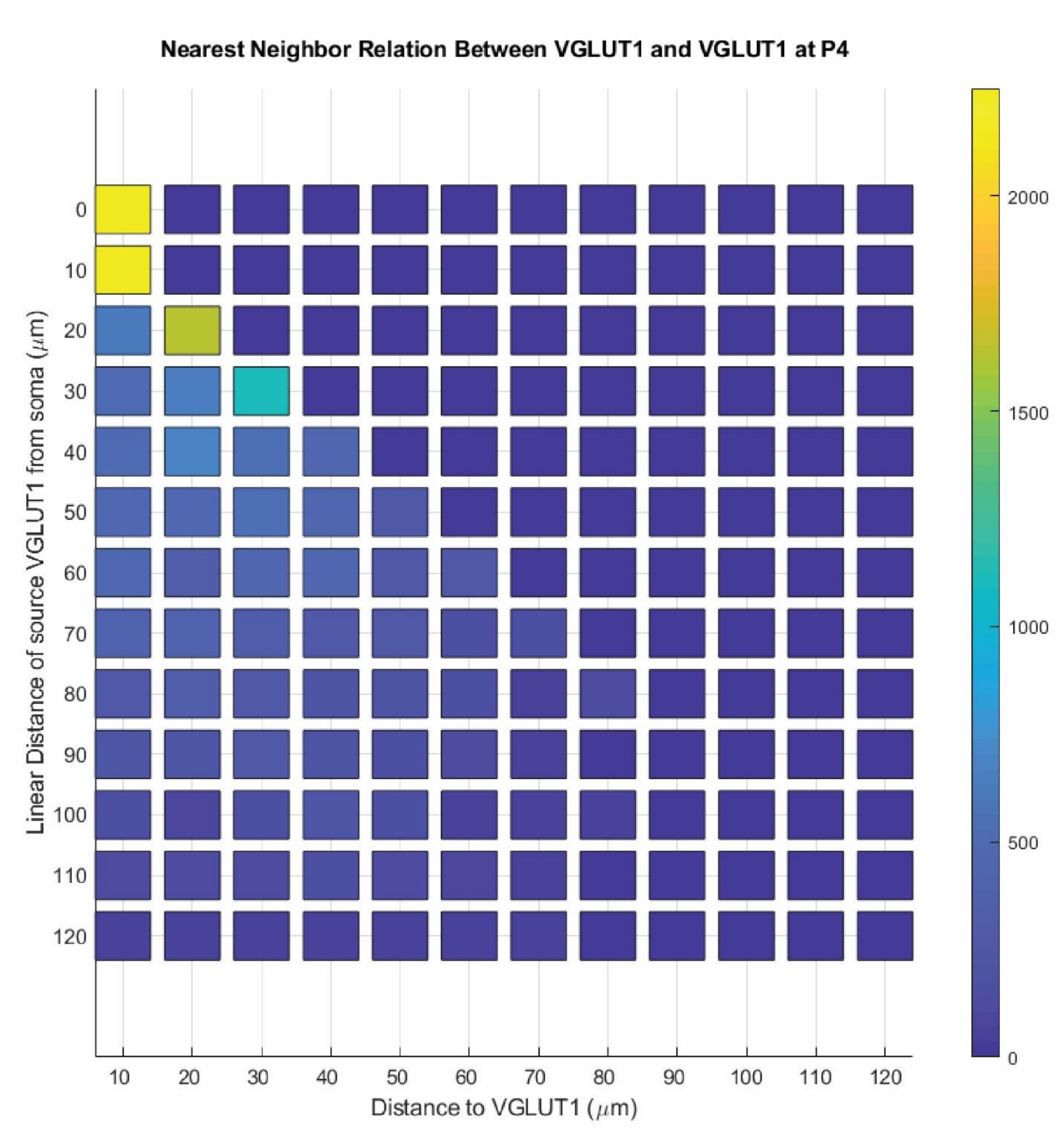

Figure 4-18

Figure 18. Heatmap shows aggregate distance counts from a given source VGLUT1 punctum to the nearest 50 neighboring VGLUT1 puncta at P4. Source VGLUT1 puncta are sampled at every 10 µm segments, with somatic VGLUT1 puncta at 0 µm. The counted distances are sampled every 10 µm.

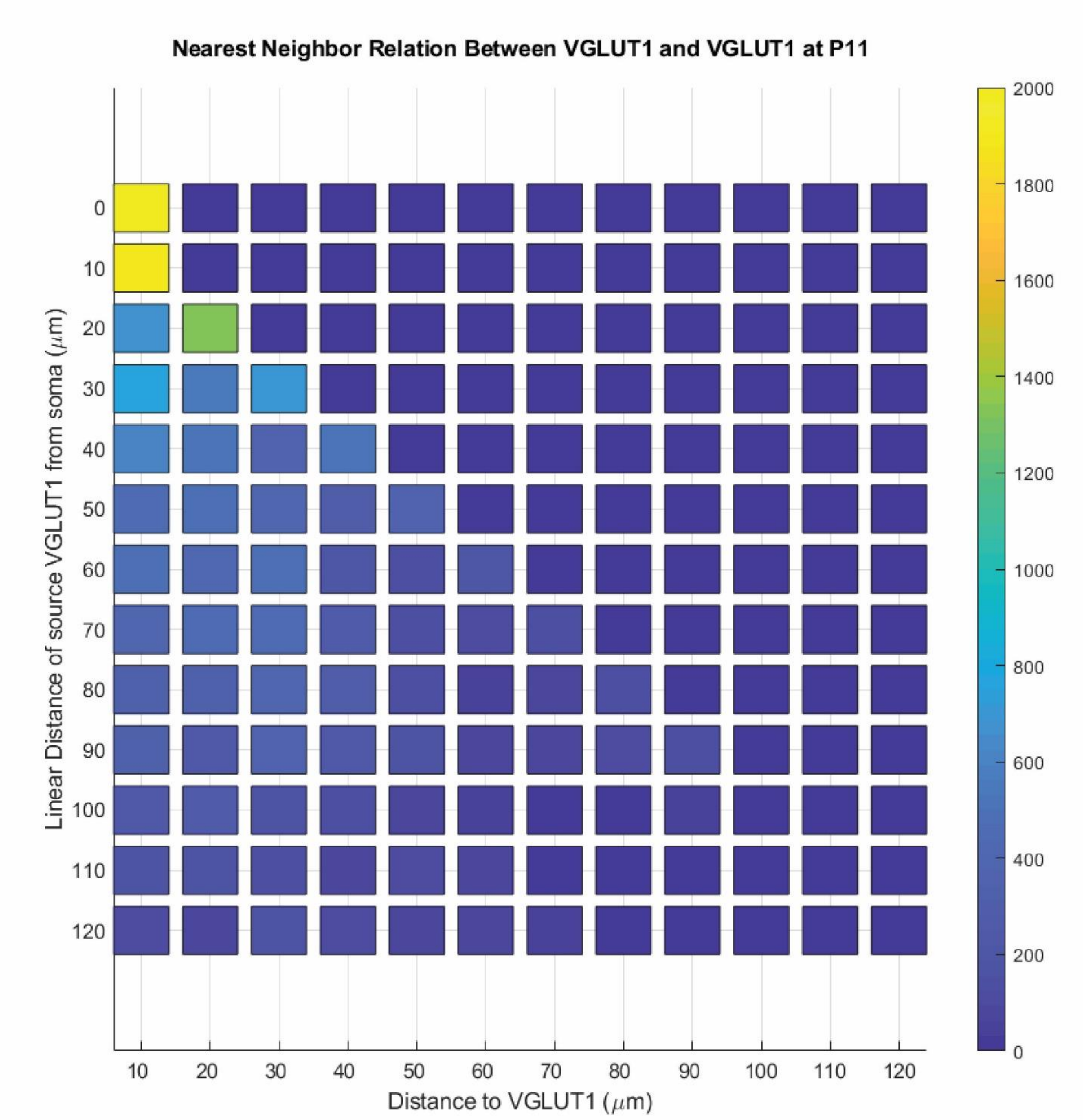

Figure 4-19

Figure 19. Heatmap shows aggregate distance counts from a given source VGLUT1 punctum to the nearest 50 neighboring VGLUT1 puncta at P11. Source VGLUT1 puncta are sampled at every 10 µm segments, with somatic VGLUT1 puncta at 0 µm. The counted distances are sampled every 10 µm.

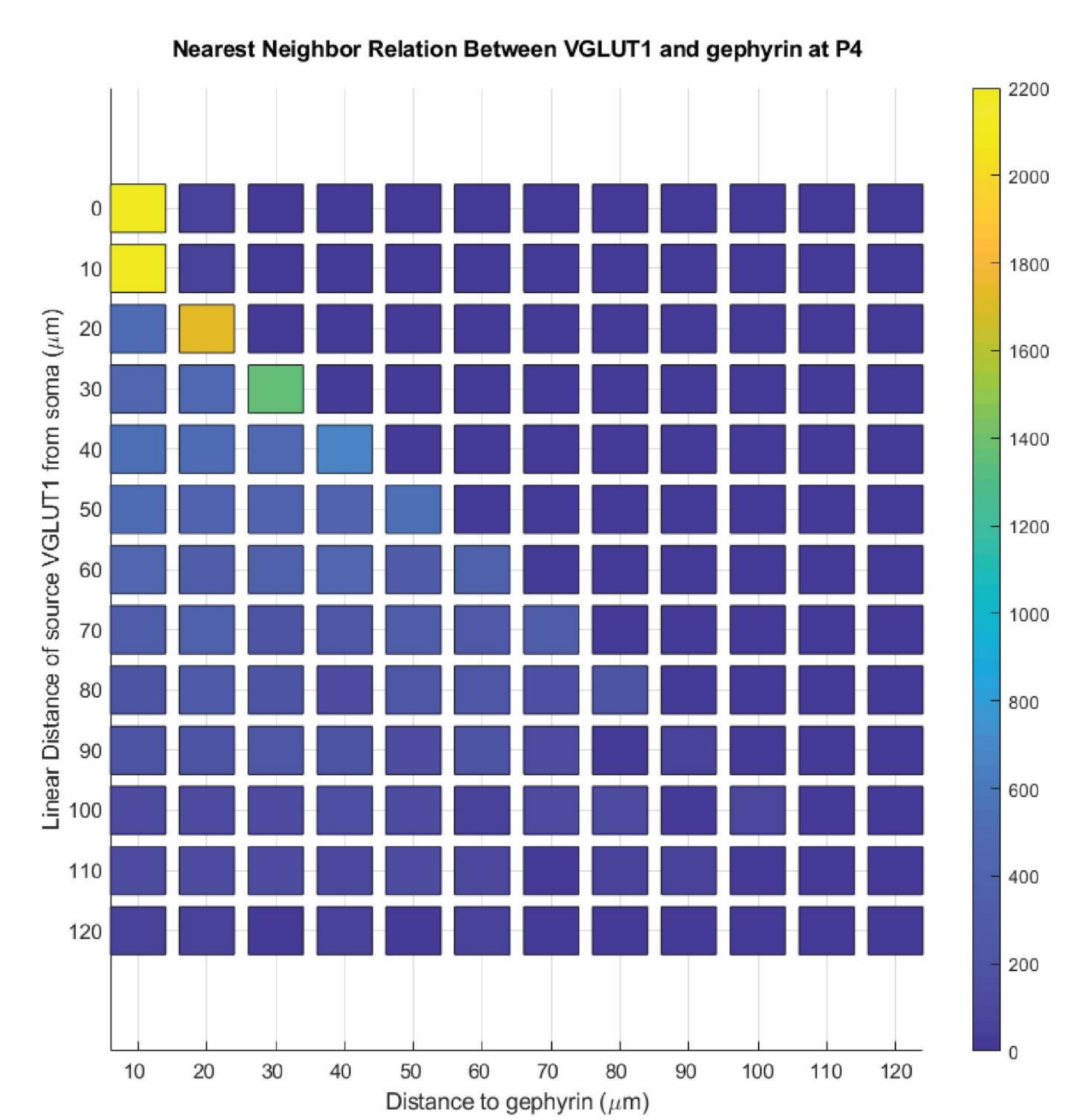

Figure 4-20

Figure 20. Heatmap shows aggregate distance counts from a given source VGLUT1 punctum to the nearest 50 neighboring gephyrin puncta at P4. Source VGLUT1 puncta are sampled at every 10 µm segments, with somatic VGLUT1 puncta at 0 µm. The counted distances are sampled every 10 µm.

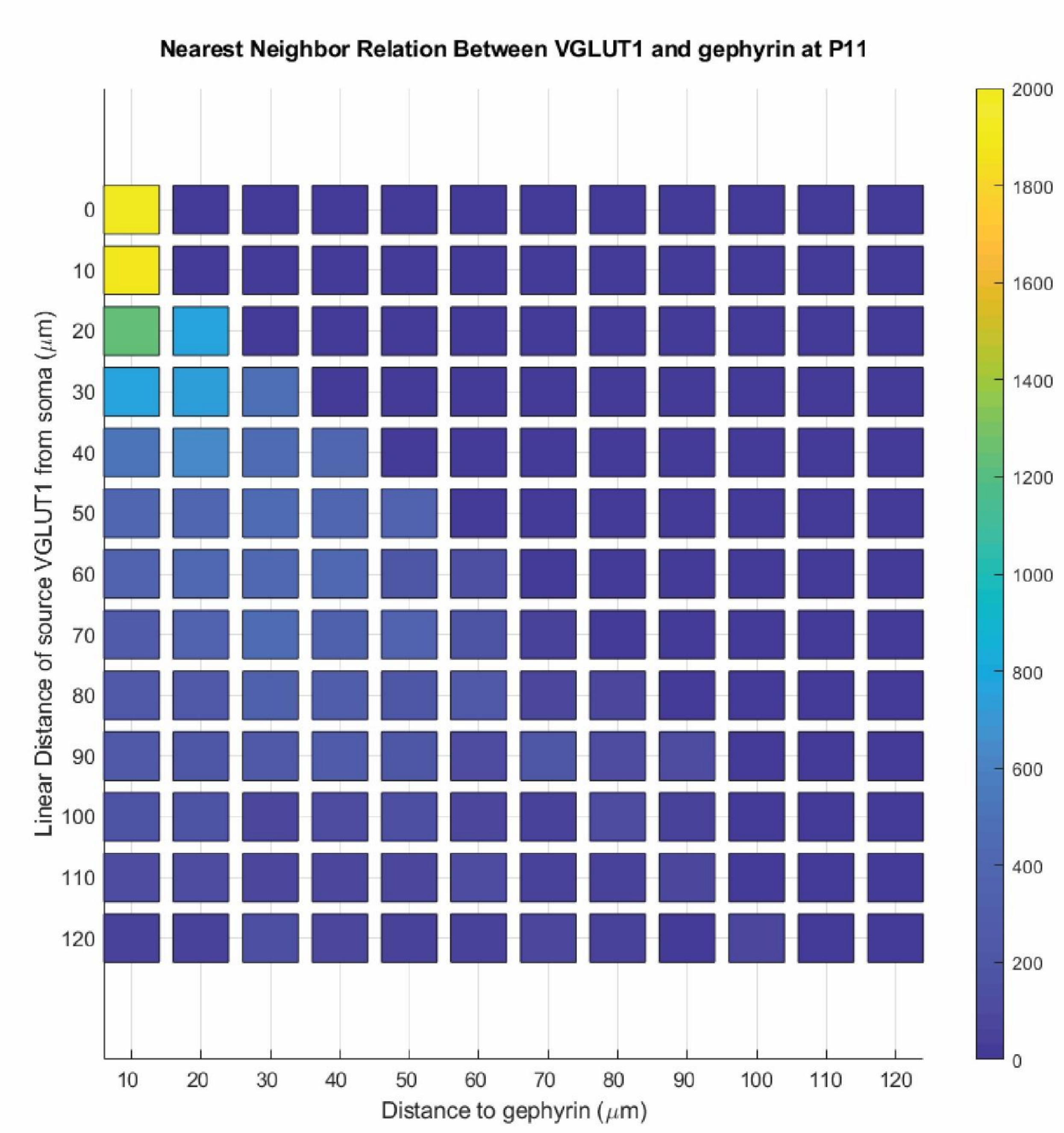

Figure 4-21

Figure 21. Heatmap shows aggregate distance counts from a given source VGLUT1 punctum to the nearest 50 neighboring gephyrin puncta at P11. Source VGLUT1 puncta are sampled at every 10 µm segments, with somatic VGLUT1 puncta at 0 µm. The counted distances are sampled every 10 µm.

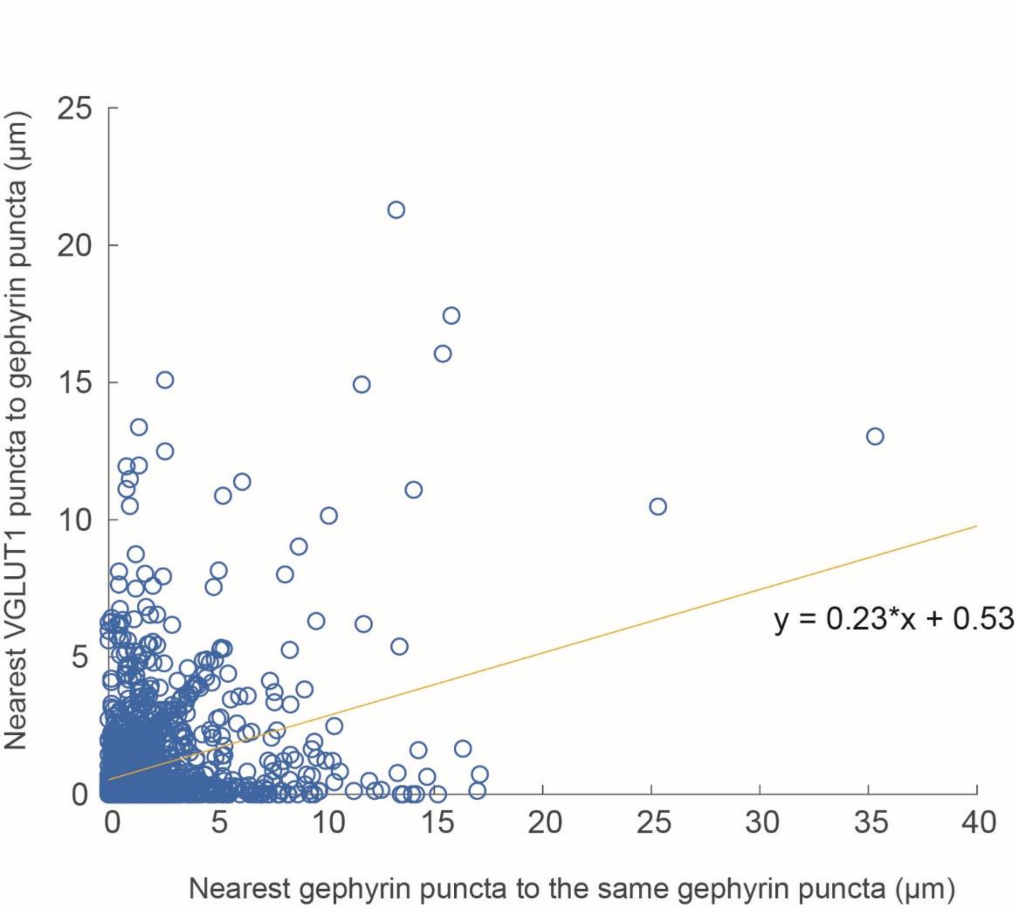

Figure 4-22

Figure 22. Scatterplot showing distances from individual inhibitory dendritic synapses to their nearest neighbouring (1NN distances) dendritic synapse, with distance to nearest inhibitory synapse on the x-axis, and distance to nearest excitatory synapse on the y-axis, at P4. Yellow line shows the linear regression corresponding to the indicated linear function.

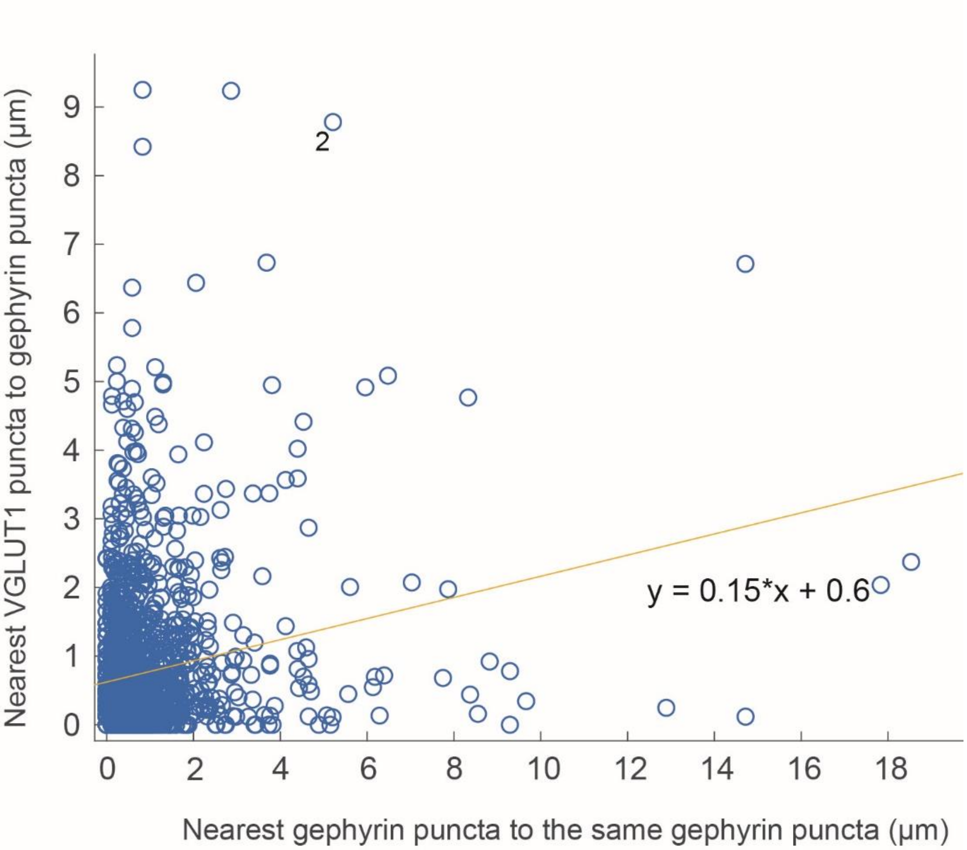

Figure 4-23

Figure 23. Scatterplot showing distances from individual inhibitory dendritic synapses to their nearest neighbouring (1NN distances) dendritic synapse, with distance to nearest inhibitory synapse on the x-axis, and distance to nearest excitatory synapse on the y-axis, at P11. Yellow line shows the linear regression corresponding to the indicated linear function.

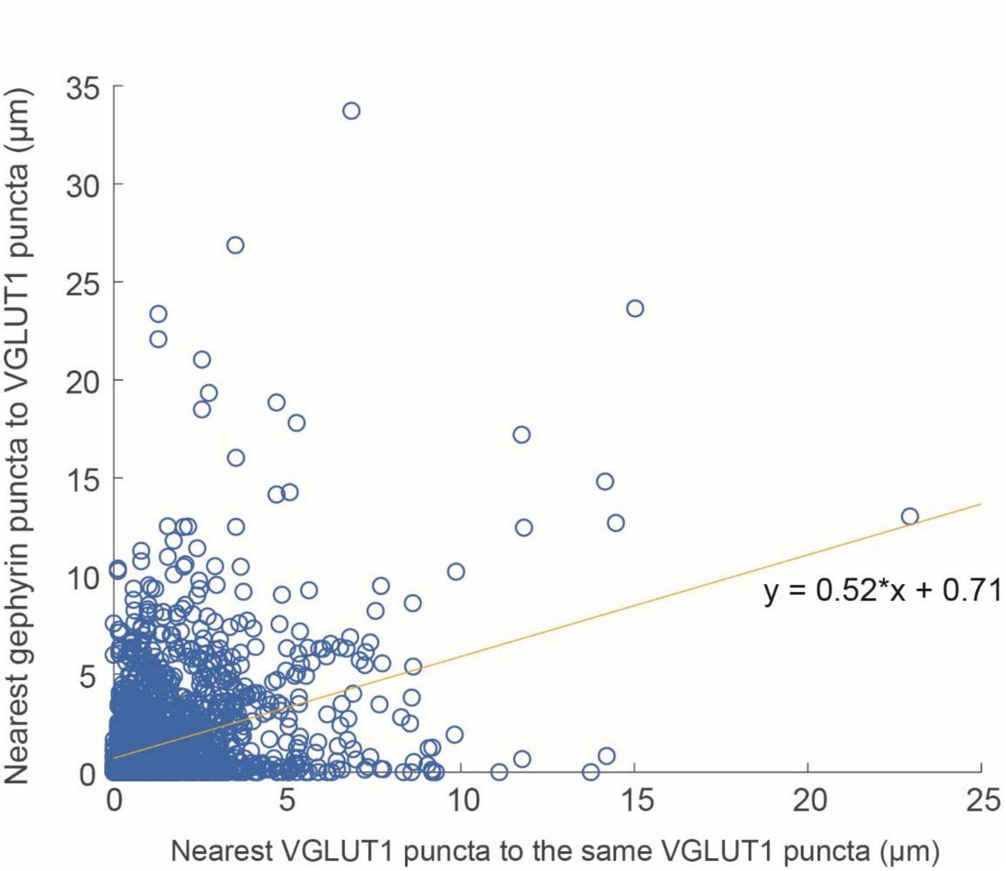

Figure 4-24

Figure 24. Scatterplot showing distances from individual excitatory dendritic synapses to their nearest neighbouring (1NN distances) dendritic synapse, with distance to nearest excitatory synapse on the x-axis, and distance to nearest inhibitory synapse on the y-axis, at P4. Yellow line shows the linear regression corresponding to the indicated linear function.

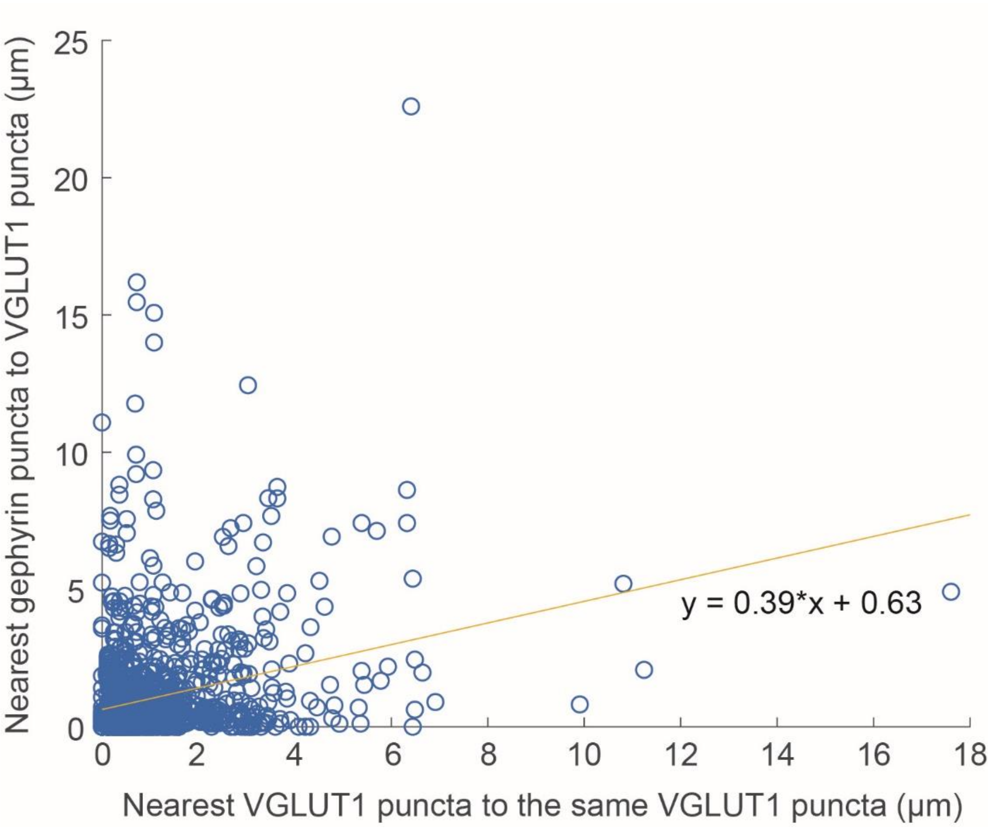

Figure 4-25

Figure 25. Scatterplot showing distances from individual excitatory dendritic synapses to their nearest neighbouring (1NN distances) dendritic synapse, with distance to nearest excitatory synapse on the x-axis, and distance to nearest inhibitory synapse on the y-axis, at P11. Yellow line shows the linear regression corresponding to the indicated linear function.

5 Chapter 5: Discussion

Research in neurobiology always has been, and remains today, heavily dependent on technical innovation. This thesis demonstrates the development of hardware and software tools for neurobiology research, culminating in an investigation of coordinated circuit refinement in auditory brainstem using the tools developed here. In Chapter 2, I report on a new, low-cost, Arduino-based single cell electroporator that allows us to label single neurons in tissue. In Chapter 3, I report on tests of available software for 3D reconstruction of neurons, and on implementation of an iterative thresholding-based watershed algorithm that allows us to segment synapses in 3D from confocal image stacks. In Chapter 4, I show how the tools I developed and described in the previous two chapters could be used to investigate a significant open question in developmental neuroscience.

5.1 The neurobiological question: what drives the redistribution of excitatory and inhibitory synapses in LSO?

Redistribution of synapses can be guided by spontaneous activity, and this may occur in the LSO of pre-hearing rats, where excitatory synapses are redistributed away from the soma during the same period that inhibitory synapses are redistributed towards soma, all in the absence of acoustic activity. Before hearing onset, the AVCN and MNTB, which form the direct excitatory and inhibitory projections to the LSO, exhibit patterned spontaneous activity (Tritsch et al., 2010) that is required for the precise frequency map refinement in the MNTB-LSO pathway (Clause et al., 2014). However, whether this spontaneous activity is required for the redistribution of synapses remains unknown. In the retina, a few days before eye opening, glutamate released from bipolar cells initiates the glutamatergic retinal waves in ganglion cells (Wong et al., 2000; Blankenship et al., 2009). Mice in which glutamate release from bipolar cells is suppressed form fewer synapses to ganglion cells compared to wildtype littermates (Kerschensteiner et al., 2009). Two-photon live has further revealed that the reduced number of synapses onto ganglion cells results from a decreased rate of synapse formation, suggesting that glutamatergic waves are required for excitatory synapse formation in the retina.

In the LSO, one obvious mechanism for the redistribution of inhibitory synapses toward the soma is that MNTB neurons specifically form new synapses onto the somata of LSO principal cells. It is also tantalizing to speculate that the formation of new synapses in LSO is guided by spontaneous activity. However, synapse redistribution can also occur through a separate, predetermined program that is independent of neural activity. In the retina, for example, direction-selective ganglion cells (DSGCs) generate robust spikes in response to a stimulus moving in a preferred direction, and not to stimuli moving in other directions (Oyster and Barlow, 1967). These DSGCs receive excitatory inputs from bipolar cells (BCs) and inhibitory inputs from starburst amacrine cells (SACs). Paired recordings of SACs and DSGCs correlated with serial block-face EM have revealed that SACs preferentially form inhibitory synapses on the ‘null’ side of the DSGCs, resulting in stronger inhibition on the null side (Lee et al., 2010; Briggman et al., 2011; Wei et al., 2011). This biased distribution of inhibitory synapses, which underlies the direction-selectivity of DSGCs, emerges a few days before eye-opening, coinciding with the period during which spontaneous retinal waves are common (Yonehara et al., 2011; Morrie and Feller, 2015). Given the critical role of patterned activity in refinement of many circuits, one might speculate that the retinal waves are required to establish asymmetric inhibition in the SAC-DSGC circuit. However, the lack of any effect on direction selectivity after pharmacological and genetic perturbation of the retinal waves suggests that SAC-DSGC synapse redistribution is independent of the retinal waves (Elstrott et al., 2008; Sun et al., 2011; Hamby et al., 2015). Instead, molecular cues such as protocadherins and semaphorins may be the primary drivers of refinement in this direction-selective circuit. Protocadherins are responsible for dendritic self-avoidance in SAC, and are required for normal direction selectivity (Lefebvre et al., 2012; Kostadinov and Sanes, 2015), whereas the transmembrane Semaphorin 6A is essential for axon guidance, and is required for nasal-preferring direction-selective circuits (Sun et al., 2013). Thus, in the auditory brainstem, although the redistribution of synapses occurs contemporaneously with the patterned spontaneous activity in the cochlear, we cannot ignore the possibility that the refinement we show here is pre-determined, as in the SAC-DSGC circuit.

5.2 Tonotopic refinement in the LSO

Whether or to what degree synapse redistribution contributes to the coordinated refinement of tonotopy in LSO remains an open puzzle. A few days after birth, individual LSO neurons receive many low-amplitude inhibitory inputs arising from a broad area in MNTB (Kim and Kandler 2003). Within the next week, individual LSO neurons lose about 75% of their inhibitory inputs from the MNTB, while the remaining inputs are strengthened by an order of magnitude. A previous study in mouse suggests that this synaptic strengthening is achieved by the increase in quantal size and quantal content, independent of synapse position (Kim and Kandler, 2010), though a reduction in rise times for single-fiber recordings suggested the proximal shift in synapse position found here in rats. More recent serial block-face EM has revealed that a week after hearing onset, the soma and proximal dendrite of individual LSO neurons are innervated by a large number of inhibitory axons with large varicosities and a small number of excitatory axons (Gjoni et al., 2018a), the strong somatic innervation providing fast inhibition to the LSO neurons. Perhaps synapse redistribution is less critical for tonotopic registration than for temporal find-tuning. A recent *in vivo* patch recording study revealed an inverse relationship between IPSP latency in the LSO and sound intensity at the contralateral ear, highlighting the importance of temporal precision of inhibition in ILD computation (Franken et al., 2018). A single study has examined the degree and development of tonotopic matching in the young LSO. Thus, we know that at hearing onset, excitatory and inhibitory synapses converging onto individual LSO principal neurons are already somewhat matched for stimulus frequency, and that further tuning occurs in one or perhaps two weeks after hearing onset (Sanes and Rubel, 1988). Why do LSO neurons initially receive such large number of excitatory synapses at the soma? One explanation for the initial somatic excitatory synapses might be that these excitatory synapses originate from what will in adult be an off-frequency band of the AVCN. During development, these excitatory synapses from the off-frequency band would be eliminated. Testing this model will require the ability to assign tonotopic representation to specific synaptic inputs at the subcellular level in the LSO. We can genetically label neurons in AVCN and MNTB with brainbow (Livet et al., 2007; Lichtman et al., 2008). In brainbow mice, fluorescent proteins are stochastically combined and expressed in the presynaptic neurons, such that scientist can reconstruct the circuit connection by matching the color of the axon and the soma. In LSO, we can label AVCN and MNTB with brainbow. Once we reconstruct the individual neurons in LSO, we can trace the synapses from the axon terminal back to AVCN and MNTB by matching the color of the somata in AVCN and MNTB. By doing so, we can map each synaptic inputs along LSO to neurons in AVCN and MNTB, and infer the tonotopic position of those neurons.

5.3 Structural plasticity in the LSO

During development, neurons and neural circuits may undergo significant structural changes. Although morphological and physiological changes are necessarily intertwined in the nervous system, here, I refer to the structural change as the anatomically measurable modification of neurites and synapses. Neural activity can induce changes in neurite growth and regulate synapse density (Cohan and Kater, 1986; Van Huizen and Romijn, 1987; Annis et al., 1994). In cortical pyramidal cells, dendritic spine volume is a useful proxy for excitatory synapse strength (Yuste, 2010); where LTP induces spine enlargement, LTD induces spine shrinkage (Okamoto et al., 2004; Yang et al., 2008; Oh et al., 2013). Moreover, LTP stabilizes the newly formed spine through an NMDAR-dependent mechanism (Hill and Zito, 2013). During development, neurons add and remove axonal branches with only a few branches stabilized (Wu and Cline, 1998; Portera-Cailliau et al., 2005). The stabilization of axonal and dendritic branches requires a local calcium signal (Vaillant et al., 2002; Hutchins and Kalil, 2008), showing how neural activity can cause structural changes in neural circuits.

Synapses that experience synchronous activity tend to cluster together along the dendrite, presumably through activity-dependent mechanisms. For example, in hippocampal pyramidal neurons, nearby synapses (< 16 µm) are more likely to be co-activated than synapses that are further apart (Kleindienst et al., 2011), and spontaneous activity and NMDAR activation are required for synapse clustering. In the LSO, inhibitory synapses were already slightly more clustered than excitatory synapses along the proximal dendrite, and synapses became more progressively clustered with synapses of the same time during the week before hearing onset.

Using MK-801, a use-dependent open-channel blocker of NMDA receptors, a former postdoc in the lab showed substantial, bidirectional, glutamate spillover between synapses of the excitatory and inhibitory input pathways to the LSO in the first postnatal week (Alamilla and Gillespie, 2011). This glutamate spillover was mediated primarily by GluN2B-containing NMDA receptors, and the rise time for the NMDAR-mediated response was longer under the inhibitory pathway than under the excitatory pathway. The authors suggested that this discrepancy could be due to a longer diffusion path from release site to receptors at inhibitory vs excitatory synapses. The data presented here allow for an alternative interpretation of the longer average rise times: faster average rise times for excitatory synapses could result instead from their greater density at or near the soma at the earliest ages. The authors further proposed that excitatory and inhibitory synapses onto LSO neurons might be able to engage in direction communication through glutamate spillover and NMDAR activation, and our data showing substantial intermingling of excitatory and inhibitory synapses in neonates are consistent with such a model.

5.4 Future directions

To tease apart whether and how spontaneous activity is required for the redistribution of synapses, we can perturb spontaneous activity using cochlear ablation or genetic manipulation. Experiments using cochlear ablation have demonstrated developmental impairment in the auditory brainstem. For example, at the calyx of Held of animals deprived of normal acoustic experience, synaptic currents and readily releasable pool size are smaller than at the normal calyx of Held, and NMDA receptors are expressed at higher levels, resulting in low-fidelity transmission (Futai et al., 2001; Grande et al., 2014). Cochlear ablation leads to decreased overall expression of VGLUT1 in the auditory brainstem, together with a decrease of amino acid neurotransmitters in the cochlear nucleus (Godfrey et al., 2015; Hasegawa et al., 2017). Cochlear ablation is however a crude manipulation, producing dramatic and irreversible effects. To probe for more nuanced effects on development, one can disrupt the temporal pattern of the spontaneous activity. In the immature cochlea, inner hair cells (IHCs) receive transient cholinergic inputs mediated by α9α10-nicotinic acetylcholine receptors (nAChRs) (Simmons et al., 1996; Glowatzki and Fuchs, 2000; Katz et al., 2004; Roux et al., 2011). Mice lacking the α9 subunit of nAChRs show a disrupted temporal structure of this spontaneous activity, and exhibit impairments in synaptic elimination and strengthening in the MNTB-LSO pathway as well as in axonal pruning of MNTB neurons (Tritsch and Bergles, 2010). Mice that lack the Ca^{2+} sensor otoferlin or the Ca^{2+} - activated K^{+} channel (SK2) also exhibit disrupted temporal structure of their spontaneous cochlear activity, and show impaired development of IHCs and of the MNTB – LSO connection (Johnson et al., 2013; Müller et al., 2019). These mouse models are thus prime candidates for investigating whether spontaneous activity is required for synapse redistribution, and if so for understanding the information content in the temporally patterned spontaneous activity.

To investigate whether new inhibitory synapses are preferentially formed around the soma, one might look for markers associated with synaptogenesis, for example, by staining for gephyrin and neuroligin-2. Neuroligin-2 (NL2), a cell adhesion protein localized in inhibitory synapses (Varoqueaux et al., 2004), is required for the recruitment of gephyrin around the soma, suggesting that NL2 is essential for somatic inhibitory synapse formation (Poulopoulos et al., 2009). In the rodent LSO, the redistribution of inhibitory synapses toward the soma can be attributed to formation of new perisomatic synapses, and it is possible that experiments performed with higher temporal resolution might show 'pre-synapses,' indicated by Neuroligin-2 clusters, that later result in gephyrin-positive synapses around the soma.

Here, we have sampled different developmental timepoints from different organisms in order to reconstruct morphological changes experienced by immature LSO neurons. In order to better understand the mechanisms underlying these changes, a more manipulable preparation, and one that allows for chronic sampling from the same preparation, i.e., one in which we could visualize the synapse position in real-time during development, would be preferable. Ideally, this would be performed using organotypic slice culture culture, and such cultures have been performed in this system (Tong et al., 2010; Dimitrov et al., 2016; Kronander et al., 2017). By culturing slices from transgnenic mice with genetically encoded fluorescent protein for both excitatory and inhibitory synapses (Chen et al., 2012; Specht et al., 2013; Bosch et al., 2014; Meyer et al., 2014; Villa et al., 2016), we would stimulate both AVCNs using realistic spontaneous activity patterns shown in Chapter 5. Two-photon imaging in the cultured slice would allow us to visualize the synapse redistribution in real-time over several days to weeks.

In this thesis, we have observed substantial reorganization of synapse location before hearing onset in rat's LSO, we also want to know whether neurons in LSO continue to refine their synapse position after hearing onset. Redistribution of inhibitory synapses requires acoustic activity in MSO (Kapfer et al., 2002), and it is plausible that a proportional redistribution of inhibitory and excitatory synapses also requires acoustic activity in LSO. Early EM studies in cats and guinea pigs suggested that adult LSO neurons receive almost inclusively inhibitory inputs at the soma (Cant, 1984; Helfert et al., 1992). A more recent SBEM studies in mice suggested at P18 LSO neurons receive a small number of excitatory inputs (Gjoni et al., 2018a). Our results showed a remarkable decrease in the E/I synapse ratio at the soma before hearing onset. Given the previous ultrastructure results, it is tantalizing to predict that the E/I synapse ratio at soma can further refine after hearing onset. In order to test this hypothesis, we can label individual LSO cells in slices from older animals. The current challenge is that the slice health of the older brainstem tissue is poor, such that the labelled LSO neurons can hardly survive after slice recovery.

The morphological data of the dendritic trees of LSO cells as well as synapse positions also allow us to create computational models to predict the physiological properties. Previously, scientists have modeled LSO neurons with point process model and integrate-and-fire model with low-threshold potassium current and/or afterhyperpolarization channels (Johnson et al., 1986; Gai et al., 2009; Zhou and Colburn, 2010; Wang and Colburn, 2012). Other modelling studies have also investigated the interaction between excitation and inhibition in LSO (Zacksenhouse et al., 1992; Gjoni et al., 2018b). Due to the insufficiency of morphological data, only one study incorporated a compartment model for LSO (Zacksenhouse et al., 1998). However, this model only presented the dendritic field with two cylinders with inhibitory synapses around the soma and excitatory synapses on dendrites. Our morphological data together with the subcellular location of the synapses allow us to create a compartment model to mimic the nature of the LSO neurons. By doing so, we can stimulate the prehearing modeled neuron with patterned spontaneous activity and post-hearing modeled neuron with acoustically driven activity. Moreover, model with the subcellular location of the synapses allows us to investigate how sub-threshold event at a specific synapse can influence the activity at neighboring synapses.

5.5 References

Alamilla J, Gillespie DC (2011) Glutamatergic inputs and glutamate-releasing immature inhibitory inputs activate a shared postsynaptic receptor population in lateral superior olive. Neuroscience 196:285–296.

Annis CM, K. O'Dowd D, Robertson RT (1994) Activity-dependent regulation of dendritic spine density on cortical pyramidal neurons in organotypic slice cultures. J Neurobiol 25:1483–1493.

Blankenship AG, Ford KJ, Johnson J, Seal RP, Edwards RH, Copenhagen DR, Feller MB (2009) Synaptic and Extrasynaptic Factors Governing Glutamatergic Retinal Waves. Neuron 62:230–241.

Bosch M, Castro J, Saneyoshi T, Matsuno H, Sur M, Hayashi Y (2014) Structural and molecular remodeling of dendritic spine substructures during long-term potentiation. Neuron 82:444–459.

Briggman KL, Helmstaedter M, Denk W (2011) Wiring specificity in the direction-selectivity circuit of the retina. Nature 471:183–190.

Cant NB (1984) The fine structure of the lateral superior olivary nucleus of the cat. J Comp Neurol 227:63–77.

Chen JL, Villa KL, Cha JW, So PTC, Kubota Y, Nedivi E (2012) Clustered Dynamics of Inhibitory Synapses and Dendritic Spines in the Adult Neocortex. Neuron 74:361–373.

Clause A, Kim G, Sonntag M, Weisz CJC, Vetter DE, Rubsamen R, Kandler K (2014) The Precise Temporal Pattern of Prehearing Spontaneous Activity Is Necessary for Tonotopic Map Refinement. Neuron 82:822–835.

Cohan CS., Kater SB. (1986) Suppression of Neurite Elongation and Growth Cone Motility by Electrical Activity. Science (80-) 232:1638–1640.

Dimitrov D, Takagi H, Guillaud L, Saitoh N, Eguchi K, Takahashi T (2016) Reconstitution of giant mammalian synapses in culture for molecular functional and imaging studies. J Neurosci 36:3600–3610.

Elstrott J, Anishchenko A, Greschner M, Sher A, Litke AM, Chichilnisky EJ, Feller MB (2008) Direction Selectivity in the Retina Is Established Independent of Visual Experience and Cholinergic Retinal Waves. Neuron 58:499–506.

Franken TP, Joris PX, Smith PH (2018) Principal cells of the brainstem's interaural sound level detector are temporal differentiators rather than integrators. Elife 7:1–25.

Futai K, Okada M, Matsuyama K, Takahashi T (2001) High-fidelity transmission acquired via a developmental decrease in NMDA receptor expression at an auditory synapse. J Neurosci 21:3342–3349.

Gabbiani F, Krapp HG, Koch C, Laurent G (2002) Multiplicative computation in a visual neuron sensitive to looming. Nature 420:320–324.

Gai Y, Doiron B, Kotak V, Rinzel J (2009) Noise-gated encoding of slow inputs by auditory brain stem neurons with a low-threshold K+ current. J Neurophysiol 102:3447–3460.

Gjoni E, Aguet C, Sahlender DA, Knott G, Schneggenburger R (2018a) Ultrastructural basis of strong unitary inhibition in a binaural neuron. J Physiol 596:4969–4982.

Gjoni E, Zenke F, Bouhours B, Schneggenburger R (2018b) Specific synaptic input strengths determine the computational properties of excitation–inhibition integration in a sound localization circuit. J Physiol 596:4945–4967.

Glowatzki E, Fuchs PA (2000) Cholinergic Synaptic Inhibition of Inner Hair Cells in the Neonatal Mammalian Cochlea. Science (80-) 288:2366–2368.

Godfrey DA, Chen K, Godfrey MA, Lee AC, Crass SP, Shipp D, Simo H, Robinson KT (2015) Cochlear ablation effects on amino acid levels in the chinchilla cochlear nucleus. Neuroscience 297:137–159.

Grande G, Negandhi J, Harrison R V., Wang LY (2014) Remodelling at the calyx of Held-MNTB synapse in mice developing with unilateral conductive hearing loss. J Physiol 592:1581–1600.

Hamby AM, Rosa JM, Hsu CH, Feller MB (2015) CaV3.2 KO mice have altered retinal waves but normal direction selectivity. Vis Neurosci 32.

Hasegawa H, Hatano M, Sugimoto H, Ito M, Kawasaki H, Yoshizaki T (2017) The effects of unilateral cochlear ablation on the expression of vesicular glutamate transporter 1 in the lower auditory pathway of neonatal rats. Auris Nasus Larynx 44:690–699.

Helfert RH, Juiz JM, Bledsoe SC, Bonneau JM, Wenthold RJ, Altschuler RA (1992) Patterns of glutamate, glycine, and GABA immunolabeling in four synaptic terminal classes in the lateral superior olive of the guinea pig. J Comp Neurol 323:305–325.

Hill TC, Zito K (2013) LTP-induced long-term stabilization of individual nascent dendritic spines. J Neurosci 33:678–686.

Hutchins BI, Kalil K (2008) Differential outgrowth of axons and their branches is regulated by localized calcium transients. J Neurosci 28:143–153.

Johnson DH, Tsuchitani C, Linebarger DA, Johnson MJ (1986) Application of a point process model to responses of cat lateral superior olive units to ipsilateral tones. Hear Res 21:135–159.

Johnson SL, Kuhn S, Franz C, Ingham N, Furness DN, Knipper M, Steel KP, Adelman JP, Holley MC, Marcotti W (2013) Presynaptic maturation in auditory hair cells requires a critical period of sensory-independent spiking activity. Proc Natl Acad Sci U S A 110:8720–8725.

Kapfer C, Seidl AH, Schweizer H, Grothe B (2002) Experience-dependent refinement of inhibitory inputs to auditory coincidence-detector neurons. Nat Neurosci 5:247–253.

Katz E, Elgoyhen AB, Gómez-Casati ME, Knipper M, Vetter DE, Fuchs PA, Glowatzki E (2004) Developmental regulation of nicotinic synapses on cochlear inner hair cells. J Neurosci 24:7814–7820.

Kerschensteiner D, Morgan JL, Parker ED, Lewis RM, Wong ROL (2009) Neurotransmission selectively regulates synapse formation in parallel circuits in vivo. Nature 460:1016–1020.

Kim G, Kandler K (2010) Synaptic changes underlying the strengthening of GABA/ glycinergic connections in the developing lateral superior olive. Neuroscience 171:924–933.

Kleindienst T, Winnubst J, Roth-Alpermann C, Bonhoeffer T, Lohmann C (2011) Activity-dependent clustering of functional synaptic inputs on developing hippocampal dendrites. Neuron 72:1012–1024.

Kostadinov D, Sanes JR (2015) Protocadherin-dependent dendritic selfavoidance regulates neural connectivity and circuit function. Elife 4:1–23.

Kronander E, Michalski N, Lebrand C, Hornung JP, Schneggenburger R (2017) An organotypic slice culture to Study the formation of calyx of Held synapses in-vitro. PLoS One 12:1–19.

Lee S, Kim K, Zhou ZJ (2010) Role of ACh-GABA Cotransmission in Detecting Image Motion and

Motion Direction. Neuron 68:1159–1172.

Lefebvre JL, Kostadinov D, Chen W V., Maniatis T, Sanes JR (2012) Protocadherins mediate dendritic self-avoidance in the mammalian nervous system. Nature 488:517–521.

Lichtman JW, Livet J, Sanes JR (2008) A technicolour approach to the connectome. Nat Rev Neurosci 9:417–422.

Livet J, Weissman TA, Kang H, Draft RW, Lu J, Bennis RA, Sanes JR, Lichtman JW (2007) Transgenic strategies for combinatorial expression of fluorescent proteins in the nervous system. Nature 450:56–62.

Meyer D, Bonhoeffer T, Scheuss V (2014) Balance and stability of synaptic structures during synaptic plasticity. Neuron 82:430–443.

Morrie RD, Feller MB (2015) An asymmetric increase in inhibitory synapse number underlies the development of a direction selective circuit in the retina. J Neurosci 35:9281–9286.

Müller NIC, Sonntag M, Maraslioglu A, Hirtz JJ, Friauf E (2019) Topographic map refinement and synaptic strengthening of a sound localization circuit require spontaneous peripheral activity. J Physiol 597:5469–5493.

O'Shea M, Williams JLD (1974) The anatomy and output connection of a locust visual interneurone; the lobular giant movement detector (LGMD) neurone. J Comp Physiol 91:257–266.

Oh WC, Hill TC, Zito K (2013) Synapse-specific and size-dependent mechanisms of spine structural plasticity accompanying synaptic weakening. Proc Natl Acad Sci U S A 110.

Okamoto KI, Nagai T, Miyawaki A, Hayashi Y (2004) Rapid and persistent modulation of actin dynamics regulates postsynaptic reorganization underlying bidirectional plasticity. Nat Neurosci 7:1104–1112.

Oyster CW, Barlow HB (1967) Direction-Selective Units in Rabbit Retina : Distribution of Preferred Directions. Scie 155:841–842.

Peron SP, Jones PW, Gabbiani F (2009) Precise Subcellular Input Retinotopy and Its Computational Consequences in an Identified Visual Interneuron. Neuron 63:830–842.

Peron SP, Krapp HG, Gabbiani F (2007) Influence of electrotonic structure and synaptic mapping on the receptive field properties of a collision-detecting neuron. J Neurophysiol 97:159–177.

Portera-Cailliau C, Weimer RM, De Paola V, Caroni P, Svoboda K (2005) Diverse modes of axon elaboration in the developing neocortex. PLoS Biol 3.

Poulopoulos A, Aramuni G, Meyer G, Soykan T, Hoon M, Papadopoulos T, Zhang M, Paarmann I, Fuchs C, Harvey K, Jedlicka P, Schwarzacher SW, Betz H, Harvey RJ, Brose N, Zhang W, Varoqueaux F (2009) Neuroligin 2 Drives Postsynaptic Assembly at Perisomatic Inhibitory Synapses through Gephyrin and Collybistin. Neuron 63:628–642.

Roux I, Wersinger E, McIntosh JM, Fuchs PA, Glowatzki E (2011) Onset of cholinergic efferent synaptic function in sensory hair cells of the rat cochlea. J Neurosci 31:15092–15101.

Sanes DH, Rubel EW (1988) The ontogeny of inhibition and excitation in the gerbil lateral superior olive. J Neurosci 8:682–700.

Simmons DD, Moulding HD, Zee D (1996) Olivocochlear innervation of inner and outer hair cells during postnatal maturation: An immunocytochemical study. Dev Brain Res 95:213–226.

Specht CG, Izeddin I, Rodriguez PC, ElBeheiry M, Rostaing P, Darzacq X, Dahan M, Triller A (2013) Quantitative nanoscopy of inhibitory synapses: Counting gephyrin molecules and receptor binding sites. Neuron 79:308–321.

Sun L, Han X, He S (2011) Direction-selective circuitry in rat retina develops independently of GABAergic, cholinergic and action potential activity. PLoS One 6.

Sun LO, Jiang Z, Rivlin-Etzion M, Hand R, Brady CM, Matsuoka RL, Yau KW, Feller MB, Kolodkin AL (2013) On and off retinal circuit assembly by divergent molecular mechanisms. Science (80-) 342.

Tong H, Steinert JR, Robinson SW, Chernova T, Read DJ, Oliver DL, Forsythe ID (2010) Regulation of Kv channel expression and neuronal excitability in rat medial nucleus of the trapezoid body maintained in organotypic culture. J Physiol 588:1451–1468.

Tritsch NX, Bergles DE (2010) Developmental regulation of spontaneous activity in the mammalian cochlea. J Neurosci 30:1539–1550.

Tritsch NX, Rodríguez-Contreras A, Crins TTH, Wang HC, Borst JGG, Bergles DE (2010) Calcium action potentials in hair cells pattern auditory neuron activity before hearing onset. Nat Neurosci 13:1050–1052.

Vaillant AR, Zanassi P, Walsh GS, Aumont A, Alonso A, Miller FD (2002) Signaling mechanisms underlying reversible activity-dependent dendrite formation. Neuron 34:985–998.

Van Huizen F, Romijn HJ (1987) Tetrodotoxin enhances initial neurite outgrowth from fetal rat cerebral cortex cells in vitro. Brain Res 408:271–274.

Varoqueaux F, Jamain S, Brose N (2004) Neuroligin 2 is exclusively localized to inhibitory synapses. Eur J Cell Biol 83:449–456.

Villa KL, Berry KP, Subramanian J, Cha JW, Oh WC, Kwon HB, Kubota Y, So PTC, Nedivi E (2016) Inhibitory Synapses Are Repeatedly Assembled and Removed at Persistent Sites In Vivo. Neuron 89:756–769.

Wang L, Colburn HS (2012) A modeling study of the responses of the lateral superior olive to ipsilateral sinusoidally amplitude-modulated tones. JARO - J Assoc Res Otolaryngol 13:249–267.

Wei W, Hamby AM, Zhou K, Feller MB (2011) Development of asymmetric inhibition underlying direction selectivity in the retina. Nature 469:402–406.

Wong WT, Myhr KL, Miller ED, Wong ROL (2000) Developmental changes in the neurotransmitter regulation of correlated spontaneous retinal activity. J Neurosci 20:351–360.

Wu G-Y, Cline HT (1998) Stabilization of Dendritic Arbor Structure in Vivo by CaMKII. Science (80-) 279:222–226.

Yang Y, Wang X Bin, Frerking M, Zhou Q (2008) Spine expansion and stabilization associated with long-term potentiation. J Neurosci 28:5740–5751.

Yonehara K, Balint K, Noda M, Nagel G, Bamberg E, Roska B (2011) Spatially asymmetric reorganization of inhibition establishes a motion-sensitive circuit. Nature 469:407–410.

Yuste R (2010) Dendritic spines. Cambridge, Massachusetts: The MIT Press.

Zacksenhouse M, Johnson DH, Tsuchitani C (1992) Excitatory/inhibitory interaction in the LSO revealed by point process modeling. Hear Res 62:105–123.

Zacksenhouse M, Johnson DH, Williams J, Tsuchitani C (1998) Single-neuron modeling of LSO unit responses. J Neurophysiol 79:3098–3110.

Zhou Y, Colburn HS (2010) A modeling study of the effects of membrane afterhyperpolarization on spike interval statistics and on ILD encoding in the lateral superior olive. J Neurophysiol

103:2355–2371.

Zhu Y, Gabbiani F (2016) Fine and distributed subcellular retinotopy of excitatory inputs to the dendritic tree of a collision-detecting neuron. J Neurophysiol 115:3101–3112.